DEVICE APPLICATIONS OF RARE-EARTH NITRIDES.

BY

HARRY WARRING

A thesis
submitted to the Victoria University of Wellington in fulfilment of
the requirements for the degree of Doctor of Philosophy

Victoria University of Wellington
(2016)

Abstract

In this thesis the properties of thin film spintronic devices are investigated. These devices incorporate rare-earth nitrides as the active elements in a geometry with vertical transport perpendicular to the layers. Many rare-earth nitrides are ferromagnetic semiconductors with a rich range of magnetic properties arising from their *4-f* magnetic moments. These magnetic moments contain both spin and orbital contributions, in contrast to the quenched, spin-based magnetism frequently exploited in spintronic devices based on transition metals.

Magnetic tunnel junctions are demonstrated with the ferromagnetic electrodes made from the intrinsic ferromagnetic semiconductor GdN surrounding GaN and AlN barriers. Fitting of the current-voltage characteristics of a GdN/GaN/GdN device determines a barrier height of 1.5 eV at room temperature. This puts the GdN Fermi level close to the GaN mid-gap, consistent with recent theoretical predictions of the band alignment at the GdN/GaN interface [Kagawa et al., Phys. Rev. Applied 2, 054009 (2014)]. This barrier height is found to scale with the band gap of the group-III nitride barrier, being approximately twice as large for AlN barriers. It was observed that the barrier height reduces as the AlN barrier thickness increases, signalling the formation of Schottky barriers at the interface. These polycrystalline junctions exhibit a tunnel magnetoresistance of a few percent but do not show clear signs of homogeneous switching. The transport properties of the GdN/GaN/GdN junctions are heavily influenced by the electronic structure of the semiconducting GdN layers, making junctions based on rare-earth nitrides promising candidates for further investigation.

A fully semiconductor-based magnetic tunnel junction that uses spin-orbit cou-

pled materials made of *intrinsic* ferromagnetic semiconductors is then presented. Unlike more common approaches, one of the electrodes consists of a near-zero magnetic moment ferromagnetic semiconductor, samarium nitride, with the other electrode comprised of the more conventional ferromagnetic semiconductor gadolinium nitride. Fabricated tunnel junctions exhibit magnetoresistances as high as 200%, implying strong spin polarisation in both electrodes. In contrast to conventional tunnel junctions, the resistance is largest at high fields, a direct result of the orbital-dominant magnetisation in samarium nitride that requires the spin in this electrode aligns opposite to that in the gadolinium nitride when the magnetisation is saturated. The magnetoresistance at intermediate fields is controlled by the formation of a twisted magnetisation phase in the samarium nitride, a direct result of the orbital-dominant ferromagnetism. Thus, new functionality can be brought to magnetic tunnel junctions by use of novel electrode materials, in contrast to the usual focus on tuning the barrier properties.

Finally, highly resistive GdN films intentionally doped with Mg are demonstrated. These films are found to have increased resistivities and decreased carrier concentrations, with no observed degradation in crystal quality as compared with undoped films. An increase of the Curie temperature in conductive films is observed which is consistent with the existence of magnetic polarons centred on nitrogen vacancies. The prospect of doping rare-earth nitride films in this manner promises greater control of the material properties and future device applications.

Acknowledgements

First and foremost I would like to thank my supervisors Ben Ruck and Joe Trodahl for their advice and support throughout my studies. I am grateful to the group at large for providing such a great working environment during my PhD. This includes not just my research group: Franck Natali, James McNulty, Eva Anton, Bart Ludbrook, Felicia Ullstad, Do Le Binh, Jay Chan, Tanmay Maity and Chang Min-Lee but also the cleanroom group: Natalie Plank, Hannah Zheng, Conor Burke-Govey, Leo Browning, Cameron Wood and Ciaran Moore.

I was fortunate to share a great office where we had many great discussions and would like to thank: Brendan Darby, Matthias Meyer, Peter Hauer, Walter Somerville, Baptiste Auguié, Camille Artur, along with all the other students, postdocs and academics with whom I have interacted with over the last few years.

For assistance with technical and equipment issues I would like to thank Peter Coard, David Stead, Olly Pantoja, Shen Chong and Simon Granville, David Flynn, Nick Grinter, Alan Rennie, Manu Pouajen-Blakiston and all the technical and administrative staff at Victoria.

A big thanks to Stéphane Vézian and Benjamin Damilano for their hospitality during my all too brief visit to Valbonne.

Financial and other assistance from Victoria University and the MacDiarmid institute were also instrumental towards the completion of this thesis, along with the external funding by which our research is supported.

I am also grateful for the support of my friends, family and Dani Metin.

Contents

Terminology: Acronyms, variables and initialisms.

AlN	Aluminium Nitride
CB	Conduction Band
CNRS	Centre Nationale De La Recherche Scientifique
CRHEA	Centre de Recherche sur l'Hétéro-Epitaxie et ses Applications
DFT	Density Functional Theory
DOS	Density of States
DRAM	Dynamic Random Access Memory
e	Electronic charge $= 1.60 \times 10^{-19}$ C
EDS	Energy-Dispersive X-ray Spectroscopy
E-gun	Electron Gun
GaN	Gallium Nitride
GdN	Gadolinium Nitride
GMR	Giant Magnetoresistance
FC	Field Cooled
FET	Field Effect Transistor
FWHM	Full Width at Half Maximum
I-V	Current-Voltage
J-V	Current Density-Voltage
k_B	Boltzmann Constant $= 1.38 \times 10^{-23}$ $m^2kgs^{-2}K^{-1}$ (SI)
m_e	Electron rest mass $= 9.11 \times 10^{-31}$ kg

MR	Magnetoresistance
MRAM	Magnetic Random Access Memory
LMTO	Linear Muffin-Tin Orbital
LSDA	Localised Spin Density Approximation
REN	Rare-Earth Nitride
RSO	Reciprocating Sample Option
SEI	Secondary Electron Imaging
SEM	Scanning Electron Microscope
SIC	Self Interaction Correction
SQUID	Superconducting Quantum Interference Device
T_C	Curie Temperature
TCR	Temperature Coefficient of Resistance
TMR	Tunnel Magnetoresistance
VUW	Victoria University of Wellington
UHV	Ultra High Vacuum
μ_B	Bohr Magneton $= 9.27 \times 10^{-24}$ JT^{-1}
VB	Valence Band
WKB	Wentzel-Kramers-Brillouin
XRD	X-Ray Diffraction
YSZ	Yttria Stabilised Zirconia
ZFC	Zero Field Cooled

List of Figures

Publications

During this project I have been involved in several publications. Three of these are first author publications, and nine are publications where I appear as a co-author. In this section both my own, and my co-authors contributions to these publications will be listed in reverse chronological order. These are split into two sections; this first being where I am the first-author, and the second being where I am listed as a co-author.

First Authored Publications

H. Warring, H.J. Trodahl, N.O.V. Plank, F. Natali, S. Granville, and B.J. Ruck. "Magnetic tunnel junctions incorporating a near-zero-moment ferromagnetic semiconductor," Phys. Rev. Applied, Accepted 2016.

This paper presents the results shown in of Chapter 5 of this thesis. I did all of the sample preparation, measurements and most of the data analysis. My co-authors assisted with the conception of the study, experimental advice throughout, interpretation of the data, and with preparation of the manuscript.

H. Warring, B. J. Ruck, J. F. McNulty, E.-M. Anton, S. Granville, A. Koo, B. Cowie, and H. J. Trodahl, "YbN: An intrinsic semiconductor with antiferromagnetic exchange," Phys. Rev. B, vol. 90, p. 245206, Dec 2014.

I performed the sample growth for this study, along with many of the measurements, the analysis, and the writing of the manuscript. Assistance from several people was required in order to complete the measurements: James McNulty,

Ben Ruck and Eva Anton assisted me (under the supervision of Bruce Cowie) in performing x-ray spectroscopy measurements at the Australian synchrotron. Annette Koo performed optical reflection and transmission measurements which I then analysed using Tfcalc [4]. This modelling was required to account for the multiple reflections within the multilayer system. Simon Granville helped with the magnetic measurements. Ben Ruck and Joe Trodahl then helped with the interpretation and presentation of the data in the final manuscript which was highlighted as an editor's suggestion in Physical Review B.

H. Warring, B. J. Ruck, H. J. Trodahl, and F. Natali, "Electric field and photo-excited control of the carrier concentration in GdN," Appl. Phys. Lett., vol. 102, no. 13, p. 132409, 2013.

The sample growth, device fabrication, measurements and analysis were performed during my Honours project. This paper is included as it was published during my PhD. The research was conducted under the guidance of Ben Ruck, Joe Trodahl and Franck Natali who were also involved in preparation of the manuscript.

Co-Authored Publications

C. Burke-Govey, U. Castanet, H. Warring, A. Nau, B. J. Ruck, J. Majimel and N. O. V. Plank, "Realizing field-dependent ZnO nanowires without high-temperature annealing," Nanotechnology, Submitted 2016."

I contributed to this study by way of UV photoconductivity measurements of ZnO devices in vacuum. I also prepared some computer rendered diagrams for the paper. All sample preparation, other measurements, and writing of the paper was performed by the other authors.

C.-M. Lee, H. Warring, S. Vézian, H. J. Trodahl, B. J. Ruck and F. Natali "Photoconductivity investigation of recombination in Mg-doped epitaxial GdN thin films," J. Appl. Phys, Submitted 2016

I contributed to this paper by helping to conceive and set-up the photoconductivity experiments. The other authors contributed to the growth, measurements, analysis and writing of the paper.

J. F. McNulty, E.-M. Anton, B. J. Ruck, F. Natali, H. Warring, F. Wilhelm, A. Rogalev, M. M. Soares, N. B. Brookes, and H. J. Trodahl, "Twisted phase of the orbital-dominant ferromagnet SmN in a GdN/SmN heterostructure," Phys. Rev. B, vol. 91, p. 174426, May 2015.

My contribution to this paper involved assistance in preparation of the samples along with F. Natali, J. F. McNulty, and E.-M. Anton. The measurements were conducted at the European synchrotron radiation facility (ESRF) by E.-M. Anton, B. J. Ruck, C. Meyer, H. J. Trodahl, F. Wilhelm, A. Rogalev, M. M. Soares, and N. B. Brookes. Data analysis and writing of the paper was primarily done by J.F. McNulty.

F. Ullstad, J. R. Chan, H. Warring, N. Plank, B. Ruck, J. Trodahl, and F. Natali, "Ohmic contacts of Au and Ag metals to n-type GdN thin films," AIMS Materials Science, vol. 2, no. 20150204, pp. 79-85, 2015.

The project was conducted by Felicia Ullstad under the supervision of Franck Natali, Ben Ruck, Joe Trodahl, and using the laboratory of Natalie Plank. My contribution was primarily offering experimental advice, and assistance in preparing some of these samples. Jay Chan performed x-ray reflectometry measurements.

C.-M. Lee, H. Warring, S. Vézian, B. Damilano, S. Granville, M. Al Khalfioui, Y. Cordier, H. J. Trodahl, B. J. Ruck, and F. Natali, "Highly resistive epitaxial Mg-doped GdN thin films," Appl. Phys. Lett., vol. 106, no. 2, 2015.

The samples for this paper were prepared in two batches by our collaborators in France (S. Vézian, B. Damilano, M. Al Khalfioui, Y. Cordier). During the first year of my PhD I spent several months characterising the first batch of these samples using temperature dependent resistivity, Hall effect and SQUID measurements. Based on the early promise shown, this study was spun-off into a masters project and C.-M. Lee took over. A second batch of samples was prepared which C.-M. Lee characterised, he then analysed the data as a whole and wrote up the paper with assistance from F. Natali, H. J. Trodahl and B. J. Ruck who also provided leadership for this project.

F. Natali, S. Vézian, S. Granville, B. Damilano, H. Trodahl, E.-M. Anton, H. Warring, F. Semond, Y. Cordier, S. V. Chong, and B. J. Ruck, "Molecular beam epitaxy of ferromagnetic epitaxial GdN thin films ," J. Cryst. Growth, vol. 404, pp. 146-151, 2014.

These samples were prepared as part of our ongoing collaboration with CHREA-CNRS in France. My contribution was in performing some measurements on the samples. My co-authors performed most of the other measurements, analysis and preparation of the samples and manuscript.

D. Le Binh, B. J. Ruck, F. Natali, H. Warring, H. J. Trodahl, E.-M. Anton, C. Meyer, L. Ranno, F. Wilhelm, and A. Rogalev, "Europium Nitride: A Novel Diluted Magnetic Semiconductor," Phys. Rev. Lett., vol. 111, p. 167206, Oct 2013.

This paper was the culmination of Do Le Binh's PhD thesis and as such much of the work can be attributed to him. Co-authors contributions focus largely on assistance with synchrotron measurements along with analysis and interpretation of data. My role was primarily the preparation of several samples used in this study.

Eva-Maria Anton, B. J. Ruck, C. Meyer, F. Natali, Harry Warring, Fabrice Wilhelm, A. Rogalev, V. N. Antonov, and H. J. Trodahl, "Spin/orbit moment imbalance in the near-zero moment ferromagnetic semiconductor SmN," Phys. Rev. B, vol. 87, no. 13, p. 134414, 2013.

My contribution to this paper was assistance in preparing samples. The other authors conducted other aspects of the growth along with all of the characterisation, synchrotron measurements and analysis.

M. Azeem, B. J. Ruck, B. Do Le, H. Warring, H. J. Trodahl, N. M. Strickland, A. Koo, V. Goian, and S. Kamba, "Optical response of DyN," J. Appl. Phys., vol. 113, no. 20, p. 203509, 2013.

Optical measurements and analysis were performed by M. Azeem, N. M. Strickland, A. Koo, V. Goian and S. Kamba. I assisted M. Azeem with film growth, and prepared films capped with Si for optical measurements in the far infrared region.

Chapter 1

Introduction

1.1 Motivation

1.1.1 Devices, Materials and Spintronics

There are many pragmatic reasons for studying new materials and devices. Recent technological progress has been wrought from silicon technology by producing ever smaller integrated circuits. The age of Moore's law and the conventional two-dimensional silicon integrated circuit is drawing to an end as nanofabrication techniques draw ever closer to size and cost limitations imposed by both the atoms involved and the Heisenberg uncertainty principle [5]. There is also the problem of heat dissipation and parasitic resistances due to interconnects on circuits which result in significant power (and voltage) losses. New technologies will have to sidestep these size limitations by accessing further degrees of freedom to increase computational power density. Aside from the obvious economic and technological reasons for researching new materials and systems, fundamental reasons include exploring the often unique physics of new materials and devices which may in turn result in unforeseen technological developments.

One such area of interest beyond the scope of existing silicon architecture is the burgeoning field of spintronics [6]. Spintronics involves accessing the extra degree of freedom offered by the spin of electrons, on top of the charge degree

of freedom exploited in conventional electronics. Several technological advances have already been realised using spintronics, most notably the read heads used to examine individual bits on computer hard drive platters [7]. These read heads exploit the interaction between the magnetic and electronic properties of their materials to produce a change in the resistance when the device is in the proximity of a local magnetic field. Most commonly, the effects exploited here are tunnelling magnetoresistance (TMR) and giant magnetoresistance (GMR) for which the 2007 Nobel Prize in Physics was awarded to Albert Fert and Peter Grünberg.

In recent years there has been a push within the spintronics community into a variety of different technological applications. This includes magnetic random access memory (MRAM), which is already commercially available albeit on a limited scale. The advantages offered by MRAM are numerous: MRAM combines the benefits of existing dynamic random access memory (DRAM) and flash memory such as high speeds, low power consumption, non-volatility, and long working life [8]. These technologies are frequently applied in a vertical transport orientation with the current perpendicular to the substrate plane.

1.1.2 Ferromagnetic Semiconductors

To date, much of the focus within the spintronics community has been on conventional transition metal-based ferromagnets such as iron, cobalt and their alloys. These metallic systems have already proven useful. However, there are several notable advantages to be gained from examining ferromagnetic semiconductors, such as increased spin polarisation and the ability to tune their properties through doping and/or electric fields.

Many of the ferromagnetic semiconductors studied to date involve the dilution of magnetic ions within an existing semiconductor framework, such as (Ga,Mn)As [9]. While these dilute systems offer greater integration with existing materials there are drawbacks, in particular the potential for magnetic impurity phases such as Mn clusters. Intrinsic ferromagnetic semiconductors are materials which are intrinsically both ferromagnetic and semiconducting without the need for magnetic dopant atoms. Despite these and other advantages offered by ferromag-

netic semiconductors they have not received as much attention in the literature, in part due to the scarcity of ferromagnetic semiconductors available.

1.1.3 Rare-Earth Nitrides

Recent studies have revealed that many intrinsic ferromagnetic semiconductors exist within a family of compounds known as the rare-earth nitrides (RENs).

The rare-earth metals contain the lanthanides as well as scandium and yttrium. The majority of the world's rare-earth minerals are produced by China with sources originating in Mongolia [10]. The rare earths have a number of uses in modern electronics, including in the electric motors of hybrid cars and wind turbines [11][1]. When reacted with nitrogen they form a rare-earth nitride crystal in the rock salt structure.

Recently there has been a focus on incorporating RENs into prototype spintronic thin-film devices. Many of these applications utilise the high spin polarisation offered by a ferromagnetic semiconductor. One such avenue for research has been into spin filter Josephson junctions, in which tunnel junctions are formed with the REN as the barrier element. Both GdN and DyN have been examined in this role so far, owing to their large magnetic moments [12–14]. There has also been significant interest in incorporation of rare-earth nitrides into group-III nitride devices. Partly owing to the epitaxial compatibility of the rare-earth nitrides with these materials, and for the potential of injecting spin-polarised currents, GdN has been examined as a spin-injector into GaN islands [15]. Finally, efforts to incorporate the RENs into field effect transistors demonstrate the ability to field control the carrier concentration, opening the door to potential spin-polarised transistors [16].

Alongside spintronics applications the REN series is also interesting for fun-

[1] Frequently the rare earths attract criticism for being expensive and hard to find. Not only are the rare earths as abundant in the Earth's crust as common metals such as copper or lead [10], but a single $1\,\mathrm{cm}^2 \times 100\,\mathrm{nm}$ thick thin film device uses $\approx 0.1\,\mathrm{mg}$ of gadolinium metal. 10^7 such devices could be produced using the same amount of rare-earth metal (one tonne) as a single wind turbine.

damental reasons. The strongly-correlated nature of the electrons presents an abundant testing ground for theoretical models which are made more tractable by the simple rock-salt structure of these materials. There is also a rich variety of magnetic properties within the series, with varying degrees of orbital contributions making for interesting effects when the spin and orbital contributions of various members are played off against one another [17]. The partially filled *4-f* orbitals give rise to a range of magnetic moments within the series which differ both in magnitude and in spin/orbital composition, as described by Hund's rules. The additional properties offered by these orbital contributions sets the RENs apart from conventional transition metals, where the orbital moment is quenched, and opens the door to a new field of research known as "spin-orbitronics".

1.2 Outline

The main goal of this thesis was to produce vertical transport device structures and exploit the magnetic properties of the rare earth nitrides. In order to pursue this, the geometry that has been developed has two crossed contacts. Vertical transport through thin REN and group III-nitride layers occurs at a junction formed where the contacts cross. This thesis is organised into four main chapters succeeding this one as follows:

- Chapter 2 reviews the physical properties of the rare-earth nitrides and gives an overview of the current state of the field.
- Chapter 3 focuses on the experimental methods used during this project.
- Chapter 4 presents results from rare-earth nitride tunnelling devices prepared with GdN electrodes.
- Chapter 5 presents results from rare-earth nitride tunnelling devices with one samarium nitride electrode.
- Chapter 6 presents results on magnesium doping of epitaxial GdN thin films.

Following these chapters is a broad conclusions chapter and appendices detailing the derivation of the Simmons model for tunnelling, and supplementary experimental details.

Chapter 2

Properties of Rare-Earth Nitrides

2.1 Historical Overview

The rare-earth nitride series first gained significant interest mid last century, encouraged by developments in lanthanide separation [18–22]. Subsequent progress was slow and the growth of high quality samples was hampered by poor stoichiometry and the materials' propensity to oxidise in ambient conditions. The magnetic behaviour and crystallographic structure of the series was relatively well characterised using these early samples, but with varied electrical transport data. The RENs form in the rock salt crystal structure[1] with lattice constants of order 5 Å. Once bonded with nitrogen the rare-earth atoms give up their *5-d* electrons, the *4-f* electrons are highly localised, meaning that the ionic radius is comparable[2] to that of the nitrogen ions as depicted in Figure 2.1 for GdN.

More recently, the REN series has regained interest with advances in film growth and characterisation. Modern thin-film growth techniques that have been applied to the rare-earth nitrides include molecular beam epitaxy, sputter deposition, and pulsed laser deposition [24–29]. These high quality samples are prepared in ultra-high vacuum, permitting very low impurity concentrations and high surface quality. Typically the metal is allowed to react in the presence of ultrapure

[1] Space group Fm3m.

[2] The 1.078 Å ionic radius is slightly smaller than that of nitrogen (1.32 Å) [23].

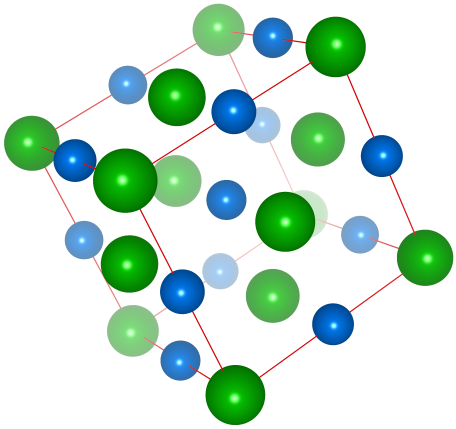

Figure 2.1 – Diagram of the rock salt crystal structure of GdN. Here blue spheres represent gadolinium ions while green spheres represent nitrogen ions.

nitrogen which may take the form of N_2 or as a nitrogen plasma or ion beam. This accompanies modern theoretical studies of the band structure and magnetic interactions, made more tractable by their simple rock salt structure. These studies have corroborated the earlier magnetic and crystallographic measurements, but have revealed that many of the early studies which found RENs to be semimetallic were probably due to poor stoichiometry. It is now widely accepted that many of the RENs are in fact semiconductors [12, 13, 25, 27, 30–34], although this remains somewhat controversial.

Two notable reviews which may be consulted for further information regarding the rare-earth nitride series are those of Duan *et al.* and the more recent review of Natali *et al.* [24,35]. The following sections will give an overview of the theoretical and experimental electronic properties of the rare-earth nitrides. The magnetic properties will then be examined with a strong focus on GdN and SmN, both because they are two of the most widely studied RENs, and because they are the rare-earth nitrides which have been incorporated into devices during this PhD project.

2.2 Electronic Structure

2.2.1 Theoretical Picture

Theoretical studies of the electronic structure of the REN series are numerous. The strong exchange interactions and correlated nature of these materials present a challenging testing ground which is used to this day to help refine density functional theory (DFT)-based computation methods. The basic electronic structure is determined by symmetry considerations, with the overall shape of the energy bands being similar between studies, having the valence band (VB) maximum at Γ and the conduction band (CB) minima at X. The band structure of ferromagnetic GdN extracted from one study is displayed in Figure 2.2. In this figure the red lines represent those bands which have a strong *4-f* character. Here the occupied *4-f* levels lie near -8 eV and the empty *4-f* levels lie close to 5 eV. The presence of the half-filled *4-f* band induces exchange splitting in the GdN VB and CB. The majority spin polarisation in the CB and VB follows the spin polarisation in the filled *4-f* levels. This exchange splitting is shown by the solid and dashed lines in Figure 2.2 which correspond to the majority and minority spins, respectively. Note that the splitting of the bands is of opposite sign for the CB and VB, giving both band edges the same spin polarisation. In the paramagnetic state, magnetic ordering is lost and the exchange splitting vanishes.

One of the most important features of the band structure is whether or not there is a finite band gap. Semiconductors are characterised by having a gap in their electronic energy levels. This gap may be direct, with the CB minimum and VB maximum occurring at the same crystal momentum. The band gap can also be indirect, such as is the case in the RENs, with the CB minimum and VB maximum occurring at different crystal momenta (see Figure 2.2). A semimetal occurs when there is a small overlap of the CB minimum and VB maximum. In this case there are extended states at the Fermi level (making it metallic), however the overlap occurs at different crystal momenta so that there is a finite direct band gap but no indirect gap. For comparison, the band structure of GdN has been included as Figure 2.3 for two calculations with different parameters; on the left is a calculation

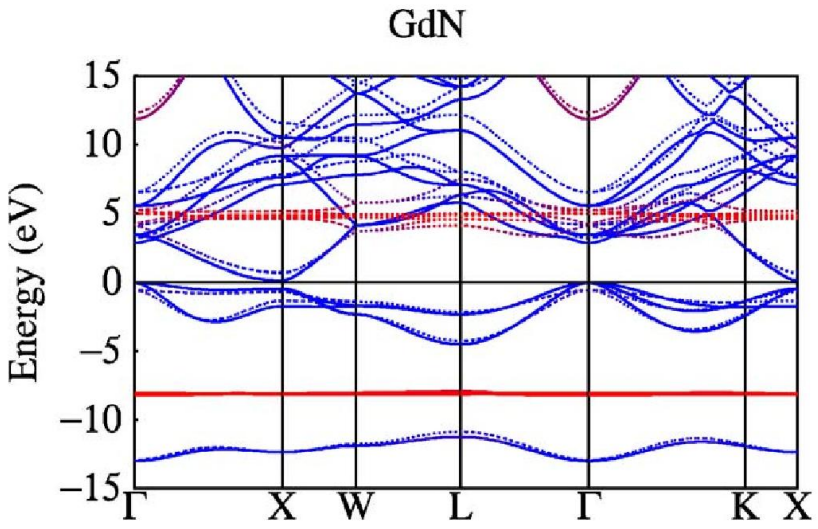

Figure 2.2 – Calculated band structure of GdN in the ferromagnetic state. Majority spin bands are represented by solid lines and minority spin by dotted lines. Figure reproduced from Larson *et al.* [1].

which finds a small overlap (semimetal) of the CB and VB, while on the right is a calculation which finds GdN to be a semiconductor.

Band gaps estimated by theoretical studies vary considerably, and the predicted band overlap (or lack thereof) between CB and VB is where many predictions disagree with modern experimental results. The extent of the band gap overlap (if any) is influenced by the location of the *4-f* bands. Early calculations of the Gd and La pnictide band structure appeared alongside the development of DFT in the 1980s. These first studies used a simple method of treating the *4-f* electrons as if they were core electrons, tightly bound to the rare-earth nucleus [36, 37]. They found that the CB and VB overlapped in GdN, which is a result reproduced in several more modern studies including Local Spin Density Approximation (LSDA) using the Linear Muffin-Tin Orbital (LMTO) method [38], although in the latter case GdN is found to be semiconducting in the paramagnetic state and semimetallic only in the ferromagnetic state. Another method brought to bear on the RENs is self interaction correction (SIC) LSDA, where a potential caused by the

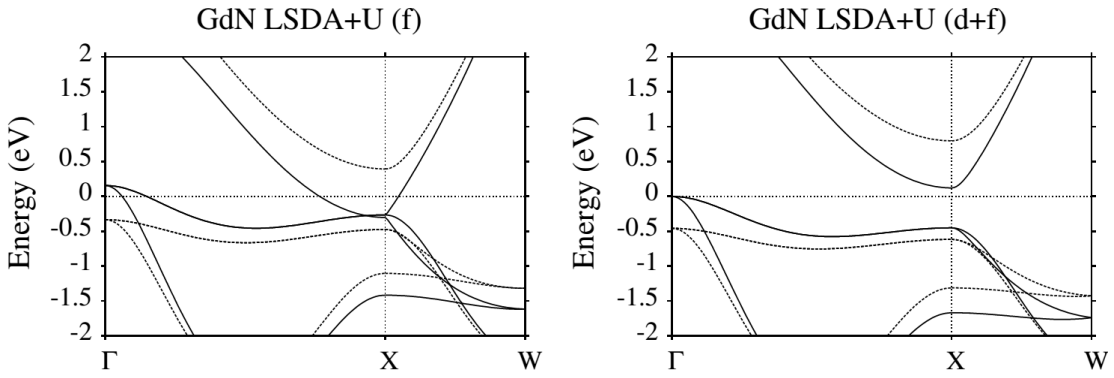

Figure 2.3 – LSDA+U calculation of the GdN band edges in the ferromagnetic state with U_f (left, semimetallic) and $U_f + U_d$ (right, semiconducting). Solid lines: majority spin; dashed lines minority spin. Figure reproduced from: Larson and Lambrecht [2].

localised f-electrons is corrected for [39, 40][3]. The band gap found by SIC-LSDA is small or nonexistent for all members of the REN series. More modern LSDA+U treatments predict that many of the RENs are semiconductors [1]. Note that in this case U, which accounts for inexact treatment of the Coulomb repulsion, is made up of two components: U_f which accounts for the localised character of the *4-f* electrons, and U_d which is an empirical correction serving to shift the empty d-states up relative to the filled ones (see Fig. 2.3). The most advanced technique employed to date is Hedin's GW approach [41, 42] where G stands for Green's function and W stands for Coulomb interaction. This GW method finds a small band gap for GdN in agreement with experiment. The electronic and magnetic structure of other members of the series are somewhat harder to calculate, with GdN being a special case due to its entirely spin magnetic moment induced by

[3]This potential exists for all electrons, but is most relevant for highly localised electrons such as the *4-f*s because they "self-interact" the most. In Hartree-Fock theory the Coulomb interaction of the electron with itself is cancelled by a self-interaction term in the exchange contribution to the Hamiltonian. In DFT under LDA the cancellation is incomplete due to the approximate treatment of the exchange and electron correlations.

a half filled *4-f* band. The semiconductivity found with refined methods is at odds with historical measurements and predictions which found many RENs to be semimetallic, but is consistent (by construction of U_d) with recent experimental studies [24].

The experimental disagreement is most likely due to slight nitrogen deficiencies in early bulk samples resulting in a slight off-stoichiometry. The effect of the stoichiometry on the electronic properties can readily be assessed. For a nitrogen density of $\sim 1 \times 10^{22}$ cm^{-3}, and if each nitrogen vacancy contributes just 1 electron to the lattice, only $\sim$1 % of the nitrogen sites need to be vacant for a carrier concentration of $\sim 10^{20}$ cm^{-3} to be realised. Carrier concentrations of this magnitude or lower are common amongst the series [16, 26, 30]. Intentionally including nitrogen vacancies produces carrier rich samples; with a large shift in the Curie temperature of GdN when significantly nitrogen deficient films are prepared [43].

2.2.2 Experimental Picture

Recent experimental results are aided by advances in thin-film growth. Techniques that have been used to grow high quality REN thin-films include molecular beam epitaxy, sputter deposition and pulsed laser deposition [25, 27–29, 44, 45]. These samples are prepared in high vacuum, which permits very low impurity concentrations and high surface quality. The metal is reacted with ultrapure nitrogen either as N_2 gas, NH_3 or in an ionised form. The results from these high quality samples have resulted in accumulating evidence suggesting that the rare-earth nitrides contain several ferromagnetic semiconductors [30–32, 46], an overall sparsely populated class of materials.

Within the series GdN is the most widely studied with its large 7 μ_B magnetic moment originating entirely from electron spin in the half-filled *4-f* shell [24]. Detailed magnetic measurements reveal that GdN is a ferromagnet below a 50-70 K Curie temperature [26, 30, 45]. Undoped GdN samples exhibit semiconductor-like resistivity at low temperatures [30], corroborated by a clear optical gap of 1.3 eV at room temperature which is red-shifted to 0.9 eV at low temperatures due to the onset of band splitting [47]. The temperature coefficient of resistance (TCR)

in films prepared with low nitrogen vacancy concentrations is typically negative, suggesting carriers are thermally activated from an impurity band located close to the CB minimum [30]. This is supported by photoconductivity studies which show that the carrier concentration can be controlled optically, with a persistent component originating from trap levels located within the band gap [16]. An example of the measured temperature dependent resistivity is shown in Figure 2.4 for GdN. A schematic diagram of the conduction band and donor level is included. As the temperature is decreased the GdN resistivity increases due to the thermally activated nature of the carriers until just below T_C where the resistance decreases. This decrease in the resistance corresponds to the onset of exchange splitting of the conduction band which breaks the degeneracy between spin up and down states. Below T_C the majority spin band experiences a decreased activation energy, resulting in a decrease in the resistivity of the material [47]. Well below T_C the resistance again increases in a thermally activated manner, albeit with a smaller activation energy than above T_C.

Like GdN, samarium nitride has also received significant attention. This is largely due to its interesting magnetic properties originating from spin and orbital contributions, which will be discussed further in Section 2.4. Studies of the electronic properties of SmN thin films point to it being a semiconductor [48]. Like GdN the TCR is negative for samples prepared with low nitrogen vacancy concentrations. Heavily doped samples also exhibit novel superconductivity at low temperatures [49].

Within the series several other rare-earth nitrides have received attention during a period of increased interest in the last 10 years. Dysprosium nitride has been studied both as a material and in device applications as a spin filter [13]. Interest in this material is increased due to the large magnetic moment offered by a Dy^{3+} ion [1]. DyN has both a negative TCR and an optical gap of 1.2 eV pointing toward it being semiconducting in nature [31, 34, 48]. Another member of the REN series, EuN, has been found to be an interesting semiconductor with a gap of 0.9 eV [50]. Nitrogen vacancies formed during the growth convert some of the Eu from Eu^{3+} to Eu^{2+}, and then the large 7 μ_B magnetic moment of the

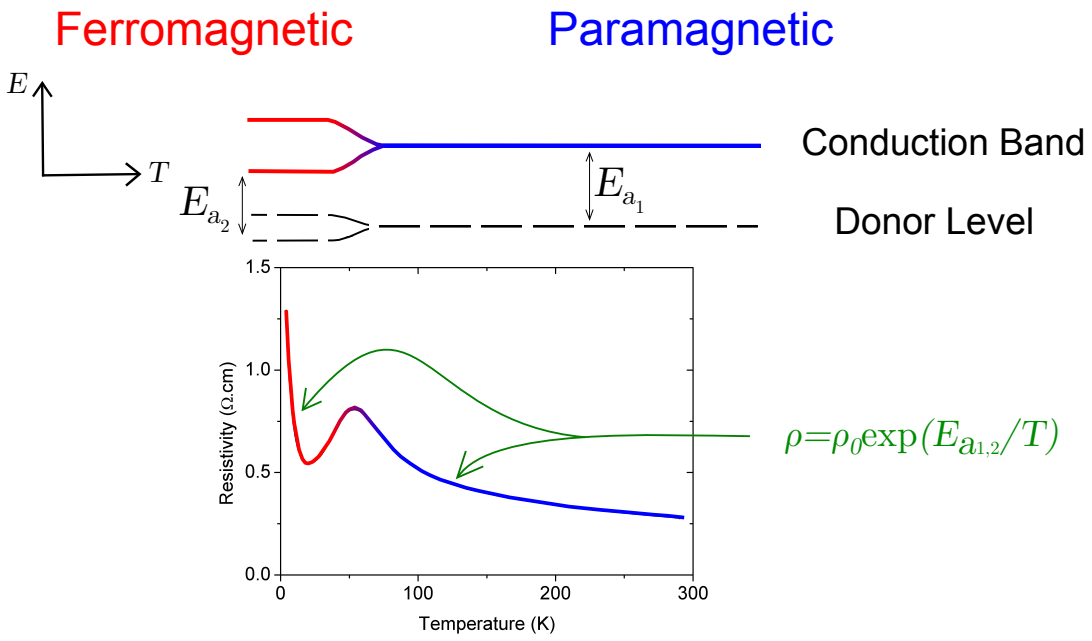

Figure 2.4 – Schematic diagram of the GdN conduction band splitting along with the temperature dependent resistivity of a GdN sample.

Eu^{2+} ions makes nitrogen deficient EuN of interest as a novel dilute magnetic semiconductor [32]. Although other RENs can be grown with inert nitrogen gas, the chemical properties of Eu require the use of an activated nitrogen source. Like europium, Yb has a propensity to form compounds in either the Yb^{2+} or Yb^{3+} charge states, offering the same potential for the magnetism of YbN samples to be controlled by altering the nitrogen vacancy concentration. However, in contrast to Eu it is only the Yb^{3+} ions that carry a magnetic moment, and the *4-f* magnetic moment of Yb^{3+} is smaller than that of Eu^{2+}. This divalent/trivalent competition also means that in thin films Yb metal will only react with ionised nitrogen to form a nitride [51]. Early (1960s) electrical transport studies of YbN yielded a positive temperature coefficient of resistance (TCR), suggesting metallic behaviour [22]. The results were supported by a thorough study of the electronic structure of bulk YbN samples in the 1990's where optical spectroscopy, specifically infrared absorption, gave further evidence for a semi-metallic band structure [52]. However

these older studies are again, like many other rare-earth nitrides, at odds with both recent experimental and theoretical considerations which suggest that YbN may be a semiconductor [1, 51].

The rest of the series have received less attention, but the prospect of combining RENs with strongly contrasting magnetic properties places a premium on studies of other members of the series. While the picture of the electronic structure of the RENs is still not entirely clear, there is a growing body of evidence to support the semiconducting nature of most members of the series. Undoubtedly, future studies will continue to shed light on this group of materials; elucidating their detailed conduction properties and by doing so challenge both theoretical and experimental techniques.

2.3 Magnetic Properties of Rare-Earth Nitrides

Magnetism within the rare-earth nitride series results from both spin and orbital contributions. In order to understand how these contributions are partitioned Hund's rules must be examined. The magnetic properties of the RENs have received significantly less theoretical attention than the electronic properties. There have been several studies investigating the exchange mechanisms in RENs [53–55], however the existence of carrier mediated ferromagnetism remains an open question [56]. Several of the ground state magnetic moments are also in disagreement with theoretical Hund's rule free-ion values [57, 58]. Undoubtedly as the experimental picture becomes clearer, this will aid theoretical studies and methods to understand the rich magnetic properties offered by the RENs.

The magnetism of the RENs originates from the quantum mechanical behaviour of electrons (namely the *4-f* electrons) surrounding each RE nucleus. Electrons have both spin and orbital angular momentum. The spin and angular momentum quantum numbers describe the allowed values that the spin and orbital angular momentum can take.

The total orbital angular momentum quantum number, L, is given by $L^2 = \hbar^2 l(l+1)$ where l is the angular momentum quantum number. l is related to the

quantum mechanical orbital in which the electron is confined; a naive viewpoint is to consider this to be related to the electron orbiting around the nucleus although in reality this is little more than a convenient way to visualise it.

The total spin quantum number, S, is given by $S^2 = \hbar^2 s(s+1)$ where s is the spin quantum number and is an intrinsic property of electrons. Each electron has $s = 1/2$, and as an orbital is filled each electron can have a spin projection (m_s) of $\pm 1/2$.

The total angular momentum quantum number is $j = |l \pm s|$. This gives the total angular momentum through the relation $J^2 = \hbar^2 j(j+1)$.

2.3.1 Hund's Rules and Magnetism

Hund's rules tell us what L and S are so that J and then the magnetic dipole moment of an individual RE atom can be determined [59]. Hund's rules are based on empirical observations of the electron interactions and magnetic moments of free ions. They are useful for qualitative analysis, however in general other effects in solids such as the crystal field must be taken into account[4] [57]. The first two rules arise from the Pauli exclusion principle and Coulomb repulsion, and the third is a result of the effects of spin-orbit coupling.

- Hund's first rule states that the total spin quantum number S is maximised. This implies that each orbital is first filled with electrons of one spin orientation (conventionally spin up).

- The second rule serves to maximise L, the total orbital angular momentum quantum number[5]. This means that orbitals are populated starting with the highest possible m_L values (m_L is the quantum number associated with the

[4]The crystal field is a static electric field produced by the surrounding charge distribution. In the rare-earth nitrides this is due to the nitrogen ions surrounding each RE ion.

[5]There is a slight modification to Hund's second rule that is invoked in the literature for the rare-earth nitrides. Namely that L_Z is the maximised quantity, which breaks the cubic symmetry and lowers the total energy (the exceptions being EuN and YbN where the cubic solution minimises the total energy) [1].

projection of the orbital angular momentum about the quantisation axis). For the rare-earth f-electrons with $l = 3$, m_L=3,2,...,-3.

- The third rule minimises J (the total angular momentum quantum number) for less than half filled orbitals ($J = |L - S|$), and maximises J for orbitals that are more than half full ($J = (L + S)$).

Figure 2.5 depicts how the magnetic moment is made up from the spin and orbital components for each member of the rare-earth nitride series. Here the magnetic moment is obtained from the expectation value of $\mu_B(\vec{L} + 2\vec{S})$, where μ_B is the Bohr magneton and $\vec{L}, \vec{S}$ are the orbital and spin angular momentum vectors[6].

Spin and orbit are coupled to one-another by a relativistic effect called spin-orbit coupling, breaking the degeneracy between states of different total angular momentum. S and L can be used in order to evaluate the magnetic moment associated with each atom. The total angular momentum is given by:

$$\vec{J} = \vec{L} + \vec{S}$$

The magnetic dipole moment is given by:

$$\vec{\mu_L} = g_J \mu_B \vec{J}/\hbar$$

where μ_B is the Bohr magneton, $\vec{\mu_L}$ is the magnetic dipole moment and g_J is the Landé g-factor given in Equation 2.1. This factor arises when a first order perturbation in the energy of an atom in the presence of a weak magnetic field is taken. It can be found as outlined in many textbooks [59]. Making the common approximation that $g_S = 2$ yields

$$g_J \approx \frac{3}{2} + \frac{S(S+1) - L(L+1)}{2J(J+1)}. \tag{2.1}$$

[6]The factor of 2 arises because the electron g-factor is approximately 2 for spin angular momentum and 1 for orbital angular momentum. This means that the spin angular momentum is twice as good at producing a magnetic moment than the orbital angular momentum.

2.4 Magnetic properties of SmN and GdN

Turning back to the rare-earth nitrides with Hund's rules in mind, it is possible to explore the rich magnetic properties offered by the contribution of their orbital magnetic moments. Moving across the series, the light rare earths first fill their *4-f* orbitals with one spin-orientation, maximising S for GdN which has a half-filled orbital. The largest orbital magnetic moments occur when the atomic orbital is one or three-quarters filled. Figure 2.5 illustrates this and includes the spin, orbital and total magnetic moments of members of the REN series. Importantly, for the light rare-earths Fig. 2.5 illustrates that the spin and orbital components of the magnetic moment are aligned *opposite* due to Hund's third rule[7].

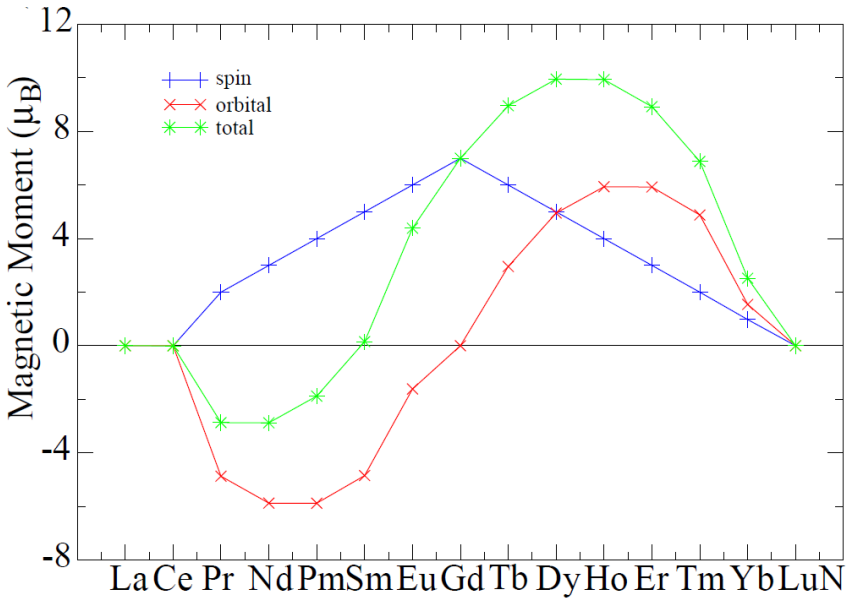

Figure 2.5 – Total, orbital and spin components of the magnetic moment in the rare-earth nitride series. Figure reproduced from Larson *et al.* [1].

Focusing now on two members in particular, the very different magnetic prop-

[7]Note that in Figure 2.5 the magnetic moment is plotted rather than the quantum numbers. For the light rare earths L is maximised, but the orbital component of the magnetic moment is negative due to Hund's third rule.

erties present within the series can be illustrated. GdN has no orbital magnetic moment, a large spin moment of 7 μ_B, and in this way is very similar to conventional transition metal magnetic ions where the orbital moment is quenched. GdN becomes ferromagnetic below 50 K with magnetic polarons increasing this to 70 K in the case of doped samples [60]. GdN has a coercive field of some tens to hundreds of Oersted depending on the growth conditions and crystalline quality of the films [44,45]. This small coercive field owes to the entirely spin-based magnetic moment with no orbital contributions. This means that there is weak coupling to the crystal lattice so the magnetic moment can easily reorient in response to an applied magnetic field.

SmN could hardly be more different, the orbital and spin magnetic moments are of similar size. According to Hund's third rule they anti-align resulting in a small net moment. Below 27 K SmN becomes ferromagnetic [46], with a near-zero magnetic moment of only 0.035 μ_B . Because SmN has a vanishing magnetic moment while still possessing full spin alignment, it could be used as a magnetic fringe field free spin-injector element. To make things even more interesting, it is in fact the orbital magnetic moment which dominates slightly in SmN [46, 61]. This orbital dominant magnetism results in interesting phenomena such as twisted magnetisation phases when GdN and SmN are grown in multilayer structures [17].

In SmN, as in other RENs, the conduction band is *5-d* like in nature and is spin polarised by the *4-f* electrons. The net magnetic moment follows the orbital component and so exhibits the unusual property that the spin moment will align *opposite* to an applied magnetic field. It is the spin moment which spin-polarises the conduction electrons so the spin-polarisation in SmN is thus expected to be opposite to that of conventional spin-based ferromagnets. This has interesting implications for electronic devices because the transport properties of devices are expected to follow the spin polarisation rather than the magnetisation. The spin polarisation of SmN is expected to align opposite to that of GdN, meaning that the two materials could be played off against one-another in a device. GdN also has a conduction band which is *5-d* like in nature, but unlike SmN it is spin-polarised parallel to the net moment. SmN has a large coercive field as high as 6 T at 5 K

which makes it significantly magnetically harder than GdN which has a coercive field as low as 10 Oe [24, 46].

2.5 Potential Applications of Rare-Earth Nitrides

By exploiting the magnetic properties of rare-earth nitrides they may be used in a variety of different devices. The large spin-polarisation has already seen RENs being employed as spin filters [12–14]. Recent pushes towards spin-transfer torque based devices could benefit from the inclusion of magnetic semiconductors. Another avenue of investigation involves controlling the magnetism of magnetic semiconductors through applied electric fields, which promises to require even lower switching energies than spin transfer torque [62].

One long sought after device is the elusive Datta-Das transistor which is the solid-state equivalent of the electro-optic modulator [63]. The Datta-Das transistor consists of two spatially separated magnetic electrodes in contact with a semiconducting spin channel with a long spin-diffusion length (e.g. GaAs). As the spin polarised current injected from one electrode passes through the spin channel, it is exposed to a potential bias applied by a gate. By tuning the size of this bias the spin of electrons can be rotated via Rashba spin-orbit coupling. The resistance of the device is then governed by the spin direction of electrons arriving at the second magnetic drain electrode. Electrons arriving at the drain with a parallel spin are transmitted, whereas conduction is inhibited if they arrive with spin anti-parallel to the polarisation of the drain electrode. To date there have been many difficulties in producing a working Datta-Das transistor, primarily due to the large band offset and resistivity mismatch which occurs at the interface between the (metallic) magnetic electrode and the (semiconducting) spin-channel. Magnetic semiconductors present an obvious opportunity to overcome these challenges. Their Fermi level (and hence band offset) can be aligned with the spin channel in order to improve spin injection efficiency and mitigate impedance mismatch. Further to this, the use of a fringe field free spin-polarised material such as SmN may also improve spin coherence in the conduction channel.

Even established fields of research could benefit from the inclusion of magnetic semiconductors such as the rare-earth nitrides. They offer promise in magnetic tunnel junctions, a device which may be switched between high and low resistance states based on the magnetic orientation of two layers separated by a thin insulating barrier. In this case the large spin polarisation and contrasting magnetic hardness offered by members of the REN series may result in large tunnelling magnetoresistance values, potentially improving device performance or opening up new functionality. Of particular interest are systems such as SmN where the spin and orbital moments cancel, resulting in zero net moment. Such materials offer promise in devices as they are free from stray fields and relatively immune to demagnetising forces, making them of interest in densely packed memory elements. The critical current required to switch a magnetic random access memory element using spin transfer torque is expected to be proportional to the saturation magnetisation of the free layer, which has further enhanced interest in zero moment ferromagnets [64, 65].

Chapter 3

Experimental Methods

3.1 Film Growth

Thin films prepared for this project were grown in ultra high vacuum systems using molecular beam epitaxy (MBE) for epitaxial samples or physical vapour deposition (PVD) for polycrystalline films. The main differences between the two techniques are the choice of substrate and substrate temperature during the growth. High temperatures permit adatoms to rearrange on the surface into a single crystal and thus are more conducive to epitaxial growth. Nitrogen gas (or an ionised nitrogen plasma) is introduced into the chamber and reacts with rare-earth atoms deposited onto the surface by an electron gun or thermal evaporation source[1]. Typical substrates for polycrystalline growths are sapphire or silicon wafers, and these are coated with a buffer layer of epitaxial GaN or AlN for growth of epitaxial RENs. REN films are highly susceptible to oxidation when exposed to air. Thus it is imperative that they be passivated with a capping layer such as GaN or AlN. Both of these materials are chosen for their high hardness, stability in air, high electrical impedance and transparency over the visible spectrum. AlN and GaN are grown using activated nitrogen supplied by a Kaufman ion source. When transparent capping layers are not required, amorphous silicon or germanium may

[1]The catalysis mechanism by which the nitrogen bonds are broken when N_2 gas is used is poorly understood and is an ongoing topic of research.

be employed. Silicon and germanium capping layers have the advantages that they are not susceptible to problems with stoichiometry and do not risk exposing the surface of the rare-earth nitride layer to energetic nitrogen ions.

There has been a focus in recent years on growing high quality epitaxial thin films of rare-earth nitrides. Unlike polycrystalline growths which occur at room temperature, epitaxial growth must be performed at temperatures of several hundred degrees in order to allow for re-arrangement of surface adatoms. Epitaxial compatibility with group-III nitrides has been demonstrated by growing onto the (111) face of GaN and AlN [25,32,44,45,66], which have acceptable lattice matches for the rare-earth nitrides. InN would be a near perfect lattice match, however it is not commercially available. MgO and Yttria Stabilised Zirconia (YSZ) have also been successfully used to grow epitaxial RENs[2] [26, 67].

The samples grown during this project have been prepared using a Thermionics ultra high vacuum deposition system which is illustrated schematically in Figure 3.1. Clean substrates are first mounted onto a molybdenum substrate holder using either molybdenum clips (for high temperature growths) or polyimide tape (for low temperature growths). This substrate holder is then installed into a load lock which allows for sample introduction and removal without necessitating venting of the growth chamber. The load lock is sealed and evacuated using rotary and turbo pumps for several hours before transferring the sample into the growth chamber. The transfer is conducted using a magnetically-coupled linear transfer arm, the end of which interfaces with grooves on the substrate holder. The sample manipulator inside the growth chamber has a second set of clips which interface with another set of grooves on the holder. This permits transfer of the sample holder into the growth chamber by rotation of the manipulator. The transfer arm is then retracted and the load-lock sealed during the growth. Once the transfer process is complete, substrates may be outgassed if a high temperature growth is to be undertaken. This is performed using a resistively heated tungsten filament

[2]In the case of YSZ the first few monolayers form as an oxide due to oxygen ion diffusion through the YSZ at high temperatures. Prolonged deposition results in high quality REN growth as evidenced by a relaxation of the lattice constant.

in close proximity to the substrate holder.

The growth is then performed using the deposition sources available in the system: a 4-pocket electron gun facilitates the high temperature evaporation of metals while an effusion cell and resistively heated thermal source may be used to deposit Al and Sm, respectively. Ultra high purity nitrogen gas is introduced into the chamber using a mass flow controller and, if desired, ionised using a Kaufman ion source. The deposition rate is monitored *in-situ* by one of two quartz crystal microbalances. For high temperature growths the substrate heater is employed to heat the substrate holder to several hundred degrees. A linearly actuated shutter protects the sample from deposition until the growth commences. Several of the sources also have shutters to prevent deposition while they are kept hot during multilayer growths. During the growth the pressure inside the chamber is monitored using a cold cathode gauge and the composition of residual gases can be analysed using a Pfeiffer quadrupole mass spectrometer. Further details regarding film growth may be found in the relevant results chapters of this thesis.

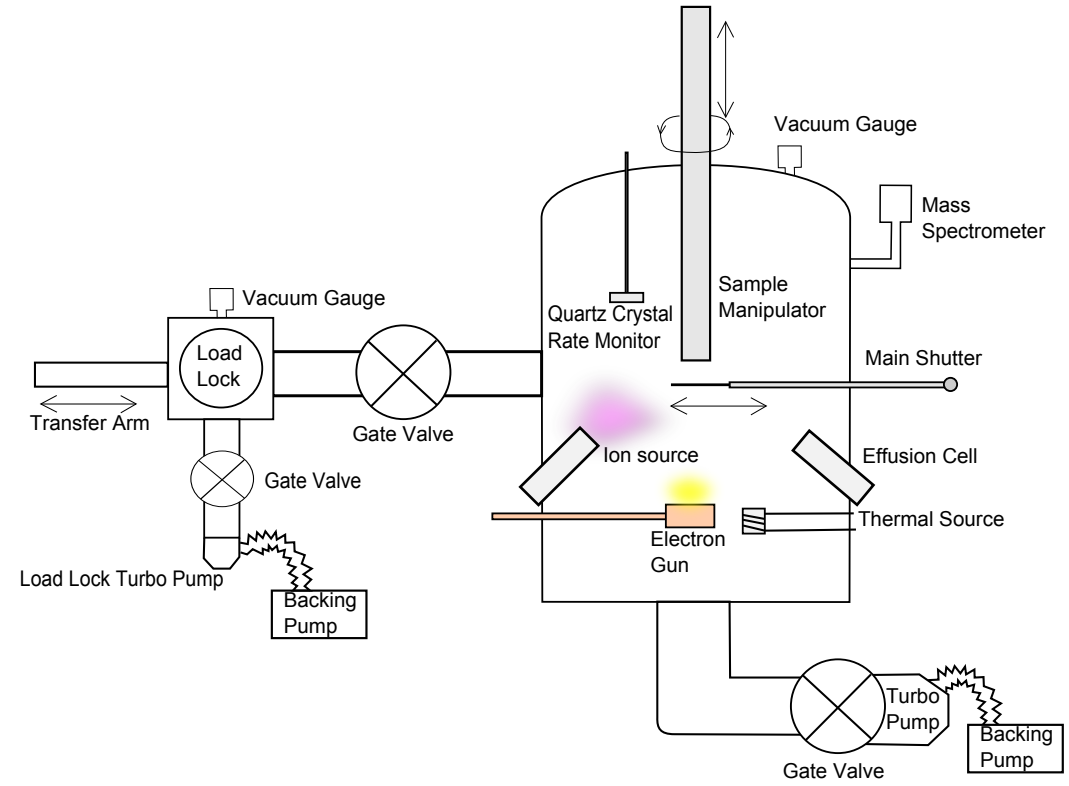

Figure 3.1 – Schematic diagram of an ultra high vacuum deposition chamber used for rare-earth nitride growth.

3.2 Photolithography

Both shadow lithography and photolithography can be used to produce patterned samples. In both cases, a pattern is formed by selectively exposing different areas of the sample to deposition while protecting others. In the case of shadow lithography, this is done with a mask held in proximity to the surface. Photolithography relies on a thin polymer layer coated onto the surface of the sample. Photolithography defines patterns, both for devices and electrical contacts, much more precisely than shadow lithography and is suitable when high temperature growths are not required. In this thesis photolithography is used extensively to produce devices in a cross-contact geometry. Here two thin layers are grown perpendicular to one another and a junction permitting vertical transport studies is formed at their crossing.

The photolithography process relies on a polymer, known as a photoresist, which is sensitive to ultraviolet light. By using a mask to control which regions of the photoresist are exposed to UV light[3], the polymer in these exposed areas can be made to respond selectively to a developing chemical. This developer removes some of the photoresist and exposes the bare substrate beneath. Depending on the resist used the photoreaction most commonly relies on conversion of the photoresist into a more alkaline soluble material such as a carboxylic acid, or a polymer cross-linking process [68]. Photolithography has a resolution limit of order 1 μm, primarily due to the diffraction limit of light. In some industrial cases this is pushed into extreme UV in order to minimise the photon wavelength [69], and in other cases electrons are used in a process known as electron beam lithography to produce patterns on the nanometre scale [70]. In this project, with the primary focus being proof of concept devices, a more conventional mercury arc lamp is used with a common photoresist. The maximum resolution expected from this system is ~ 2 μm, which

[3]The mask has features in a ratio of 1:1 and can be in either a positive or negative configuration depending on the resist used. These masks are produced by etching from a continuous film of metal deposited on a transparent soda glass substrate. The mask is printed either using electron-beam lithography or by using a laser writer which writes the pattern into photoresist using a tightly focused GaN UV-laser.

is superior to shadow lithography.

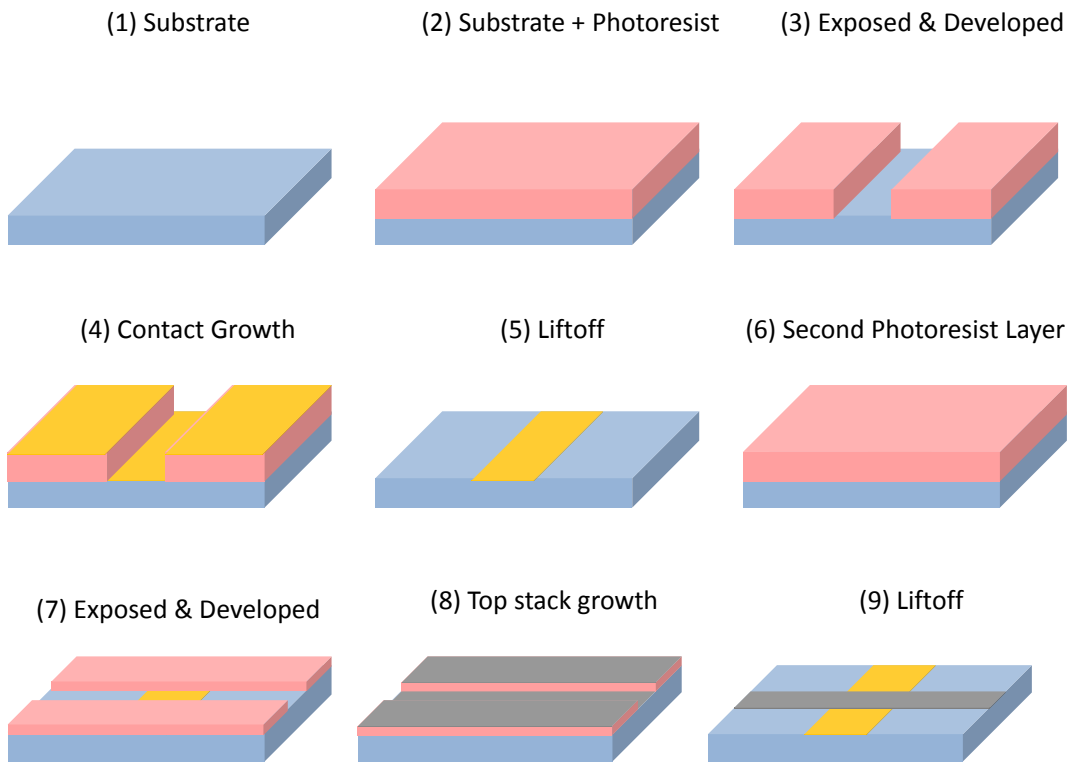

Figure 3.2 – Schematic flowchart of the photolithography method used to grow samples in the cross-contact geometry.

The photolithography process is as follows:

1. If desired, the substrates are first cleaved using a diamond pen. Typically 1 cm^2 sized pieces are used.

2. The substrates are cleaned with instrument grade acetone followed by instrument grade isopropyl alcohol, then dried using nitrogen gas[4].

[4]Instrument grade (or better) solvents must be used here, as contaminants present in drum solvents can cause striations and other defects within the photoresist.

3. AZ1518 photoresist is applied by clean pipette to the substrates and then spin-coated for 60 s at a rotational speed of 4000 RPM. During this step it is important to ensure that no air bubbles are applied to the substrate, as such spume will cause imperfections in the spin coated layer. It is also important to ensure that the entire substrate is coated with photoresist in order to prevent defects at the corners.

4. The photoresist is baked at 95°C for 2 minutes in order to remove solvents present inside the film. This step improves resist adhesion to the substrate, prevents the resist from sticking to the mask during the next step and prevents N_2 bubbles from forming during exposure.

5. After baking, the substrate is then transferred into the Karl Süss MJB3 mask aligner to be exposed. A mercury lamp provides UV light which is used to expose the photoresist for 7.5 s. The exposed pattern is defined by a photomask made from Cr-coated soda glass.

6. A solution of 3:1 AZ-326:H_2O is then used to develop the pattern for 35 s. AZ-826 may be used if a developer with surfactant properties is required. During this step, slight agitation of the substrate helps to produce optimal results as developed photoresist must be allowed to migrate away from the patterned region. The developer is a pre-diluted solution of tetra methyl ammonium hydroxide[5].

7. To stop the develop process before over-development occurs, and to remove developed material, the sample is rinsed with deionised water (18.2 $M\Omega\,cm$) and dried with nitrogen gas.

8. Following deposition of metal and/or nitride layers into the developed pattern, the remaining photoresist can then be removed using instrument grade acetone. This step can be done with or without sonication of the solvent solution. Care must be taken here with sonication when small features are

[5]AZ-326/AZ-826 should be avoided if layers containing Al species are being processed, as the hydroxyl groups aggressively attack aluminium ions and cause rapid etching.

desired as this process can easily damage patterned films. Removal of the photoresist reveals the patterned material in the geometry described by the photomask.

A schematic diagram of this process is included as Figure 3.2 for a multiple step process by which tunnel junctions are fabricated. An animated version of the process appears as Figure F.1. First a layer of photoresist is spin coated on and developed to reveal a channel into which the bottom contact is grown. The photoresist is then lifted-off and another photoresist layer used to define the second pattern. The second layer, comprised of the tunnel junction stack along with the top contact, is then deposited. After deposition of the second layer, the second photoresist layer is lifted-off and the cross-contact geometry tunnel junction is revealed. For full details of these samples refer to Section 4.2.2. The rare-earth nitrides are sensitive to oxidation via water, and for this reason a bottom-up growth method was developed to avoid exposure to hydrated solvents.

3.3 Characterisation Methods

A number of different techniques have been employed throughout this project to characterise the structural, electronic and magnetic properties of rare-earth nitride thin films and devices, as described below.

3.3.1 Temperature Dependent Resistivity

The temperature dependent resistance is measured in a helium closed-cycle cryostat at temperatures down to 4 K, which is shown schematically in Figure 3.3. For resistivity measurements a four-terminal geometry is employed to negate resistance components from the leads and/or contacts to the sample. For bulk layers measurements are performed in the van der Pauw geometry [71]. In this measurement regime, for a square sample, the sheet resistance (R_s) is given by

$$R_s = \frac{R\pi}{\ln(2)}.$$

The resistivity is then given by multiplying by the thickness (t)

$$\rho = R_s \cdot t. \tag{3.1}$$

When this technique is applied to rare-earth nitrides the form of the temperature

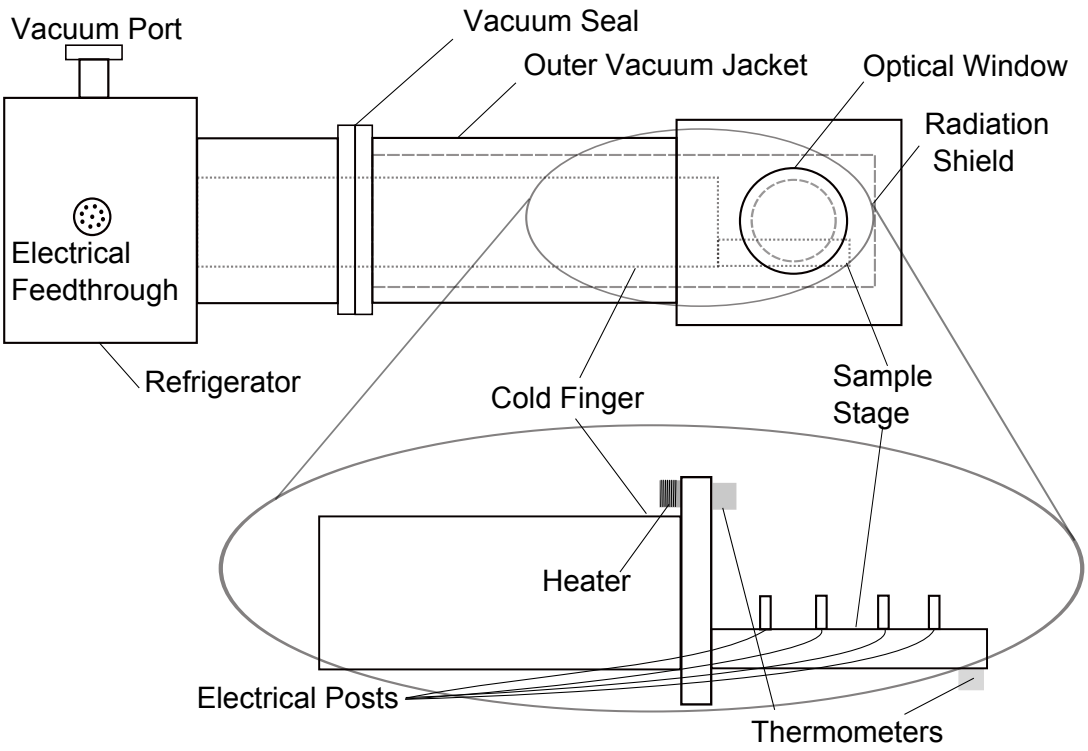

Figure 3.3 – Schematic diagram of the closed cycle cryostat used for resistivity measurements. The lower portion of the diagram is an expanded view of the sample stage.

dependent resistivity differs from conventional semiconductors. An example of the measured temperature dependent resistivity of GdN is included as Figure 2.4 in Section 2.2.2.

3.3.2 Operation of the Helium Closed-Cycle Cryostat

The closed-cycle cryostat used for resistance measurements operates by compressing helium gas, and in essence it is a refrigerator with the refrigerant being helium. The cryostat is kept under vacuum when in operation to prevent heat flow through conduction and convection. An inner reflective shroud, referred to as the radiation shield, is held at a temperature of $\sim$30 K and prevents radiative heat input. On the end of a copper cold-finger is attached a copper stage to which samples are mounted.

For most measurements a small copper block is heatsunk to the copper stage, as depicted in Figure 3.4. The copper block has four cantilevered clips to mechanically make electrical contact to the sample[6]. The sample is then placed on top of the copper block with thermal grease suitable for cryogenic applications (Apiezon-n) underneath to ensure good thermal contact. Thermal grease layers should be as thin as possible to ensure optimal thermal contact[7]. The four cantilevered clips can then be screwed down onto the top of the sample. The clips are soldered to wires connected to four out of the eight electrical posts beside the sample stage[8]. These posts can be seen in Figure 3.11 along with a schematic diagram of an alternative method for measuring samples using silver paint. In this case silver paint in the corners of the sample is connected to the posts directly using copper wires. This method using rigid clips has advantages over alternatives such as silver paint as the contacts are far less likely to fail when the system is cooled; the silver paint has a tendency to crack/break when cooled causing the contacts to fail, whereas the mechanical clips do not suffer from this problem. The tips of the copper clips are coated with indium metal, which is malleable and can be

[6]These clips are screwed down using Teflon screws, which are both electrically insulating and vacuum compatible.

[7]For samples with electrically conductive substrates a thin piece of paper is also inserted under the substrate in order to electrically insulate it from the copper block.

[8]These posts are electrically isolated using electrically insulating spacers. They are connected to an electrical feed-through via thin wires running along the length of the cold finger. The wires are wrapped around the cold finger several times to thermally anchor them.

stoutly pushed onto the surface of the sample[9]. A two or four terminal resistance measurement can then be performed using these contacts. The copper block and clips is shown schematically in Figure 3.4 for both a magnetic tunnel junction and bulk film. In the case of a four-terminal resistance measurement the van der Pauw geometry is used, for which contacts are placed in the four corners of the sample. The measured resistance is then converted into a resistivity using Equation 3.1.

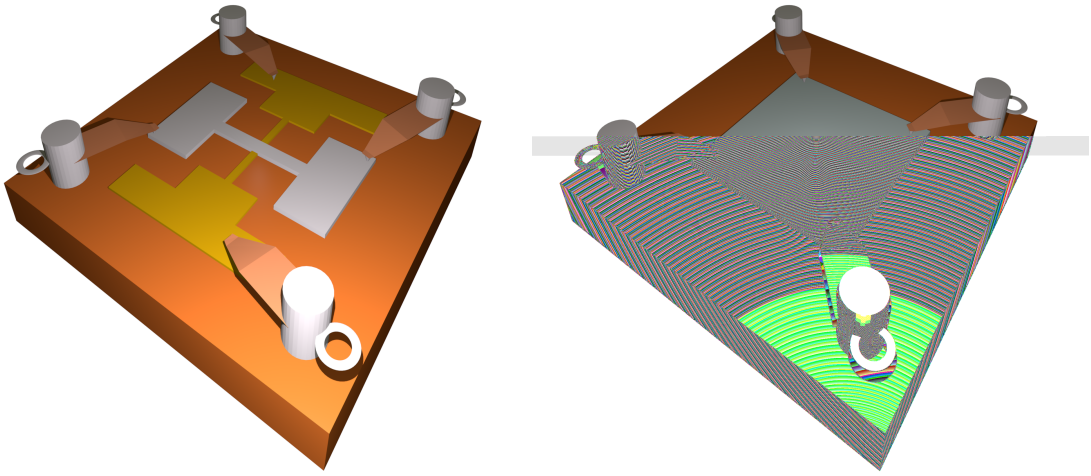

Figure 3.4 – Diagram of the copper block and clips used to perform current-voltage and temperature dependent resistivity measurements in the closed-cycle cryostat. Left: Depiction of measurement of a cross-contact magnetic tunnel junction. Right: Depiction of measurement of a bulk sample in the van der Pauw geometry.

The closed-cycle cryostat is automated using a LabVIEW program which controls the temperature using a Lakeshore 340 temperature controller, which monitors two silicon diode thermometers inside the cryostat. When in operation the refrigerator unit cools the system down to ∼4 K, and a resistive heater connected to the temperature controller is used to obtain sample temperatures between 4 K and room temperature. LabVIEW also controls the current source (Keithley 224)

[9] A further step which can be employed to further reduce the contact resistance is to apply a small amount of silver paint to the indium contact-sample interface. This is then wicked into the area around the join and increases the contact area.

and monitors the voltmeter (Keithley 182) used for electrical transport measurements. Electrical connections are made through a high-vacuum feed-through into the cryostat, and the sample is connected via wires soldered to posts inside the cryostat. A schematic diagram of the electronic apparatus is shown in Figure 3.5. The LabVIEW program records the sample voltage as a function of current in both the forward and reverse directions to negate spurious thermoelectric voltages. The current and temperature are also recorded throughout the measurement.[10]. The measurement routine is defined by a sequence file which is loaded at the beginning of each measurement. Some examples of these sequence files can be found in Appendix A.

During this PhD, LabVIEW code has been rewritten to measure the current using an ammeter in series with the current source. Prior to this it was frequently observed that the sample resistance would overload the internal voltage limit of the current source. In this case the current source then reverts to a voltage-limited measurement mode where the current is undetermined although LabVIEW continues logging data. This can result in erroneous data as no error message is generated in the data file. By installing an ammeter in series the real current is measured; if the real and desired currents do not match a column in the datafile logs the error and the real current can then be used to calculate the real resistance.

3.3.3 Current-Voltage Characteristics

In the closed-cycle cryostat there is also the facility to measure current-voltage (IV) characteristics of samples as a function of temperature. During this PhD two different ways to do this using different LabVIEW programs have been developed.

Most commonly the LabVIEW program mentioned in Section 3.3.1 above is used with a modified sequence. In these sequences the sample is held at a given temperature and each subsequent line of the routine instructs LabVIEW to iteratively perform measurements while varying the current. Each of these measure-

[10]The temperature is recorded using two different thermometers at different distances from the sample. The difference between these two readings gives a rough measure of the level of thermal gradients present in the system.

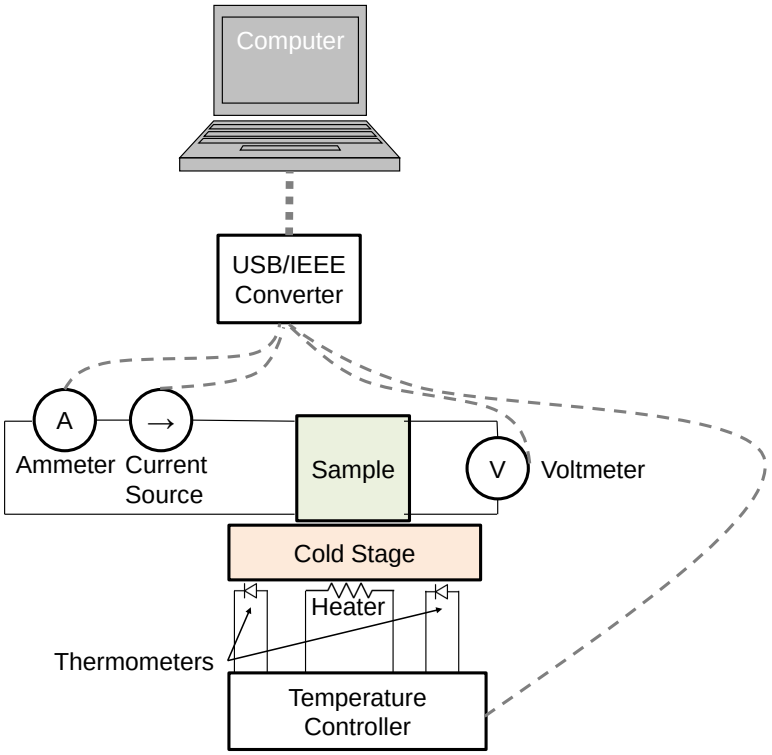

Figure 3.5 – Schematic diagram of the resistivity measurement apparatus.

ments generates a new data file so it is necessary to concatenate these files to obtain the full I-V curves. An example of one of these sequences can be found in Appendix A along with the commands used to concatenate the data files.

The other method uses a new LabVIEW program developed during this project. This program scans the current and measures the voltage continuously and outputs all the data in a single file. In this case the temperature is controlled by hand and the operator must be present in order to scan to a different temperature.

The first method is ideal for performing long measurements overnight or over multiple days while the second measurement is better for performing quick measurements with the operator present, such as to check whether contacts are Ohmic or not.

3.3.4 Magnetoresistance Measurements

Magnetoresistance is the change in sample resistance in response to an applied magnetic field.

Magnetoresistance measurements are performed using a Quantum Design Physical Property Measurement System (PPMS)[11]. The PPMS contains a sample stage which can be rotated within a superconducting magnet capable of generating magnetic fields up to 8 T. Electrical transport measurements can be performed in these fields between room temperature and 2 K. For electrical resistivity measurements samples are mounted onto a sample holder known as a "puck". The puck has two independent measurement channels each consisting of four gold pads to which the sample can be connected[12]. These gold pads are connected to the sample by means of copper wires and silver paint. The sample is thermally and mechanically anchored to the puck using 7031 cryogenic varnish. In principle both channels can be connected to the sample to perform two measurements simultaneously (such as Hall effect and magnetoresistance), however for a single set of magnetoresistance measurements, only one channel need be connected.

Metal pins on the puck interface with the PPMS to bridge the electrical connections while permitting sample rotation. The PPMS has a vacuum seal at the top so that the sample space may be evacuated of air once the puck has been installed. The measurement is then conducted by way of a sequence programmed into the PPMS. For magnetoresistance measurements this sequence normally consists of the following steps:

1. The temperature and magnetic field are stabilised at 300 K and 0 T, respectively.

2. The sample resistance is measured as a function of temperature while cooling to 3.5 K[13].

[11] Magnetoresistance measurements up to 1 T can also be performed using the liquid helium bath cryostat along with the attached electromagnet. See Appendix B for more details.

[12] The four pads are comprised of two voltage and two current connections.

[13] The PPMS can be cooled to liquid helium temperatures by way of liquid helium introduced through a needle valve.

3. The resistance is measured as a function of magnetic field at a low temperature (e.g. 5 K) with the field applied perpendicular to the substrate plane (field out of plane)[14]. This field orientation is denoted 0 degrees.

4. The resistance is measured as a function of magnetic field at the same temperature at 90 degrees. Here the field is in plane with the substrate.

5. Steps 3 and 4 are repeated at a selection of higher temperatures.

6. If time permits scans of the resistance as a function of temperature in various applied magnetic fields can be conducted.

The magnetoresistance is defined as the change in resistance under and applied magnetic field divided by the resistance at zero field[15]:

$$\mathrm{MR} = \frac{R(H) - R(0)}{R(0)}. \tag{3.2}$$

IV curves can also be performed using the PPMS however the measurement mode (AC transport) best suited to I-V curves has a low internal impedance which makes it unsuitable for most of the magnetic tunnel junctions (MTJs) studied in this project.

3.3.5 Hall-Effect Measurements

A current flowing through a (finite) slab of material in the presence of a magnetic field is influenced by what is known as the Hall effect. The magnetic field results in a Lorentz force ($-\frac{e\vec{v}}{c} \times \vec{H}$) which deflects electrons to one side of the slab and holes to the other by virtue of the sign of their charge. This results in a transverse electric field (as shown in Figure 3.6) from which the Hall coefficient is defined as

$$R_H = \frac{E_y}{j_x H},$$

[14]Often these scans as a function of applied magnetic field are broken up into separate regimes whereby the field is swept more slowly at low field than at high field. This is done in order to ensure that a sufficient number of data points are obtained at low fields. To observe switching in tunnel junctions the field is swept up to 8 T, down to −8 T, and then up again to 1 T.

[15]This reference state is typically taken at 0 T, although sometimes a high field value is used in the literature (often to give a larger % change).

where E_y is the transverse y (Hall) electric field, j_x is the current density in the x direction and H is the magnetic field.

From the Drude model it is possible to derive (see Ref. [59] pg. 11) the equation

$$\frac{d\vec{p}(t)}{dt} = -\frac{\vec{p}(t)}{\tau} + \vec{f}. \tag{3.3}$$

Here $\vec{p}$ is the momentum per electron (or hole), τ is the relaxation time and $\vec{f}(t)$ is the external force acting upon the electrons.

By inserting the Lorentz force into Eq. 3.3 and noticing that in the steady state this will be time independent and $j_y = 0$ [59], it is found that

$$R_H = -\frac{1}{nec}.$$

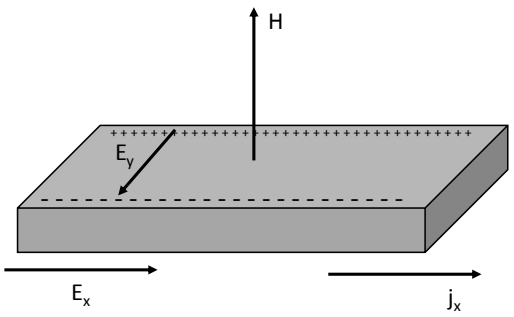

Figure 3.6 – Schematic illustration of the Hall effect. Here E_x is the x (bias) electric field.

Hall effect measurements can be performed at room temperature by measuring R_H in different applied fields. For low temperature Hall effect measurements the PPMS is employed. The sample must be connected differently to resistance measurements in order to measure the perpendicular voltage. The PPMS has two measurement channels, so it is possible to perform magnetoresistance and Hall effect measurements simultaneously. The measurement sequences for Hall effect are run in much the same way as for magnetoresistance measurements. Typically

the Hall resistance is measured by performing measurements at both 0 and 180 degrees and taking the difference[16]. Due to the measurement geometry used there are often magnetoresistive components to the measured resistance in each direction. These are removed by measuring at both 0 and 180 degrees and taking the difference.

3.3.6 Magnetometry

Magnetometry measurements are performed using a Quantum Design Magnetic Property Measurement System, more commonly referred to by its method of operation as the superconducting quantum interference device (SQUID). The SQUID utilises two parallel Josephson junctions connected into a superconducting loop. In the presence of a magnetic field the current flowing in this loop is perturbed and the measured voltage begins to oscillate (each oscillation corresponds to one magnetic flux quanta). Counting the oscillations (done by the instrument) allows the change in magnetic flux through the loop to be measured.

For SQUID measurements, samples are grown on silicon alongside those used in patterned devices, and the silicon is then cut into smaller pieces for different measurements such as scanning electron microscopy. The size of samples to be used in the SQUID is constrained by the size of the sample holder to $\sim$3 mm wide and approximately twice as long. The cut piece is then mounted into a plastic straw using a second straw to keep the sample securely in place [17]. The location of the sample within the straw is important for the measurement as once installed a centring procedure must be undertaken in order to perform precise measurements.

[16] Care must be taken when measuring samples which exhibit large hysteresis.

[17] When performing measurements with the SQUID, care must be taken to remove potential sources of magnetic contamination which may interfere with the measurement. If possible, plastic or brass tweezers should be used as steel tweezers may transfer magnetic impurities to the sample. This is even more important to consider when attempting to measure samples with a small magnetic moment such as SmN. Given that the film thickness is just some tens or hundreds of nanometres even a small amount of contamination can easily mask the signal of the sample. Other sources of potential erroneous signals to consider include diamagnetic or paramagnetic contributions from the substrate or capping layer.

A centring scan is performed until a good fit of the sample location (automated by the software) is obtained. This ensures that as the sample is moved up and down during the magnetisation measurement the scan is correctly centred and extends over the correct range. Once the centring process is complete, the measurement can be initialised and follows a sequence programmed by the user. The measurement is conducted by moving the sample up and down in close proximity to the SQUID detector. The magnetic moment of the sample is then measured by way of counting the magnetic flux.

In this thesis all measurements have been performed in the reciprocating sample option (RSO) configuration. Each measurement sequence generally begins first with zero field cooled (ZFC), followed by a field cooled (FC) scans of the temperature dependent magnetisation. For ZFC measurements the sample is cooled in zero field. Magnetic domains form as the sample is cooled, and these are measured on warming under a small applied magnetic field. For FC measurements the sample is cooled in the presence of a small magnetic field. This applied field tends to align the magnetic domains that form as the sample is cooled. The difference between ZFC and FC curves can be used to obtain information about magnetic ordering such as the Curie temperature or the coercivity [72]. It is generally easier however to extract the coercive field from the field loops (MH loops) which are performed at fixed temperatures after the ZFC/FC scans.

3.3.7 X-Ray Diffraction

X-ray diffraction is an analytical technique used to assay the quality of thin films. It can allow determination of the crystalline quality and the composition (to some extent) of thin films.

XRD is performed in-house using a PANalytical X'Pert x-ray diffractometer. The substrates are mounted horizontally[18], and a scan of the reflected intensity as

[18]It is important to ensure that samples are mounted as flat as possible. Flatness can be estimated by observing the position of the substrate reference peak. While some degree of correction for angle offset can be made while analysing data, it is generally advisable to minimise this. To this end, the samples are mounted either onto a glass slide attached to the flat stage in

a function of the incident angle is obtained using the $\theta - 2\theta$ or x-ray reflectivity geometries. The diffracted angle, 2θ, is the angle between incident x-rays and the detector. For these measurements the sample is kept flat and the source and detector symmetrically rotated about the sample.

The XRD peak positions depend on the crystal structure and lattice constant, and the crystallite size can be determined from the location and widths of the peaks using the Scherrer equation [73]:

$$\tau = \frac{K\lambda}{\beta \cos\theta}$$

where τ is the size of the crystallites, K is the shape factor (K≈0.9 for spherical domains), λ is the x-ray wavelength (1.54Å), β is the FWHM spread of the peak in 2θ space (in radians) and θ is the Bragg angle.

By matching the locations of the peaks to tabulated values, the crystallographic orientation of the crystallites can be found and, by using the Bragg formula [74], the lattice constant can be ascertained:

$$d = \frac{n\lambda}{2\sin\theta},$$

with

$$a = d\sqrt{h^2 + k^2 + l^2},$$

where h, k, l are the Miller indices.

Another type of measurement known as a rocking curve measures detected intensity as a function of ω, the angle between the source and the sample surface[19]. For this measurement the detector is held fixed and the sample is tilted using a motorised stage. The width of the rocking curve peak measured yields information about the crystalline quality and defects present.

A third type of measurement, known as x-ray reflectivity (XRR), relies on the interference fringes produced when x-rays are reflected from the film surface at

the diffractometer or (for small samples) onto an adjustable sample holder.

[19]Rocking curve measurements in this thesis were performed off-site using a system with a goniometer.

grazing incidence.[20] Fitting of the x-ray reflectivity fringes produced in multilayer structures allows for the thickness and roughness of layers to be assessed.

3.3.8 Electron and Optical Microscopy

Both optical and electron microscopy are used to assay the properties of films and devices. Within the scope of this project, optical microscopy was useful for examining patterned features. Scanning electron microscopy (SEM) with a JEOL 6500F scanning electron microscope was used in order to examine the thickness of crystalline layers. The wavelength of a high energy electron is significantly lower than that of a photon so images can be acquired at a much higher resolution than using an optical microscope. This allows features on the order of nanometres to be resolved. The sample preparation and measurement procedure is as follows: The samples are first cleaved using a diamond scriber in order to expose a fresh surface to be studied in the cross-section geometry. The substrates are mounted to a metal stub using conductive carbon tape which helps to minimise charging [21]. The carbon tape must be sufficiently outgassed before the samples can be introduced into the SEM, for this purpose our sample storage desiccator is used to desiccate the samples overnight prior to examining them with the SEM.

After introducing the samples into the load lock, and finally the analysis chamber of the SEM, the gun valve can be opened and the samples exposed to the electron beam. At this point it is necessary to align the electron beam with the desired beam current and voltage.

[20] For x-rays most materials have a refractive index less than 1, this results in an effect known as total external reflection which is exploited by XRR measurements.

[21] The ideal substrate to use for SEM samples is conductive silicon. This mitigates problems caused by electron charging. If there are no low-resistance pathways for the electrons to flow to ground, charge may build up on the surface creating a local electric field disturbance which steers incident electrons away from the specimen and smears the acquired image. If an insulating substrate is used (i.e. if conductive silicon is not available for growth reasons) the carbon tape may be folded over onto the surface of the film to aid in electrical contact. Conductive layers such as platinum or carbon may be coated onto the sample surface to enhance conductivity, however this also potentially changes the surface topography.

The SEM is capable of acquiring images in the secondary electron imaging (SEI), energy-dispersive x-ray spectroscopy (EDS) and backscatter electron measurement modes, these are described in Appendix C. SEI is most commonly used and gives information about the surface topography. EDS is used to assay the elements present in the sample by means of emitted x-rays, however this has a limited sensitivity and resolution and is most useful for qualitative analysis rather than quantitative measurements. Backscatter measurements are sensitive to the mass of the material present as well as the topography, which is useful to obtain contrast between layers of different atomic mass.

3.4 Electrical Contact Deposition

Electrical contacts are important for measuring the properties of both devices and bulk samples. Ohmic contacts are desirable as these permit the sample/device, rather than spurious contact resistance effects, to be measured. It is also important to be able to produce reliable contacts which will survive at low temperatures. Making electrical contact to the rare earth nitrides is challenged by the fact that they oxidise readily. This makes it impossible to deposit the contacts directly onto the REN after the sample has been removed from the growth chamber.

In this project, various methods for electrical contact deposition were investigated. Electrical contacts for transport studies may be deposited before substrates are loaded into the chamber for rare-earth nitride growth. These are referred to as predeposited contacts. In this case the rare-earth nitride sample is later grown on top of these predeposited contacts. One advantage of predeposited contacts is that metals can be used that are not available inside the rare-earth nitride growth chamber. The sample holder in the evaporator for contact deposition is also significantly larger than the sample holder in the rare-earth nitride growth chamber, meaning that many substrates with predeposited contacts can be prepared simultaneously. Another option for contact deposition involves the growth of contacts on top of the rare-earth nitride film inside the growth chamber. This is referred to as *in-situ* contact deposition and has the advantage of depositing the contacts directly onto the rare-earth nitride layer without exposing the surface to air.

3.4.1 Predeposited Contact Deposition

Predeposited contacts are prepared using an Angstrom Engineering evaporator containing two resistively heated thermal sources, and an electron-gun with a carousel containing several different pockets. The contact geometry may be defined either using photolithography (see Section 3.2) or shadow lithography. In the case of shadow lithography samples are cut into 1 cm^2 pieces using a diamond scriber and affixed to a shadow mask using kapton (polyimide) tape. Holes in the shadow mask leave areas of the substrate exposed for deposition. Kapton tape is then used

to attach the mask (or samples defined by photolithography) to the sample holder, which is loaded into the evaporator. Once the desired metals are installed using an appropriate thermal evaporation source[22] the door is sealed and the evaporator is pumped down. Several hours later, once the pressure is $\sim 2 \times 10^{-6}$ mbar, the contacts can be deposited. A shutter is opened once the sources have been heated and a stable deposition rate is obtained using a pre-programmed deposition controller[23]. The rotating sample holder is then exposed to the metal vapour. The process of this predeposited contact deposition is illustrated schematically in Figure 3.7. Typically Cr/Au contacts are used, where in this project ∼3 nm of Cr is deposited to aid in adhesion followed by $\sim 50 - 100$ nm of gold.

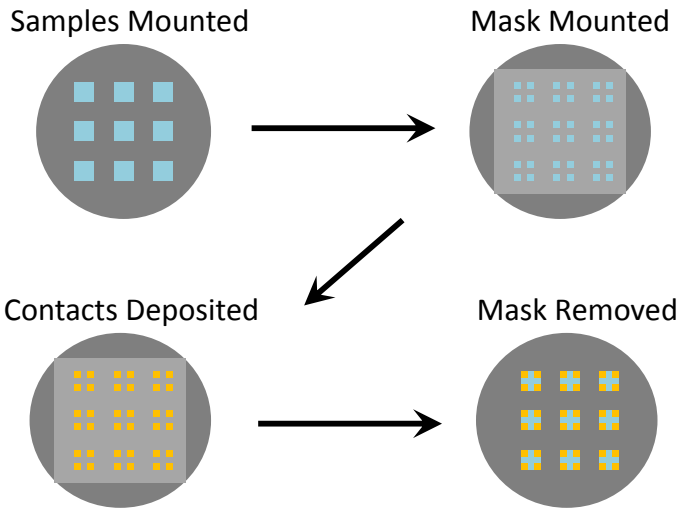

Figure 3.7 – Schematic diagram of the predeposited contact deposition process.

[22]This may be a resistively heated boat, crucible or metal-coated rod.

[23]The deposition controller accounts for the density and Z-factor of the metals used so that a more accurate measurement of the deposition rate can be extracted from the quartz crystal oscillators inside the chamber. The Z-factor is used to match the acoustic properties of the material to the quartz substrate.

3.4.2 *In-Situ* Contact Deposition

Contacts can be deposited *in-situ* using either the electron gun (for rare-earth metallic contacts) or by using an effusion cell (for Al contacts). In principle almost any material could be loaded into the e-gun however due to constraints on the number of sources, and the time taken to re-load the system, it is generally only filled with rare-earth metals and gallium.

The evaporated metal is ejected from the e-gun and is allowed to fall onto the substrate in a pattern described by a mask developed during this project. Generally for horizontal transport studies the van der Pauw geometry is used, and this mask can be seen in Figure 3.8. The mask holder is spring-loaded so that it can be brought into intimate contact with the film surface without risking damage to the delicate components inside the UHV system. The materials used have been selected to be UHV compatible and the base of the mask is designed in order to interface with the pre-existing sample transfer arm available within the chamber; this transfer arm can be moved linearly, by doing so each of the 3 growth windows in the mask can be used to grow the film, the contacts, and the capping layer, respectively[24]. The capping layer growth window is rotated by 45 degrees in order to leave a small portion of the contacts uncapped for making electrical contact.

A flowchart of this horizontal contact growth procedure is depicted in Figure 3.9.

In order to prepare devices in the vertical transport orientation, a cross-contact geometry was also employed using a similar mask based process which is shown schematically in Figure 3.10. Here the lower contact strip was predeposited, with the sample and top contact deposited into a perpendicular strip using a shadow mask.

The above techniques can be used to prepare epitaxial films. For polycrystalline films a mask is not required inside the vacuum system and the film growth is defined

[24]When designing this mask holder care was taken to ensure that the mask itself is a modular component. The mask attachment can be removed and interchanged with other film/mask/capping layer geometries without needing an entire mask holder assembly to be re-machined each time.

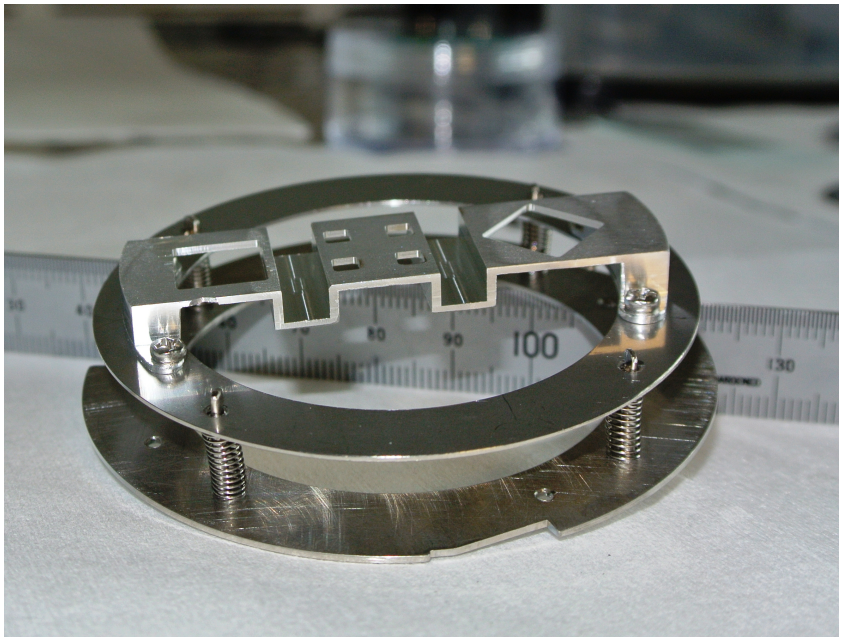

Figure 3.8 – Photograph of the mask used for contact deposition *in-situ* on top of the film.

by photolithography and/or by using predeposited contacts. Photolithography has a higher resolution than shadow masking, albeit at the cost of not being able to grow at high temperatures. When vertical transport studies are to be undertaken, the growth procedure differs slightly. A substrate must be used with a pre-patterned base contact geometry to form the lower contact. The film is then grown on top of this bottom contact before the top contact is grown. In this situation the top contact also acts as the capping layer. This process is shown schematically in Figure 3.10.

3.4.3 Silver Paint vs. Predeposited Contacts

Prior to fabricating REN devices it is necessary to understand the conductive nature of the electrical contacts by which measurements are performed. There are two common established techniques for performing resistivity measurements of the RENs in the van der Pauw geometry. In one case, predeposited contacts

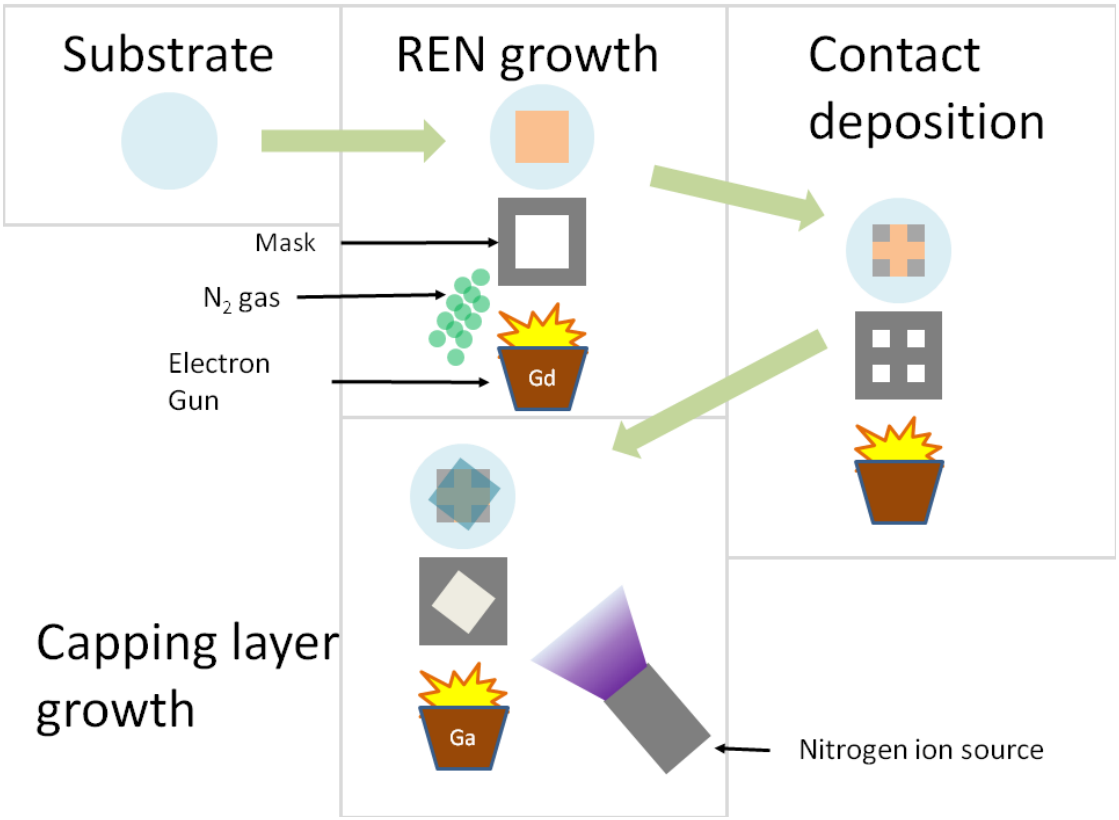

Figure 3.9 – Schematic flowchart of the method used for contact deposition *in-situ* on top of the film for van der Pauw measurements (horizontal transport).

are patterned using shadow lithography and then the film is deposited onto these as described in Section 3.4.1. In the second case, silver paint is applied to the top surface of the film and wires are attached to posts inside the cryostat, as represented schematically in Figure 3.11. While the effect of the contact resistance itself is mitigated by use of a four-terminal geometry these methods both have disadvantages; The former technique cannot readily be applied to epitaxial samples (which are grown at high temperatures) unless refractory metals are used. In this case unless the metal used is epitaxially compatible with the REN layer the sample will be polycrystalline above the contact. The silver paint technique can be applied retrospectively to epitaxial samples, however there is a propensity for contacts to

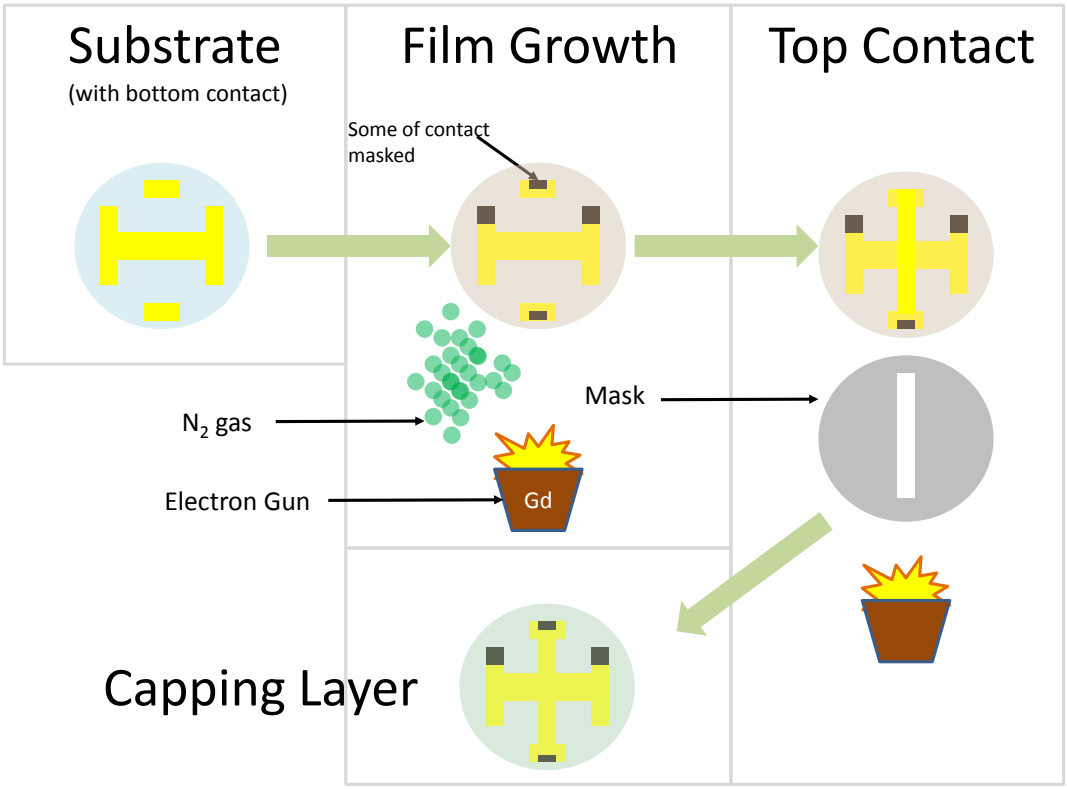

Figure 3.10 – Schematic flowchart of the shadow lithography method used for contact deposition *in-situ* on top of the film for vertical transport studies.

fail using this method. This is partly due to the fact that current must still pass through the insulating capping layer. Contact failure predominantly happens as the sample is cooled, where contacts functioning correctly at room temperature may fail during cooling. This can occur either because of a mechanical failure, or due to an increase in the contact resistance. The silver paint technique is also susceptible to geometrical asymmetries which complicate the data analysis.

To investigate the properties of silver paint contacts, two-terminal current-voltage characteristics were performed. Figure 3.12 (left) reveals non-linearity at low-bias suggesting that the contacts are non-Ohmic in nature. Because silver paint is being used to contact directly to the insulating capping layer, there will

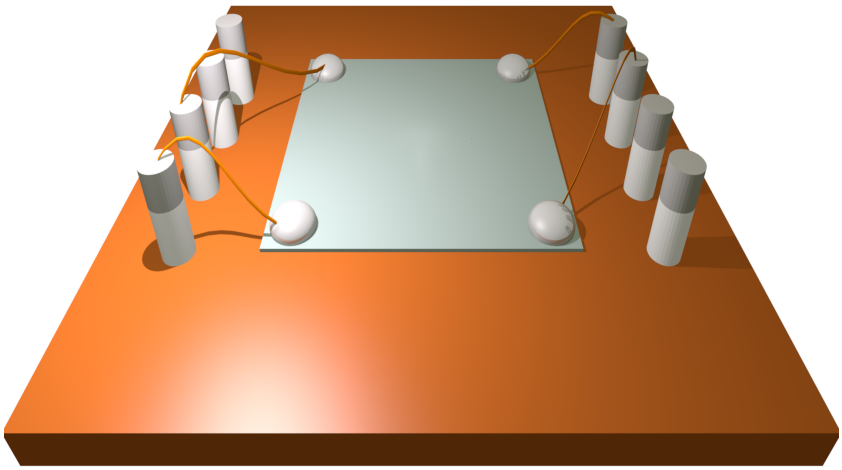

Figure 3.11 – Schematic diagram of a resistivity measurement performed using silver paint contacts.

be Schottky barriers forming at the interface. For comparison, current-voltage characteristics were also performed on a sample with predeposited gold contacts and are displayed in Figure 3.12 (right). In this case the contacts are Ohmic, making them desirable for use in electronic devices where reliable contact to the active layers within the device is required[25].

3.4.4 *In-situ* Contact Testing

Samples were grown with the contacts deposited *in-situ* using the van der Pauw shadow mask in the manner shown in Figure 3.8. Preliminary testing revealed that it is possible to make contact to the rare-earth nitrides in this way. Figure 3.13

[25]The study of Ohmic contacts was broadened and continued by Felicia Ullstad, and appears in a paper examining the current-voltage characteristics of a number of different metals [75].

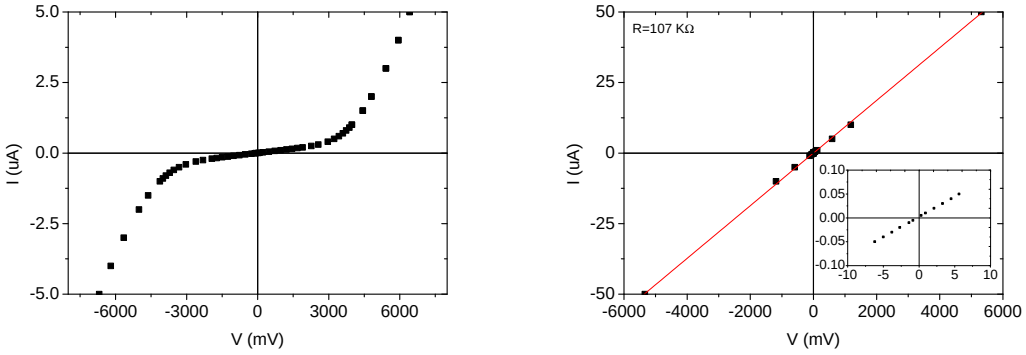

Figure 3.12 – Current voltage characteristics of a sample measured using silver paint contacts (left) and predeposited Au contacts (right) at 5 K. The inset to the right hand plot shows the linearity of the Au contacts at low voltage.

shows the resistivity of a GdN sample grown using this mask with contacts made from graduated GdN where the nitrogen flow into the chamber was stopped and the contacts allowed to evolve into pure gadolinium. The exposed GdN layer was then capped with GaN after contacts were deposited. This sample shows a clear peak in resistance at 50 K associated with the onset of exchange splitting within the GdN layer, verifying that it is the GdN resistance being measured. However, it was found that correct alignment of the mask at each step was very challenging, meaning that predeposited contacts should be used wherever possible. This method of depositing *in-situ* contacts is best suited to samples that require this technique, such as epitaxial films.

Temperature dependent resistance data for a bulk GdN sample patterned using shadow lithography in the vertical transport orientation is included as Figure 3.14. This sample was prepared as described in Figure 3.10 with a mask attached to the transfer arm of the vacuum system. This sample is 100 nm of GdN on a gold contact with an Al/Gd top contact[26]. The shape of the temperature dependent

[26]The aluminium contact/capping layer oxidised after several hours of the sample being exposed to air, suggesting that aluminium is not suitable as a contact material in thin films such as these.

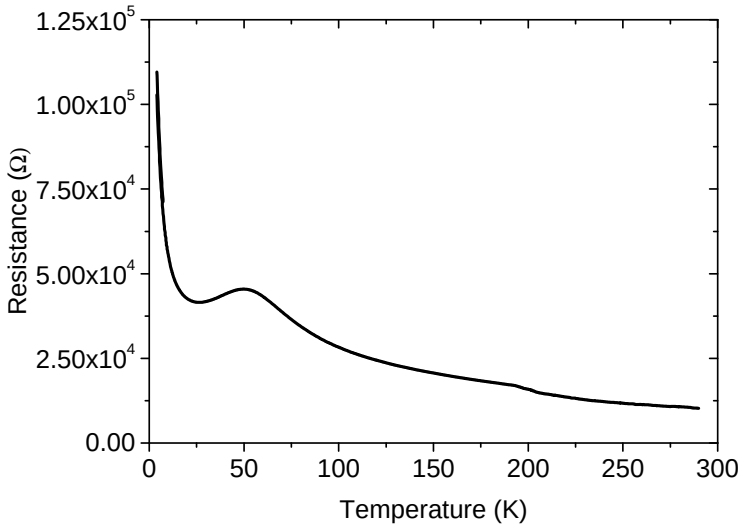

Figure 3.13 – Temperature dependent resistance for a sample grown with contacts deposited *in-situ*.

resistance curve is much more metallic than bulk GdN and the reasons for this shape, due to a contact resistance component, are discussed in Section 3.5 for Gd/GdN/Au junctions. It was found to be difficult to align these samples in order to prepare cross-contact samples. For this reason, and to improve the resolution, it was decided instead to prepare photolithographically defined samples. If epitaxial tunnel junctions are to be produced in future in a bottom-up method, this *in-situ* technique for preparing junctions should be re-examined. It offers the possibility of producing tunnel junctions without using photoresist which will not survive the high temperatures required for epitaxial growth.

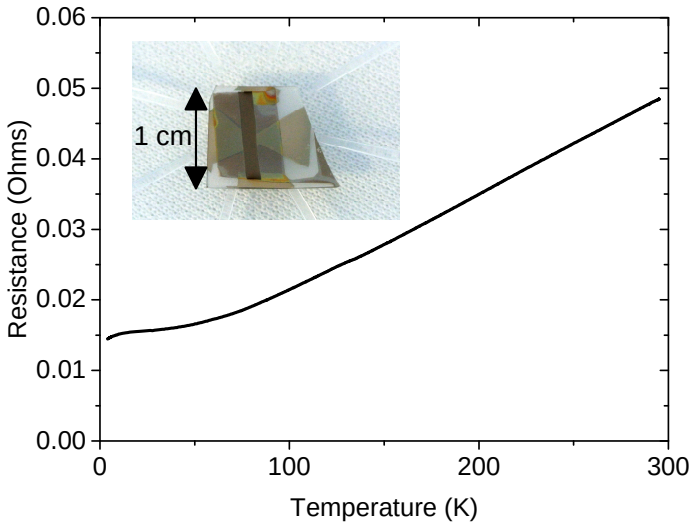

Figure 3.14 – Temperature dependent resistance of a sample grown using shadow lithography *in-situ*. Inset: Photograph of the sample.

3.5 Junction Contact Resistance Effects

Photolithography was used to produce samples in a similar cross-contact geometry to Section 3.4.4. Prior to fabricating multilayer devices, samples were produced with bulk GdN control layers to be measured in the vertical transport geometry. A narrow (100 µm) gold contact strip was deposited onto a sapphire substrate and patterned using photolithography followed by a metal lift-off process as described in Section 3.2. A 200 µm wide channel was then fabricated by photolithography orthogonal to the gold strip. The GdN was then deposited by evaporating Gd metal from an electron gun in the presence of nitrogen gas, followed by a top layer of ∼40 nm gadolinium metal that acts as a top contact and also as a capping layer to prevent oxidation of the GdN. A photograph of this cross-contact device geometry is included as Figure 3.16. This geometry was chosen as a four-terminal measurement mitigates the resistance of the leads, measuring only the resistance at the junction. In order to further minimise the effect of the lead resistances[27] a barbell shape has been employed. This means both that the leads are as wide as possible for as long as possible, and that there is a sufficiently large metal pad to make contact and measure the device easily.

Figure 3.15 (left) displays temperature dependent resistance data from a sample patterned into a cross-contact geometry with a GdN layer between Au and Gd layers. For comparison, the temperature dependent resistance of Gd metal at low temperatures (< 120 K) is included in Figure 3.15 (right). The data in Fig. 3.15 (left) is qualitatively different from both the temperature dependent resistance of GdN layers (see Fig. 2.4) and that of the Gd layer. First of all note that the resistance of the vertical transport sample changes much more as a function of temperature than does the metallic Gd layer, and there are also some subtle differences to the shape at low temperature. It is likely that there is a component of the resistance from the Gd contact which dominates the vertical transport data at high temperatures while the GdN resistivity begins to contribute appreciably to

[27] Minimising the 2-terminal resistance is important as the current source used for transport studies has an internal voltage limit. The 2-terminal voltage, and hence resistance, limits the maximum current that can be applied.

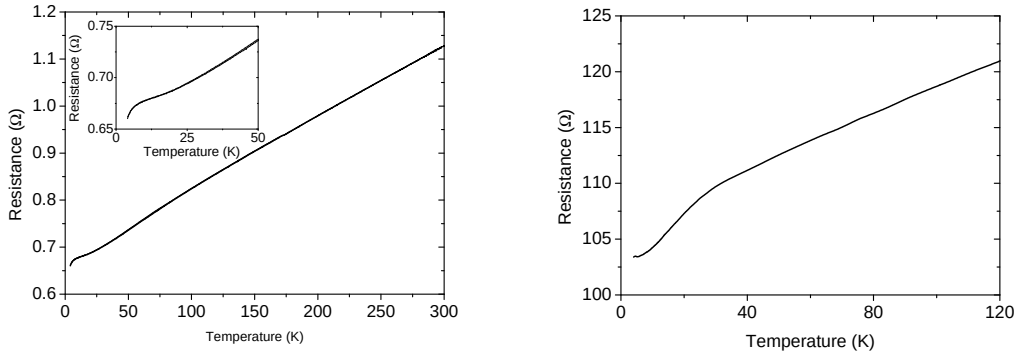

Figure 3.15 – Temperature dependent resistivity data for a Au/GdN/Gd sample measured in the vertical transport geometry (left) and Gd layer (right).

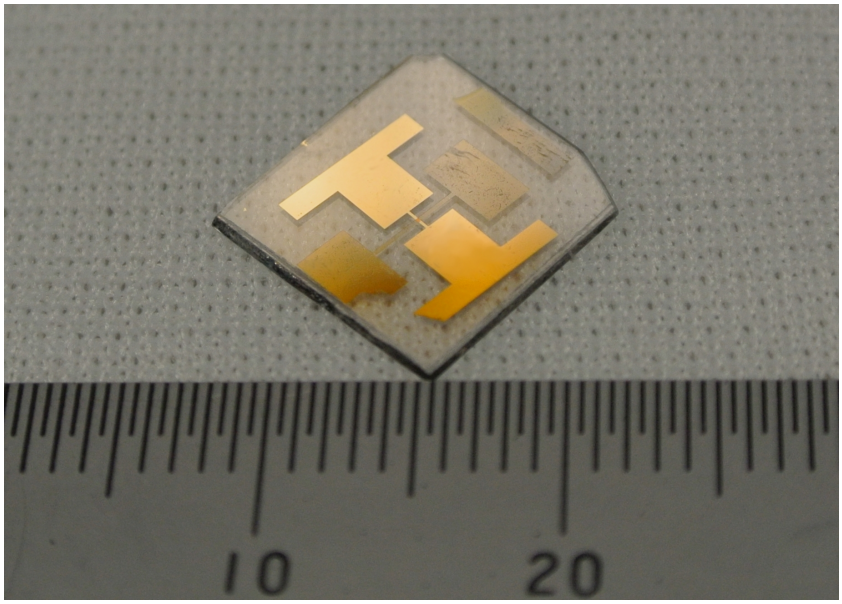

Figure 3.16 – Photograph of a sample prepared in the cross-contact geometry using photolithography.

the low temperature resistance. Thus, resistivity measurements of bulk GdN layers using this cross-contact geometry are compromised by spurious contributions from the electrical contact layers. The origin of these contributions will now be examined in more detail.

The four-terminal measurement geometry mitigates the effects of the leads. However, diagonal resistance pathways across the junction can still contribute to the measured resistance (this is illustrated in Figure 3.17). The resistance pathways will change as a function of temperature due to the competition between the metallic resistance (which decreases with decreasing temperature) and the semiconducting GdN (which increases with decreasing temperature)[28].

The relative size of these two contributions can be assessed approximately for the GdN devices. For transport along a 100 nm thick Gd layer with a resistivity of $\sim$100 µΩ cm [77], and with

$$R = \rho\frac{l}{A},$$

l =100 µm and A =100 µm×100 nm[29] then R_{Gd}=10 Ω. The resistance measured through a 100 nm thick GdN layer (of area 100 µm×100 µm) can be calculated in a similar way. For a resistivity of 1 Ω cm at room temperature R_{GdN} =0.1 Ω so the measurement is dominated by the Gd contact. The resistivity only has to increase to 10 Ω cm at low temperatures for the GdN to contribute 10% of the total resistance. While the numbers here are very approximate, it is easy to see how the relative contributions of the Gd and the GdN to the total resistivity may change as a function of temperature. This can be used to explain the data in Fig. 3.15, however it also means that in order to measure the vertical transport of GdN alone these devices must be: made much smaller, have much more conductive contacts, or the resistance of the sample layer must be engineered in order to dominate. A schematic diagram included as Figure 3.17 illustrates how the current might flow in one of these junctions where the resistance of the top contacts is comparable to the resistance down vertically through the layers. In this case there is both a horizontal component from the contacts along with the vertical component which is trying to be measured. A more detailed treatment of the voltage profile in these cross-contact junctions is included in Appendix D.

[28]Pomeroy and Grube solve this problem using finite element modelling in the case where the series resistance of the contacts is larger than the device resistance [76]. They show that it is possible to correct for the anomalous resistance contributions due to these contact effects.

[29]This assumes that roughly half of the Gd contact contributes and that the Au contribution is negligible.

In the highly resistive tunnel junction devices presented in this thesis these erroneous resistance contributions are not expected to contribute due to the large resistance introduced by the barrier. However, for devices with a low (but non-negligible) vertical resistance which increases with decreasing temperature, it is expected that the sign of the measured voltage will reverse as the sample is cooled. Fig. 3.17 shows how these devices are connected and how such a sign inversion can occur. It is apparent that in this geometry when the sample resistance dominates the apparent voltage is positive while when the contact resistance dominates the apparent voltage is negative.

With these geometrical considerations in mind, the data in Figure 3.15 can be qualitatively understood where the positive voltage due to the contacts is combined with a negative voltage due to the sample[30]. GdN has a peak at 50 K where exchange splitting sets in. This voltage contribution (vertical) is in opposition to the contact resistance contribution and results in the shoulder around 50 K (as seen in the Gd resistance data) being reduced. Similarly, GdN has a large upturn in resistivity at low temperatures, which explains the downturn in resistance below 10 K in Fig. 3.15.

[30]Please note that this sample was connected with the voltage leads in the opposite polarity with respect to Fig. 3.17 in order to yield positive resistance values.

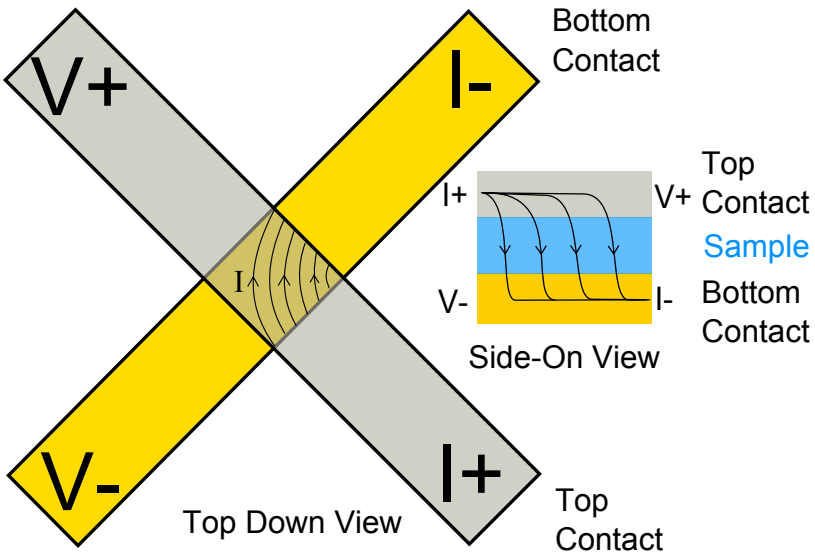

Figure 3.17 – Schematic diagram of the cross-contact measurement geometry with the diagonal resistance pathways highlighted. Note that the current distribution pattern will differ depending on the relative resistivities of the layers.

Chapter 4

Tunnel Junctions with GdN Electrodes

4.1 Motivation

As outlined in Chapter 1, there are many reasons motivating both fundamental and applied research into new types of solid state devices. In this chapter, results from magnetic tunnel junctions with gadolinium nitride as the electrodes will be presented and discussed. In contrast to conventional ferromagnetic metals commonly used in MTJs, electrodes based on ferromagnetic semiconductors are especially interesting because of the potential for 100% spin polarisation and also because the charge density can be tuned. By studying its device integration there is also potential for understanding more about the fundamental properties of GdN.

4.2 Introduction

4.2.1 Magnetic Tunnel Junctions

A magnetic tunnel junction is comprised of two ferromagnetic layers separated by a thin insulating layer through which current must tunnel to pass between the two ferromagnetic materials . Generally when the magnetisation of the two

layers is aligned the tunnel resistance is low and, conversely, when anti-aligned the resistance is high. By exploiting this resistance contrast the tunnel junction may be used as a magnetically actuated switch. A schematic diagram of the energy bands of the magnetic layers in both resistance states is shown in Figure 4.1 along with a diagram of the structure of such a device. In this figure the two resistance states are shown. In the case of parallel alignment the two majority spin orientations are aligned and the resistance is low, while in the high resistance case the spin polarisations are anti-aligned. Note that it is actually the alignment of the majority spin polarisation which controls the device resistance rather than the magnetisation. In conventional systems exploiting transition metal based magnets, the spin aligns with the magnetisation so the two can be used interchangeably. In the case of rare-earth systems where the orbital contributions come into play it will be seen, in the case of SmN, that this needn't be true.

Magnetic tunnel junctions and tunnel magnetoresistance have produced major technological impacts, forming the basis for both modern hard drive read-heads and the emergent technology of magnetic random access memory. They consist of a ferromagnet/insulator/ferromagnet junction in which the TMR is defined by TMR $= (R_{ap} - R_p)/R_p$. With R_{ap} and R_p the resistance measured when the magnetisations of the left and right ferromagnetic layers, so called electrodes, are antiparallel or parallel, respectively. If the tunnelling process conserves spin then the resistance of the device is minimised when the electrodes have parallel magnetisation and the TMR is given by the Julliere formula [78],

$$\mathrm{TMR} = 2P_L P_R/(1 - P_L P_R). \tag{4.1}$$

Here P_L and P_R are the spin polarisation at the Fermi level (E_F) of the left and right electrodes, respectively. Most MTJs contain conventional transition metal-based ferromagnets that have only partial spin polarisation, limiting the TMR [79]. Large TMR values are obtained when the wave functions in the electrodes and the barrier are matched such that tunnelling of the most highly polarised carriers is favoured. Alternatively, to maximise the TMR, fully spin-polarised half-metallic ferromagnets such as Heusler alloys [80, 81], manganites [82], or dilute magnetic

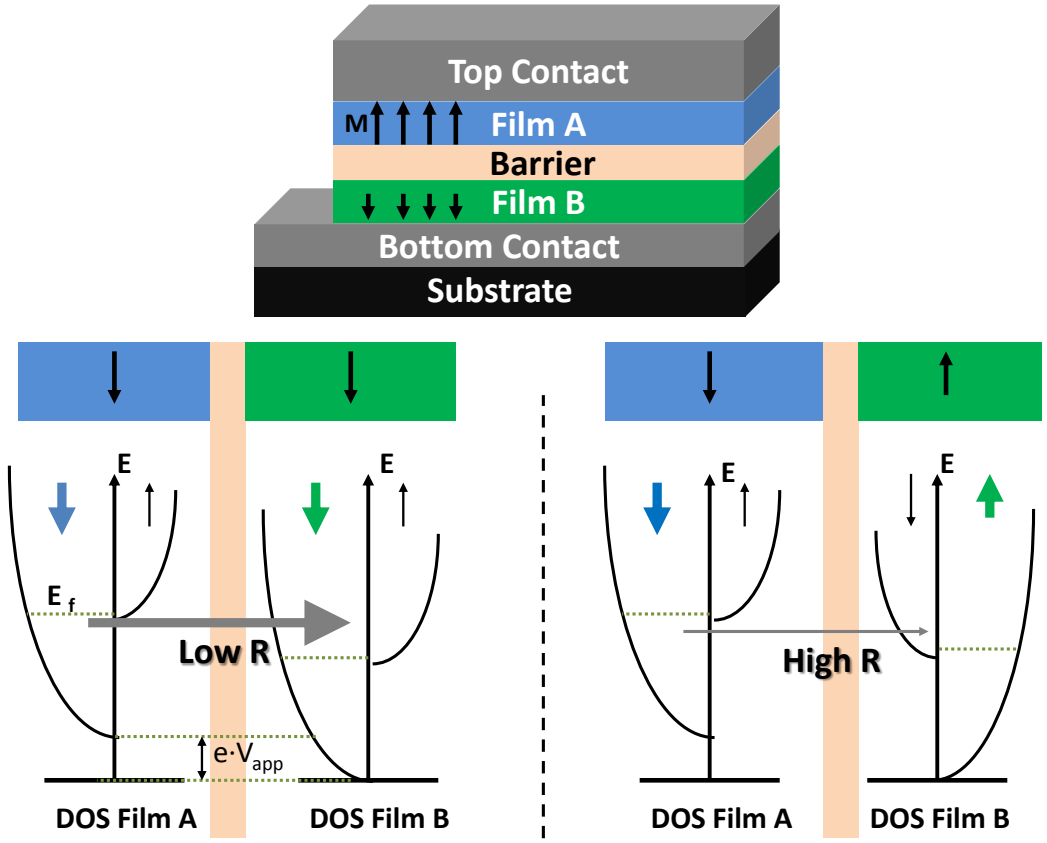

Figure 4.1 – Schematic diagram of a magnetic tunnel junction and the energy band structure of the MTJ in its high and low resistance states. When in the off state the resistance is much higher because the electrons must tunnel from majority to minority spin state.

semiconductors (DMS) can be used [83,84]. TMR values of more than 1800% have been observed in such manganite systems at low temperatures. DMS systems are of special interest because the carrier concentration, the Fermi level, and the nature of the conduction wave functions can in principle be tuned. However such tuning is not always possible without also influencing the Curie temperature (T_C) of the DMS. Thus it is of substantial interest to investigate TMR in devices with the electrodes fabricated from *intrinsic* ferromagnetic semiconductors.

Magnetic tunnel junctions are devices which act as a switch, with their on/off state controlled by an external action. This action most often comes in the form

of an applied magnetic field[1]. However, there is an increasing interest in devices based both on electric field-induced switching (such as in multiferroics [85]) and on current controlled switching where the spin of the electrons is used to switch the magnetisation of the free layer in a device [86]. This effect is known as spin-transfer torque and promises smaller, simpler devices with decreased power consumption. By controlling the magnetic properties using an electric current, as opposed to an external magnetic field, the need for extraneous electromagnets is removed and the system can be scaled down to technologically relevant bit densities. Clearly spin-transfer torque controlled magnetic tunnel junctions are of high technological value. There are potential benefits to be gained by having a semiconducting system with a lower number of carriers in the conduction band. This may reduce the threshold current required to flip the magnetisation of the layers.

When the electrodes used in a MTJ are ferromagnetic semiconductors the spin polarisation of the layers can result in very large TMR values. When the spin polarisation of the two layers is aligned the electrons are tunnelling from a band of majority spin polarisation into a majority band, with many free states above the Fermi level resulting in a low resistance. Conversely, when the magnetisations are anti-aligned the electrons must tunnel either into or out of a minority band with a low number of states giving a consequently higher resistance. As mentioned in Chapter 2, the rare-earth nitride series includes members combining semiconductivity with complementary magnetic properties [24, 25, 27, 30–34]. The most thoroughly studied rare-earth nitride is GdN. Below the 50-70 K T_C it is a semiconductor with an indirect band gap of $\sim$ 0.3 eV [47]. A large exchange splitting of both the conduction and valence bands means that carriers at the band edges are expected to be fully spin polarised [1]. The spin polarisation in GdN has been reported at 80% experimentally for thin layers, with a prediction of 100% for thick >10 nm layers [14, 87]. For a 100% polarisation, Equation 4.1 leads to an infinite TMR, making magnetic semiconductors interesting candidates for large

[1]In order to produce localised magnetic fields extra device elements such as crossed-wires must be employed. This introduces further components, and thus fabrication steps to the device manufacturing process. There is a fundamental size limitation imposed by these localised magnets due to their fringe fields which ultimately limits the maximum device density.

TMR values[2].

For the above reasons, the RENs could be used as novel electrodes with large spin polarisation in tunnel junctions. On top of their use as electrode materials is the potential for epitaxial incorporation with group-III nitrides, which present themselves as an obvious choice of tunnel barrier material. Enhancing this potential is the fact that these barriers may enhance the spin polarisation of the tunnelling electrons due to their crystal structure. It has been predicted that barriers lacking a centre of inversion symmetry give a significant spin polarisation to electrons tunnelling through them [88]. Both AlN and GaN grow in the wurtzite structure and so are non-centrosymmetric, making them candidates for highly efficient tunnel barriers. Incorporating both unconventional ferromagnetic electrodes and a novel barrier material into tunnel junctions may give rise to further understanding of the physics of magnetic tunnel junctions. Demonstrated here is one such device using gadolinium nitride as the ferromagnetic electrodes in an all semiconductor GdN/I/GdN (I=AlN,GaN) magnetic tunnel junction.

4.2.2 Experimental Details

Magnetic tunnel junctions consisting of GdN electrodes separated by a thin GaN or AlN tunnel barrier were grown at room temperature in a vacuum system with base pressure 1×10^{-8} mbar. For the GdN layers, gadolinium metal was evaporated from an electron gun at a rate of $0.2-0.5$ Å/s under a nitrogen partial pressure of $(1-10)\times10^{-5}$ mbar. GaN barriers were grown in a similar fashion, but with activated nitrogen supplied from a Kaufman ion source. AlN barriers were grown in the same fashion, with the aluminium evaporated using an effusion cell. By including a tunnel barrier which instils a large perpendicular resistance, the device resistance can be made to vastly exceed the resistance of the leads and so the effects discussed in Section 3.5 are mitigated. Refer to Section 3.1 for more sample preparation details.

Tunnel junctions were formed by photolithography in a cross-contact geom-

[2]In practice other effects such as the properties of the barrier and interfaces are likely to impede the maximum TMR value that can be achieved.

etry, as shown schematically in Figure 4.2(a). A narrow (100 µm) gold contact strip of thickness 50 nm was deposited on to a sapphire substrate. This was patterned using photolithography followed by a metal lift-off process as described in Section 3.2. The substrate and gold electrode were then covered by a layer of photoresist and a 200 µm wide channel was fabricated by photolithography orthogonal to the gold strip. The GdN/I/GdN tunnel junctions were then deposited, followed by a top layer of ∼45 nm gadolinium metal that acts as a capping layer to prevent oxidation of the GdN and also acts as a top contact for the MTJ. After depositing the tunnel junction and the Gd layer the photoresist was removed via a second lift-off process. A cross-section SEM image showing the junction stack is displayed in Figure 4.2(b), which shows the GdN layers are each about 60 nm thick. X-ray reflectometry measurements are useful for measuring the thickness and roughness of thin films. However, the penetration depth of x-rays rules this technique out for the thick multilayers used in these tunnel junctions. Instead, in order to ascertain the thickness of the barriers used in this project, x-ray reflectometry measurements were performed on a GaN layer grown under the same conditions as the tunnel barriers[3]. The results of these measurements, along with the fit used to extract the layer parameters, are shown in Figure 4.3. This yielded a GaN thickness of several (~ 5) nm, consistent with the SEM results. The GaN layer roughness was found to be 0.5 nm, although this may differ for GaN layers in tunnel junctions due to the different roughness of the GdN layer beneath. In order to examine the quality of the GdN layers used in tunnel junctions, a ∼100 nm single-layer GdN film was prepared under nominally identical growth conditions to those used in the MTJs and capped with a ∼30 nm thick GaN layer instead of a Gd layer. An X-ray diffraction (θ-2θ scan) displayed in Figure 4.4 reveals that the GdN is polycrystalline, strongly (111) textured, and with an out of plane lattice parameter of 5.00±0.01 Å[4]. It was necessary to grow a control layer to perform these measurements as the Gd capping layer on the tunnel junction films has XRD peaks very close to the GdN (111) peak, which makes a quantitative analysis of the layers

[3]These measurements were performed with assistance from Olly Pantoja and Jay Chan.

[4]Note that the (unlabelled) XRD peaks close to the sapphire reference peak are experimental artefacts.

more difficult. This can be seen in Figure 4.5 which displays XRD patterns of three different magnetic tunnel junctions each capped with Gd metal. While the peaks from the GdN and SmN layers are visible, they are unresolved and in close proximity to Gd peaks from the capping layer making fitting difficult. The Gd layer also makes magnetic measurements difficult. The metallic Gd layer is ferromagnetic up to room temperature and is expected to break the symmetry between the magnetic properties of the top and bottom ferromagnetic GdN layers [79]. SQUID measurements of the temperature dependent magnetic moment performed on a GdN/GaN/GdN/Gd magnetic tunnel junction are displayed in Figure 4.6. It is clear that in Fig 4.6 there are contributions from both the Gd layer (setting in near room temperature) and the GdN layers (at around 50 K). While it is difficult to separate the contribution from the two layers it is still somewhat useful for estimating their Curie temperatures. Similarly, for field loops (magnetic moment as a function of applied field) from the same sample, because the two contributions cannot easily be separated the saturation magnetisation cannot be measured. However the data, displayed in Figure 4.7, is still useful to put an upper bound of 500 Oe on the coercive field of the layers at 5 K (although it is unclear whether the Gd or GdN contribution dominates).

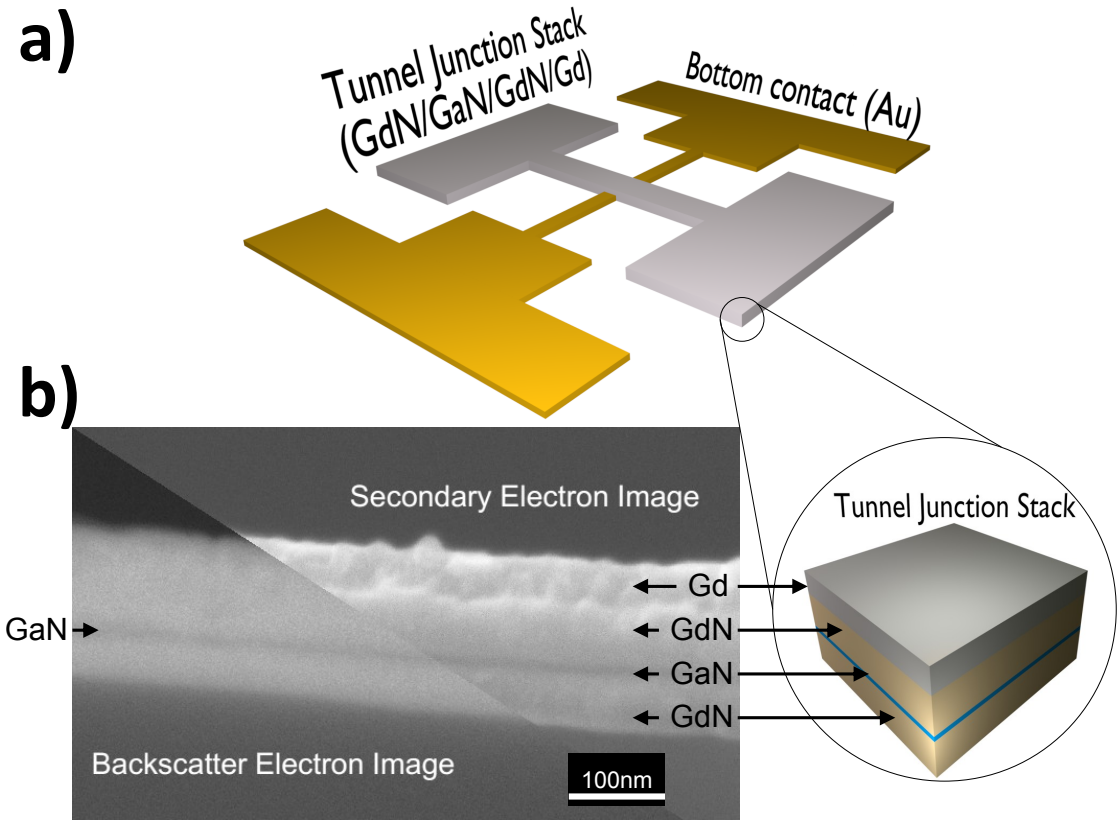

Figure 4.2 – (a) Schematic illustration of the entire MTJ geometry, where the "tunnel junction stack" consists of the stack shown at lower right. The tunnel junction area is 100 µm×200 µm. (b) Cross-section SEM images of the GdN/GaN/GdN tunnel junction obtained by both backscatter and secondary electron imaging. The backscatter image highlights the GaN layer.

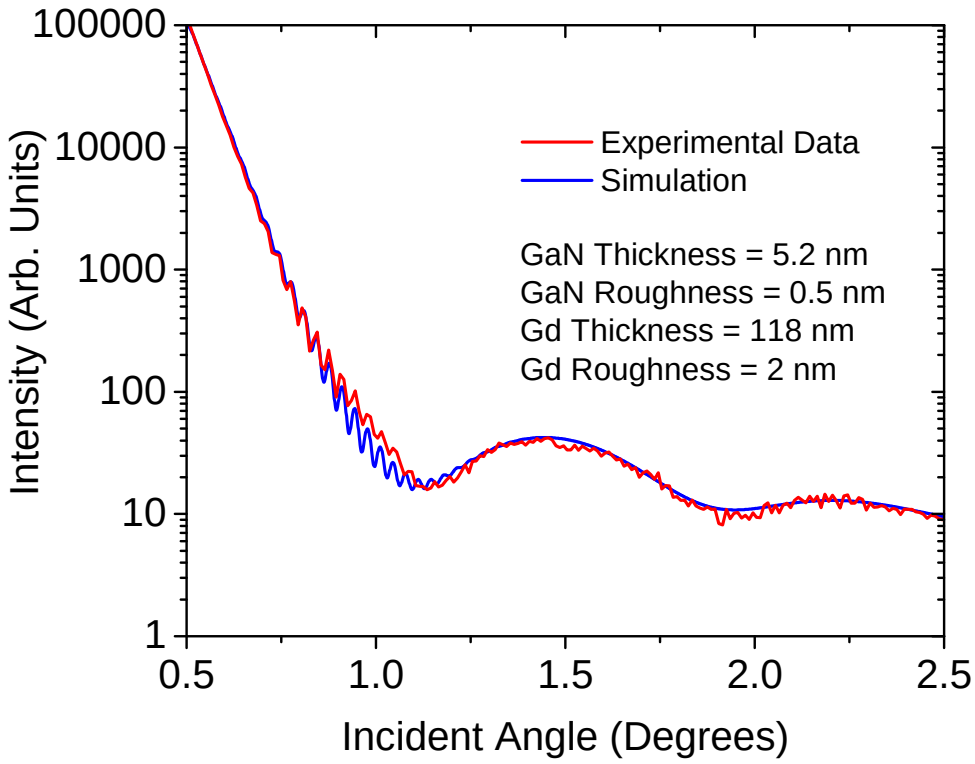

Figure 4.3 – X-ray reflectivity data from a GaN/Gd sample. This shows interference fringes with two different periodicities, which are related to the GaN and Gd layers. A fit to the data has been used to extract the layer thicknesses and roughness.

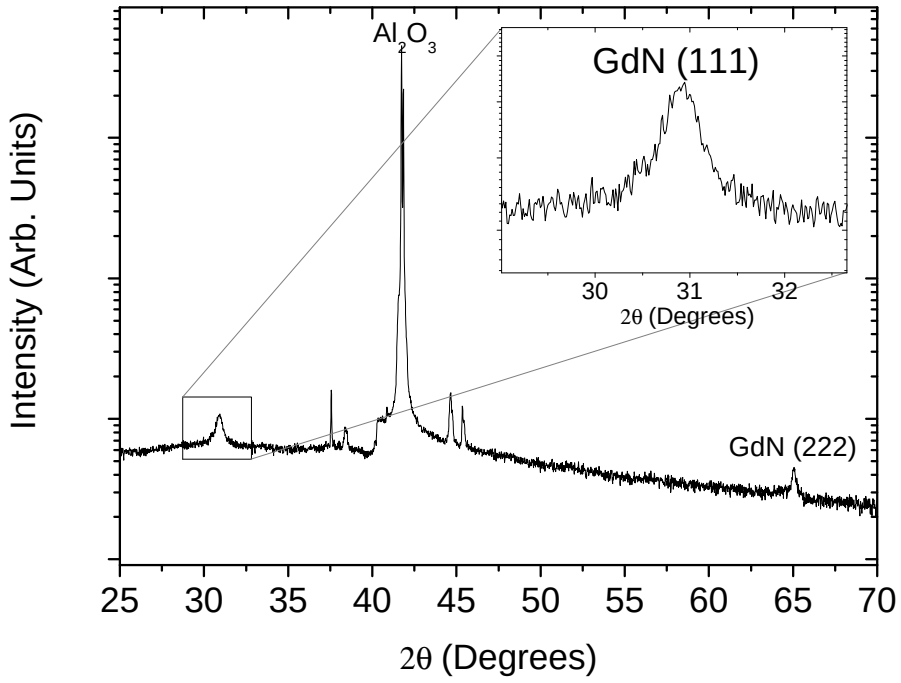

Figure 4.4 – θ-2θ x-ray diffraction pattern from a GdN control layer grown under nominally identical conditions to the tunnel junctions. Inset: Expanded XRD pattern around the GdN (111) peak.

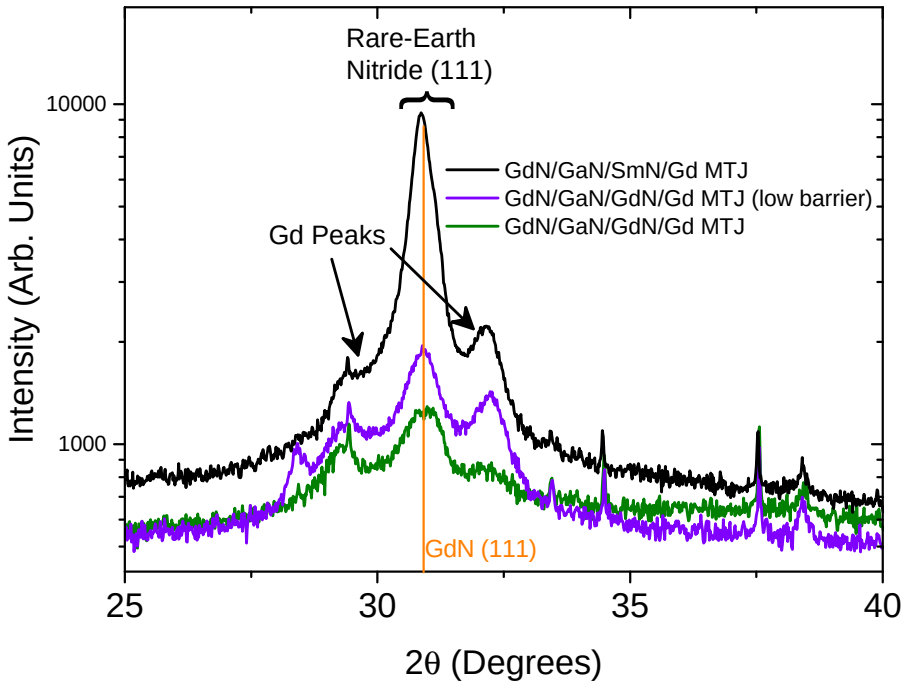

Figure 4.5 – θ-2θ x-ray diffraction pattern from several tunnel junction samples with Gd capping layers.

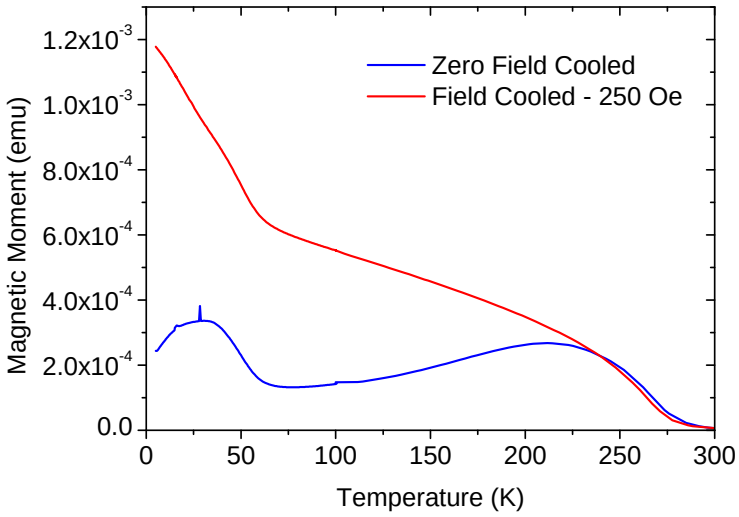

Figure 4.6 – ZFC/FC data of the magnetic moment vs. temperature for a GdN/-GaN/GdN/Gd tunnel junction.

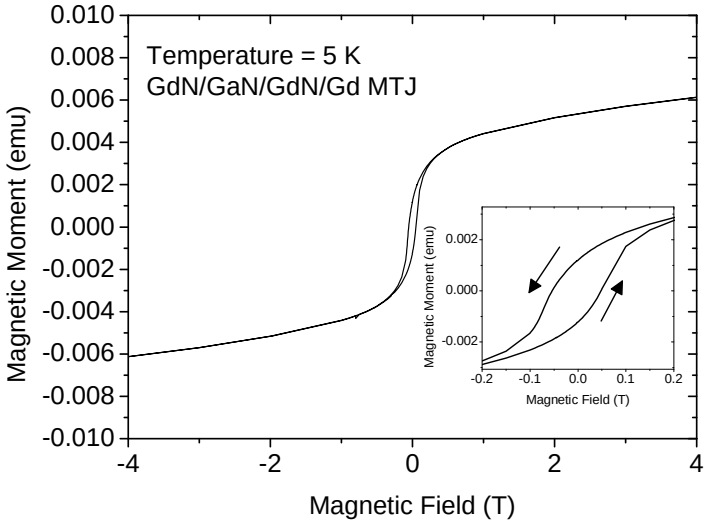

Figure 4.7 – Field loop (magnetic moment vs. H) at 5 K for a GdN/GaN/GdN/Gd tunnel junction.

4.2.3 Simmons Model

Current-voltage characteristics of magnetic tunnel junctions can be understood using a variety of different models. The problem of electrons in metal contacts tunnelling through a barrier is not new, having been studied since at least the 1930s [89–91]. One of the most widely employed models for studying real systems is that of Simmons [92], which is relatively simple to understand and is expressed in terms of useful parameters such as the average barrier height and width[5]. There are numerous more complicated models to account for effects such as spin dependent tunnelling [93], or using the joint density of states of the electrodes via Fermi's golden rule [94]. Despite the availability of more sophisticated models it makes sense to first employ the simplest model in order to understand the broad behaviour and differences between similar devices. If needed, more subtle effects can then be accounted for by employing one of these more sophisticated models. For these reasons the Simmons model has been used to interpret and understand the current-voltage characteristics of tunnel junctions studied in this project. A derivation of the Simmons model, including the temperature dependence, may be found in Appendix E.

A schematic diagram of the tunnelling situation is depicted in Figure 4.8 both with and without an applied voltage. With zero applied voltage the barrier is rectangular and the Fermi level aligned across the device structure. With an applied voltage there is a deformation of the barrier which is accounted for within the framework of the Simmons model. With this applied voltage there is an induced current of electrons tunnelling through the barrier. Simmons solves for the current density in several different cases with symmetric/asymmetric barriers, different voltage regimes and with image forces included.

For a rectangular barrier, without inclusion of the image forces, Simmons finds

[5]Caveat: These barrier parameters are approximate values. It is unlikely that there will be a uniform barrier width or height, so they represent more of an average height and width. They are useful in order to understand and compare devices, and also to obtain a picture of the band offsets. The thickness in particular may not match other estimates of the barrier thickness. This is partly due to the fact that tunnelling is dominated by the thinnest parts of the barrier.

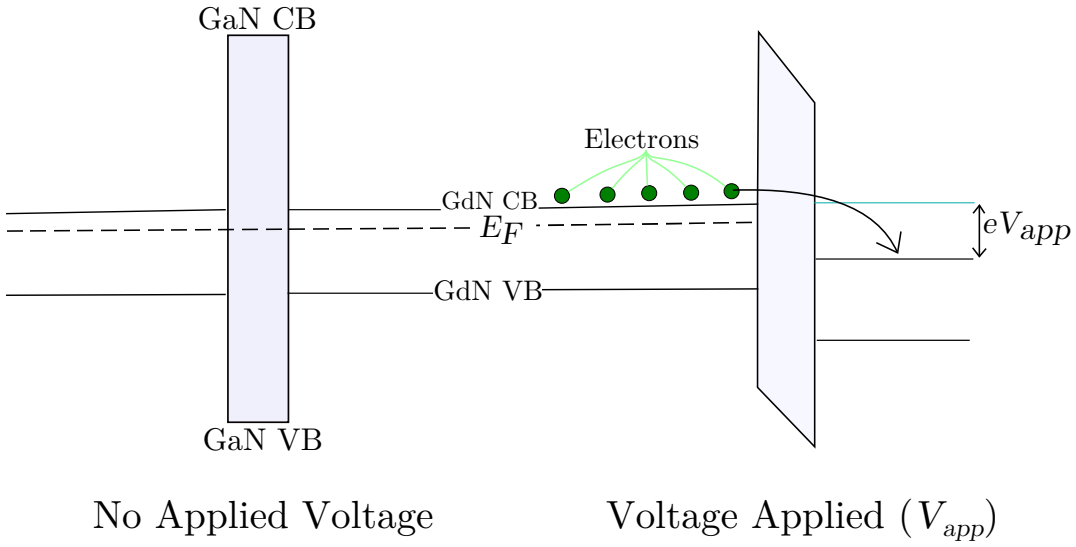

Figure 4.8 – Schematic diagram of a tunnel junction with and without an applied voltage, illustrating the deformation of the barrier height under an applied voltage.

for applied voltages less than the barrier height:

$$J(V,0) = \frac{6.2 \times 10^{10}}{s^2} \left\{ (\varphi_0 - V/2) \exp\left(-1.025 s (\varphi_0 - V/2)^{\frac{1}{2}}\right) - (\varphi_0 + V/2) \exp\left(-1.025 s (\varphi_0 + V/2)^{\frac{1}{2}}\right) \right\},$$

where s is the barrier width, φ_0 is the barrier height, V is the applied voltage, and J is the current density.

Although a small correction in most cases, it is possible to account for the image forces within the framework of the Simmons model[6]. For intermediate voltages, including the effect of image forces modifies the Simmons model for a rectangular

[6]Image charges are imaginary charges which are used to replicate the boundary conditions in certain electrostatics problems. An electron approaching a dielectric layer induces a positive charge on the interface which acts like an image charge within the layer. In the case of tunnel barriers image charges accumulate in the electrodes as carriers approach the barrier interface. The image potential due to these charges reduces the effective barrier height and width by rounding off the corners of the barrier. The effect of the image potential is generally small compared to the barrier height.

barrier by substituting φ_0 with a new barrier height

$$\varphi_I = \varphi_0 - (V/2s)(s_1 + s_2) - \frac{5.75}{K(s_2 - s_1)} \ln \left[\frac{s_2(s - s_1)}{s_1(s - s_2)} \right], \tag{4.2}$$

where K is the dielectric constant of the barrier and s_1, s_2 are the limits of the barrier at the Fermi level as defined in Appendix E. For a rectangular barrier and applied voltages less than the barrier height,

$$s_1 = 6/K\varphi_0, \tag{4.3}$$

$$s_2 = s \left[1 - \frac{46}{3\varphi_0 K s + 20 - 2VKs} \right] + 6/K\varphi_0. \tag{4.4}$$

Inserting Equations 4.3 and 4.4 into Eq. 4.2 gives a barrier height which can be used in:

$$J(V,0) = (6.2 \times 10^{10}/\Delta s^2) \times \{\varphi_I \exp(-1.025\Delta s \varphi_I^{\frac{1}{2}}) - (\varphi_I + V) \exp -1.025\Delta s (\varphi_I + V)^{\frac{1}{2}}\} \tag{4.5}$$

to model the current density of a rectangular barrier with the image forces included[7]. The temperature dependence, for a symmetric barrier, is given by

$$J(V,T) = J(V,0) \left[1 + \frac{3 \times 10^{-9} \times s^2 T^2}{\varphi_0 - V/2} \right], \tag{4.6}$$

with $J(V,0)$ the current density at zero temperature given by the temperature independent Simmons model (Eq. 4.5) [92], s the barrier thickness, T the temperature, and φ_0 the barrier height [95]. A derivation of this is given in Section E.3. The full equation combining Equations 4.2-4.6 used for fitting of tunnel junction J-V characteristics can be found as Figure E.2 in Appendix E.

4.2.4 Features of the Simmons Model

In order to understand the electronic characteristics of devices, the Simmons model can be examined in order to understand the broad behaviour and estimate whether the resistance of devices agrees with the model. For all resistance calculations a

[7] Here $\Delta s = s_2 - s_1$.

barrier area of 2×10^{-4} cm^2 has been assumed in order to scale the current density into a resistance.

The current density-voltage characteristics as a function of temperature are included as Figure 4.9 and show that as the voltage is increased so is the current density. The J-V curve becomes steeper (more non-linear) as the temperature is decreased. Note that (not shown) for higher barriers, it is expected that the temperature dependence will be decreased as $k_B T << \bar{\varphi}$.

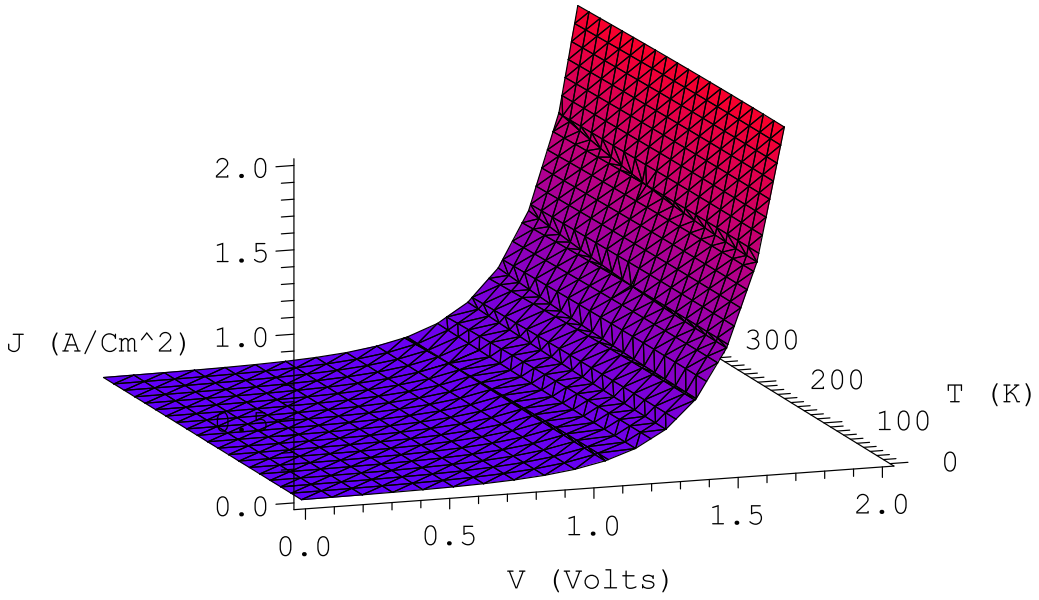

Figure 4.9 – Modelled current density plotted as a function of temperature and voltage. This calculation was performed using the rectangular Simmons model with a barrier of width 2 nm and height 1.6 eV. The image forces are not included here.

By changing the barrier thickness (by changing the growth time or rate) and height (by using a different material) it is possible to produce tunnel junctions with a variety of different resistances. Figure 4.10 depicts the junction resistance as a function of barrier height and width at 290 K. This calculation was performed using the rectangular Simmons model with image forces included, with applied voltage 0.01 V and a barrier dielectric constant of 9 which is close to that of GaN

and AlN at 300 K [96,97]. It is apparent that the resistance increases rapidly with both increasing barrier height and width.

Turning now to the barrier materials used in this project, the calculated resistance of devices with AlN and GaN barriers are examined in Figure 4.11, assuming a barrier height of roughly half the band gap [98,99]. In these plots the AlN barrier results in a much larger resistance than the GaN barrier. The resistance increases exponentially (linearly when plotted in a log scale) with increasing barrier width. It is apparent from these graphs that a wide variety of device resistances are possible by changing the barrier thickness slightly. For a fixed width of 2 nm the resistance as a function of barrier height is calculated and shown in Figure 4.12[8]. This figure is non-linear which, due to the log scale on the resistance axis, shows that the resistance does not increase exponentially with barrier height. This means that changing the barrier height does not have as marked an effect as changing the barrier width.

Now that the features of the Simmons tunnelling model in response to device parameters have been examined, it is time to turn to the experimental properties of devices.

4.3 GaN barriers with GdN electrodes

In this section the properties of GaN tunnel barriers with GdN electrodes are examined. These devices have been studied using electrical transport measurements including current voltage characteristics, temperature dependent resistivity and magnetoresistance measurements.

Current density-voltage (J-V) characteristics at 5 and 290 K of a typical GaN tunnel barrier are displayed in Figure 4.13. The curves are non-linear at all temperatures 5-290 K, as expected for a system dominated by tunnelling. The data fit well to the Simmons model for tunnelling through a rectangular barrier [92]. In our structure the temperature dependence of the current density follows the

[8] 2 nm has been used for modelling as this is of similar thickness to the values extracted from actual devices presented in the following sections of this thesis.

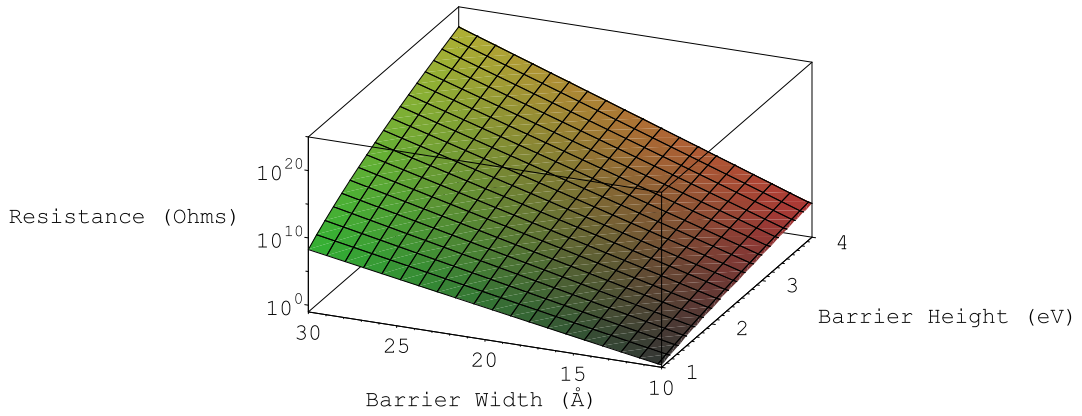

Figure 4.10 – Modelled resistance plotted as a function of barrier width and height at 290 K with an applied voltage of 0.01 V.

predicted quadratic relationship in Equation 4.6.

It was found that the data at all temperatures were fit extremely well with a barrier width of ∼1.9 nm, leaving the barrier height as the only temperature dependent fitting parameter. The inset to Fig. 4.13 shows the temperature dependent barrier height extracted from the fitting. The modelled barrier thickness is similar to SEM and x-ray reflectivity measurements, although slightly thinner than the best estimate of these, most likely due to the fact that tunnelling is dominated by the thinnest parts of the barrier. The barrier height is found to be 1.5 eV at room temperature and 1.65 eV at low temperatures, suggesting that the Fermi level lies close to the middle of the gap of the GaN barrier (assuming E_F in the GdN is close to the conduction band minimum). Note that this is in good agreement with the recent calculation of the band offsets between GdN and GaN which finds the GdN Fermi level to lie 1.19 eV above the GaN valence band maximum and close to mid-gap [100].

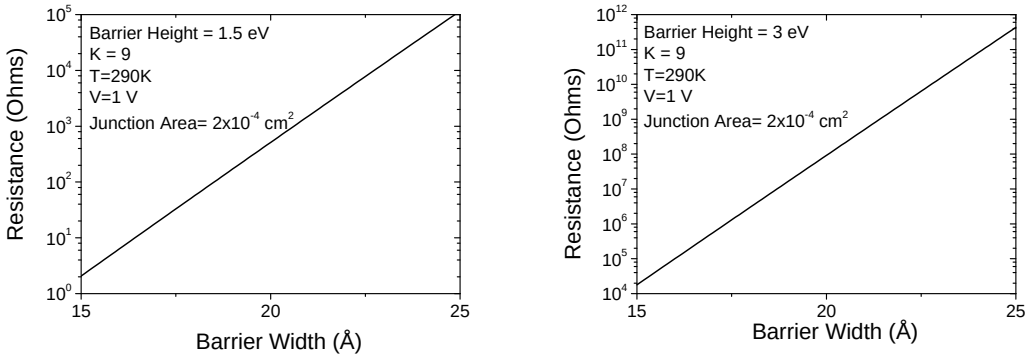

Figure 4.11 – Modelled resistance plotted as a function of barrier width for GaN and AlN barriers. This calculation was performed using the rectangular Simmons model with image forces included, at 290 K with applied voltage of 1 V and a barrier dielectric constant of 9.

The temperature dependent resistance of the tunnel barrier measured at different applied currents is shown in Figure 4.14. The resistance of the tunnel barrier measured at the smallest current (10 nA) is between four (at 5 K) and six (at 300 K) orders of magnitude larger than calculated from the GdN resistivity alone, so it is clear that the MTJ resistance is dominated by the GaN barrier. Indeed, an otherwise similar GdN control device with no GaN barrier (see Figure 3.15) was found to have a very low resistance ($< 1\ \Omega$) in the vertical transport orientation. For comparison the resistivity of a homogeneous GdN film measured in the van der Pauw geometry is shown in the inset to Fig. 4.14. The resistance of both the homogeneous film and the tunnel barrier show similar electronic structure, including a feature at 50 K near the Curie temperature of GdN. This is caused by the onset of exchange splitting of the GdN bands, which reduces the majority carrier activation energy and hence the resistance [1, 47]. It is striking that the density of states in the electrodes has such an important effect on the device characteristics. The peak near T_C is suppressed and the overall resistance decreases in the tunnel junction at higher currents, whereas for bulk GdN these effects are not seen. For larger applied currents, and hence voltages, the relative effect of band splitting

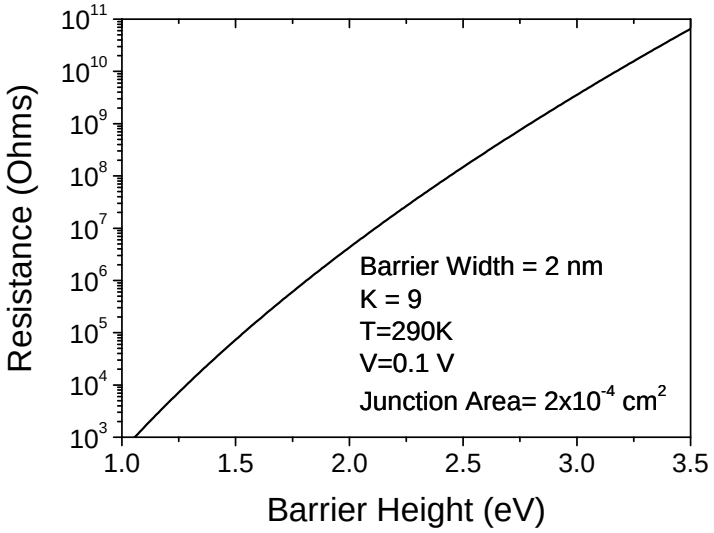

Figure 4.12 – Modelled resistance plotted as a function of barrier height. This calculation was performed using the rectangular Simmons model with image forces included, at 290 K with applied voltage 0.1 V and a barrier dielectric constant of 9. Note that a different (smaller) voltage was used in this calculation than in the width calculations, this is because the model fails as the applied voltage approaches the barrier height.

becomes diminished in comparison to the effect of the applied voltage on the barrier height. Clearly, transport through the tunnel junction is dominated by the presence of the GaN layer, but the density of states in the electrodes also has an important effect on the device characteristics. This is in contrast to conventional magnetic tunnel junctions, which have a large density of (extended) states at the Fermi level and consequently do not exhibit strong temperature dependence.

The magnetoresistance with low fields applied in the substrate plane for a GaN MTJ at 5 K is shown in Figure 4.15[9]. The low field magnetoresistance in Fig. 4.15(a) shows some hysteresis at fields comparable to the GdN coercive field (see Figure 4.7). While this is qualitatively different from the switching seen in conventional MTJs, it is also different in form to the hysteresis typically observed

[9]Here the definition of magnetoresistance in Equation 3.2 has been used.

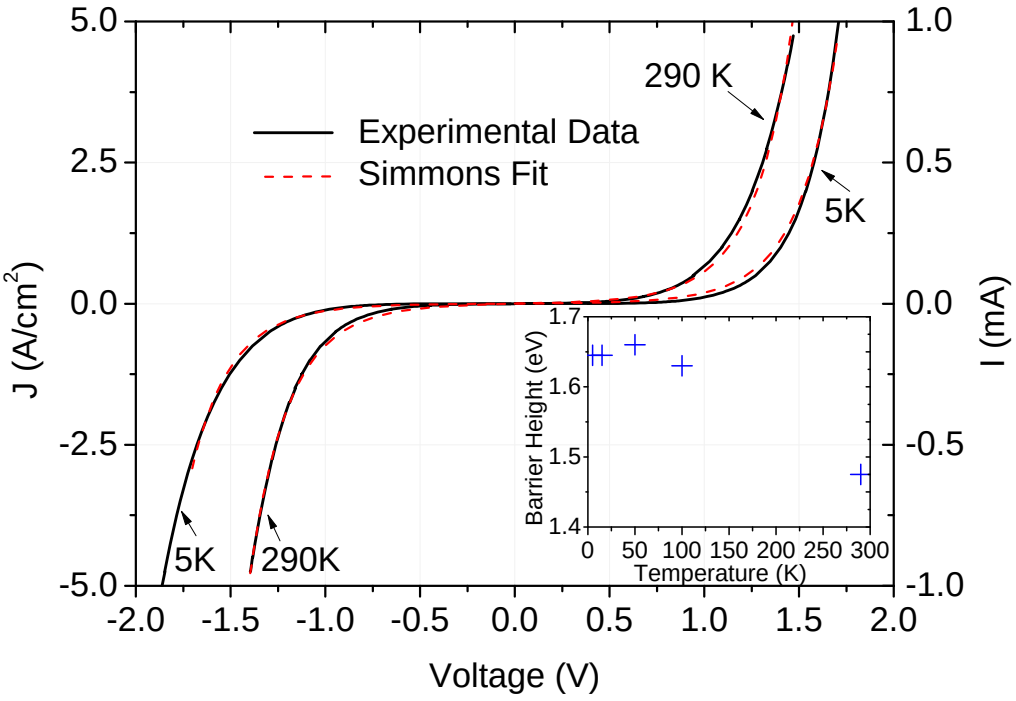

Figure 4.13 – Current-Voltage characteristics for the GdN/GaN/GdN tunnel junction fitted using the Simmons tunnelling model. Inset: Modelled barrier height (average of forward and reverse current) plotted against temperature, extracted assuming a fixed barrier width of 1.9 nm.

in bulk GdN films[10]. The high field magnetoresistance out to 8 T, visible in Figure 4.15 (b), is both large (> 50 %) and negative. The temperature dependent magnetoresistance, shown in Figure 4.16, shows a peak at T_C and then increases again at low temperatures. The temperature dependence of the magnetoresistance in this MTJ is different from bulk GdN films, which typically have a large (~ 50 %) MR at T_C that decreases at low temperatures [26][11].

[10]There are also features at 1000-3000 Oe which are hysteretic and not observed in bulk samples.

[11]Exchange-related magnetoresistance near T_C has been observed in a closely related and more widely studied compound, EuO, for which the Eu^{2+} ion shares the same *4-f* configuration as the

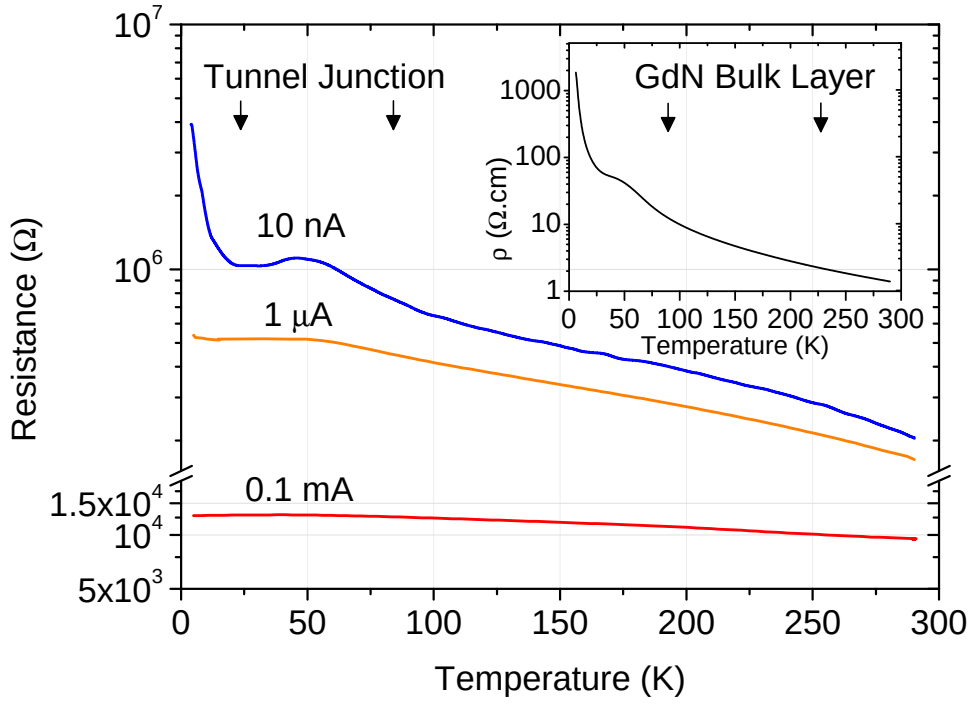

Figure 4.14 – Temperature dependent resistance of the GdN/GaN/GdN MTJ measured using various applied currents. Inset: Resistivity of a bulk GdN layer. The features in the resistivity of bulk GdN are reflected in the properties of the MTJ even though the MTJ resistance is clearly dominated by tunnelling.

The lack of characteristic switching typically exhibited by magnetic tunnel junctions is unsurprising given that the device is comprised of electrodes with similar properties, each of which is made up of multiple magnetic domains. The large number of magnetic domains will have a distribution of sizes and coercive fields [26], smearing out any switching behaviour. In order to induce magnetic switching in these REN MTJs the ratio of device size to magnetic domain size must be improved by either decreasing the device size or increasing the crystallite size using epitaxy. Another route to improved switching is to exploit the differ-

Gd^{3+} ions in GdN [101].

ent magnetic properties presented within the REN series. This is addressed in Chapter 5 using the huge coercive field contrast offered by SmN.

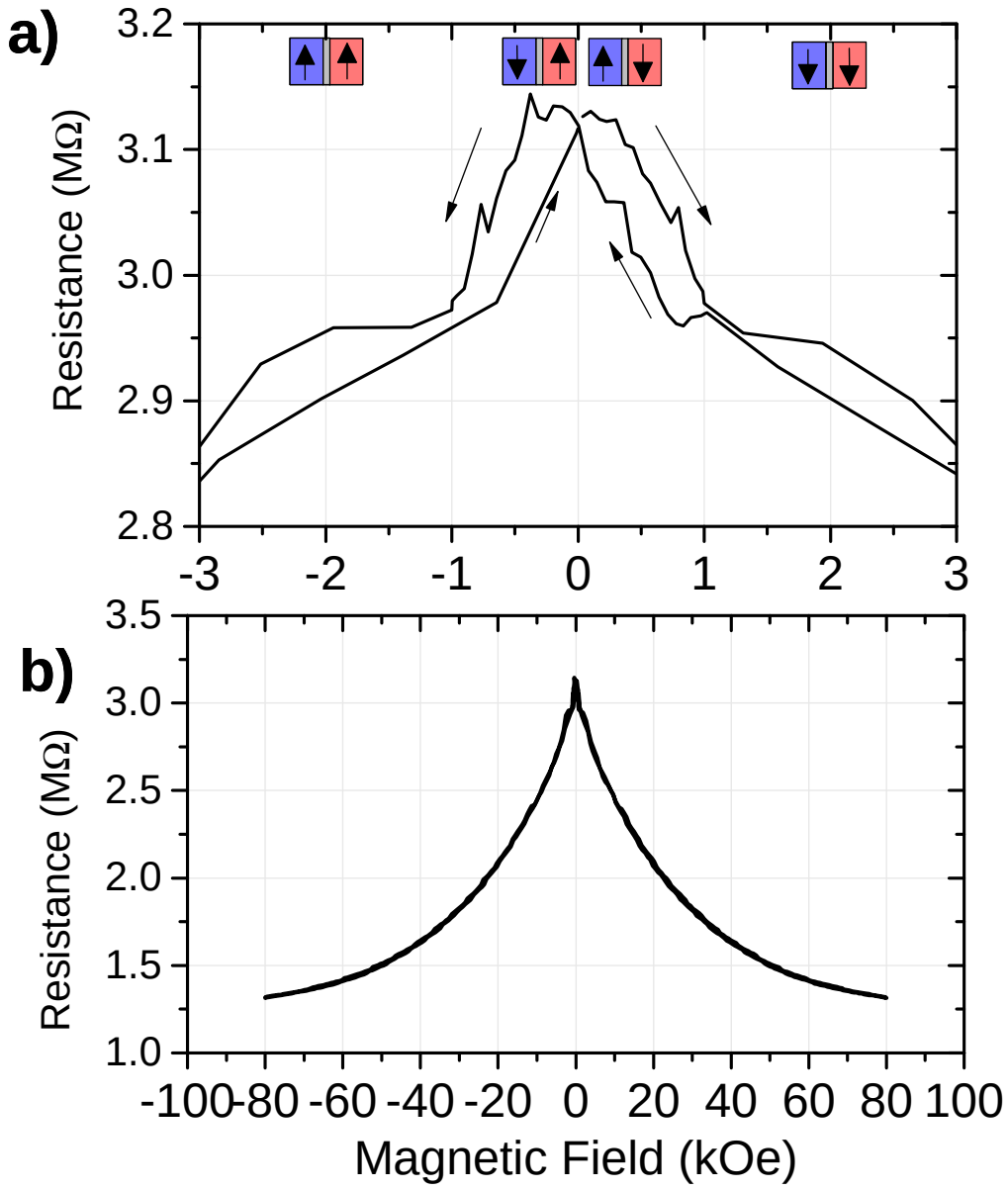

Figure 4.15 – (a) Field dependence of the tunnel junction magnetoresistance obtained from a GdN/GaN/GdN tunnel junction. Measurement performed using a current of ∼30 nA at 5 K with the applied field in-plane with the substrate. The diagrams above the data indicate the dominant magnetisation directions of the electrodes. (b) High field magnetoresistance data from the same sample.

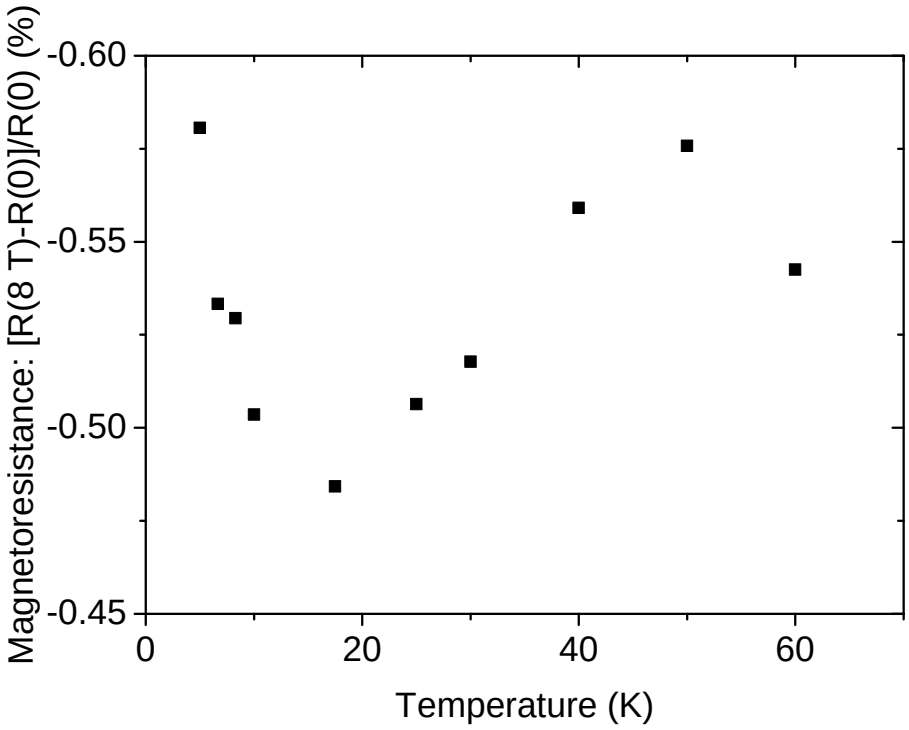

Figure 4.16 – High-field magnetoresistance amplitude from a GdN/GaN/GdN tunnel junction measured at temperatures between 5 K and 60 K (field in-plane).

4.4 AlN Barriers with GdN electrodes

In order to further investigate the properties of these GdN/I/GdN devices, the barrier material was changed from GaN to AlN. Given that GaN and AlN are group III nitrides, and thus share similar properties, the only significant difference between them is their band gap. GaN has a band gap of 3.4 eV [98], while AlN has a band gap of 6.2 eV [99]. This means that the barrier height of a tunnel junction grown using AlN should be roughly double that of GaN given that there is less than a 1 eV offset between the GaN and AlN mid-gap [102].

Current voltage characteristics at 5 and 290 K from a tunnel junction (Sample I) grown with an AlN barrier are displayed in Figure 4.17. The barrier height extracted from fitting was found to be ∼3 eV across the 5-290 K temperature range as expected for the doubled band gap. The barrier width was held fixed at 15 Å to extract the temperature dependent barrier height[12]. The doubled barrier height when going from GaN to AlN suggests that the barrier height scales with the band gap of the III-V nitride barrier, as expected given the less than 1 eV band offset between the two materials [102].

Interestingly, Sample I was not the most resistive sample with an AlN barrier. This is because the device resistance depends on both the barrier height and width. A second sample (Sample II) showed higher resistance with a slightly lower barrier height (2.5-2.7 eV) but larger barrier width (17Å). IV-characteristics at 5 and 290 K from sample II are shown in Figure 4.18. These are strongly non-linear at all temperatures much like the I-V curves obtained for GaN barriers. This was investigated further for a series of AlN samples of different barrier widths, where the growth conditions of barriers was kept the same and the growth time increased between samples. A trend of decreasing barrier height with increasing barrier width was found. Figure 4.19 displays this data for several such samples. One of these samples was grown with more conductive GdN by way of decreased

[12]Note that the IV curve is slightly asymmetric, having approximately a 0.1 eV larger barrier height in one direction. The inset to Fig. 4.17 is an average of the forward and reverse fitted barrier height. This asymmetry was observed in multiple junctions, and its origin remains an open question.

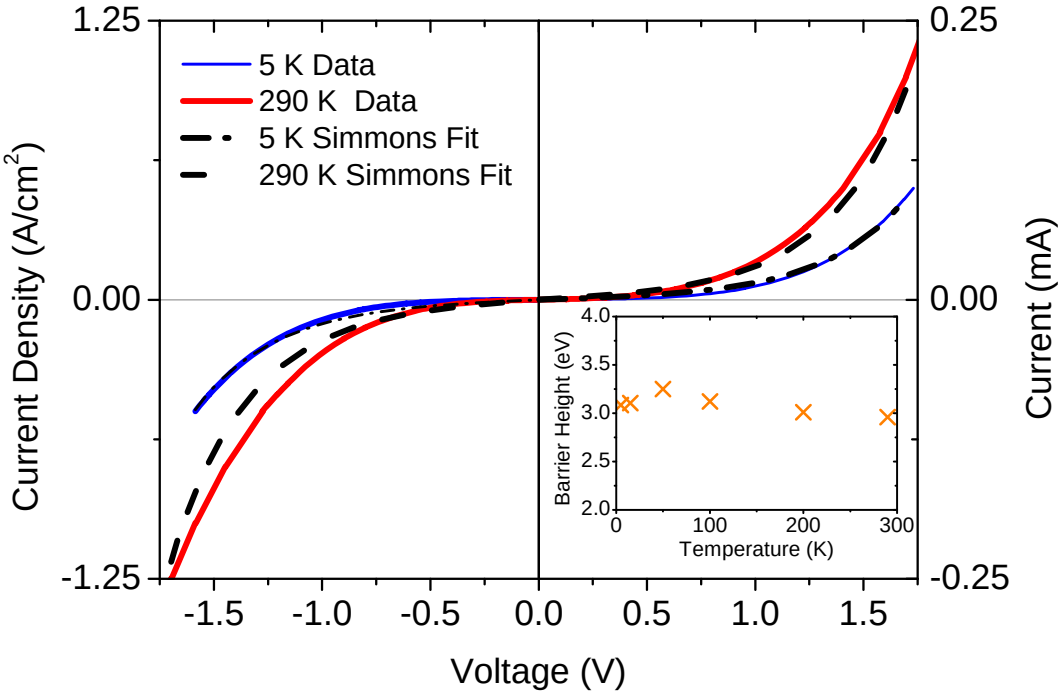

Figure 4.17 – IV characteristics for a tunnel junction (Sample I) with GdN electrodes and an AlN barrier. Inset: Barrier height plotted as a function of temperature.

N_2 pressure. This sample still conforms to the observed trend of decreasing barrier height with increasing barrier width.

The origin of this trend is likely to be due to the formation of Schottky barriers at the edge of the AlN barrier, giving a slightly higher barrier at the edges and an average barrier height which decreases with increasing barrier width. This is illustrated schematically in the inset to Fig. 4.19. Similar effects have been seen for tunnel junctions incorporating DyN and GdN barriers, where the barrier height decreased with increasing barrier width up to the point that diffusive transport through the barrier begins to dominate [13,14]. In the present case of AlN barriers it was not possible to reach this crossover regime as samples with thicker barriers had resistances exceeding 25 MΩ and were unable to be measured reliably.

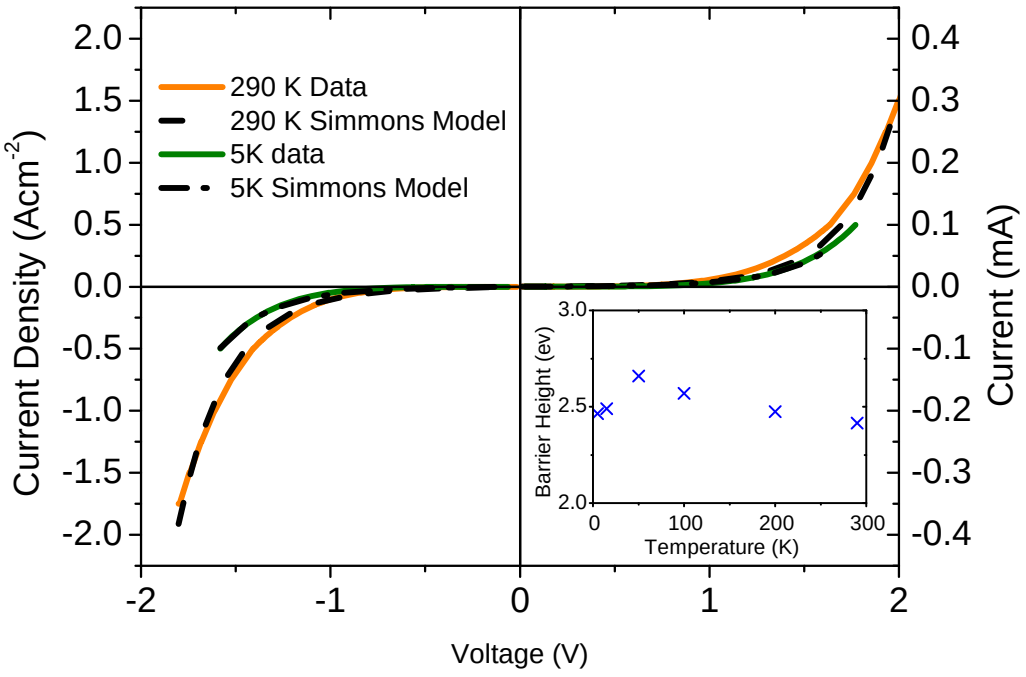

Figure 4.18 – IV characteristics for a tunnel junction (Sample II) with GdN electrodes and an AlN barrier. Inset: Barrier height plotted as a function of temperature.

The temperature dependent resistance for sample II is shown in Figure 4.20. This shows similar features to the GaN barrier in Figure 4.14 but with resistance values approximately one order of magnitude larger. For the highest currents, there is almost no temperature dependence as expected for such a large tunnel barrier in which case $k_B T << \bar{\varphi}$.

In these temperature dependent resistance curves there is a feature at 50 K corresponding to the GdN T_C. This occurs for both GaN and AlN barriers. This peak in the resistance coincides with the peak in the fitted barrier height vs. temperature. It is probable that the device resistance is not just a function of the barrier height and width as described by the Simmons model. The Simmons model does not take into account the density of states of the electrodes, which

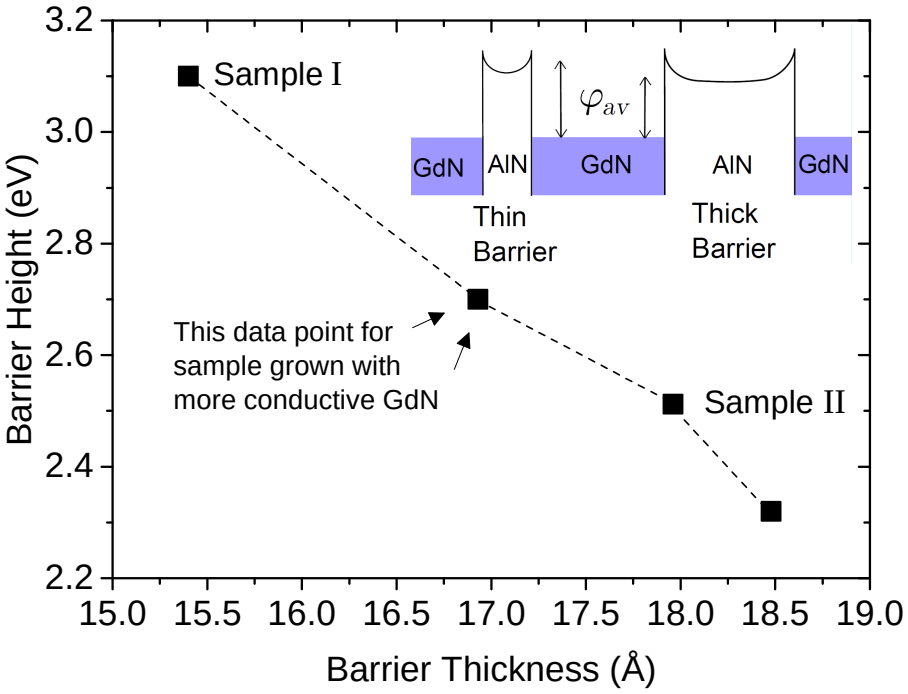

Figure 4.19 – Plot of fitted barrier height vs. width for samples grown with AlN barriers. Here the barrier height and width have been averaged over all temperatures measured. Inset: Schematic diagram of Schottky barriers formed at the edge of the AlN layer, which causes the average barrier height to decrease with increasing width.

is likely to modulate the resistance of the device. Below T_C there is an influx of carriers into the GdN conduction band, which may reduce the device resistance due to an increase in the number of electrons available for tunnelling (and hence anomalously reduce the fitted barrier height). There is also an increase of the barrier height with decreasing temperature well before the sample gets close to T_C. The band gap of both GaN and AlN increase by $\sim 0.1 - 0.2$ eV between room temperature and5 K [96, 103], which is one possible cause of the increase in barrier height as the sample is cooled. Simmons also notes that a temperature dependent dielectric constant (which both GaN and AlN possess) will produce an additional temperature dependence in the J-V characteristics [95].

Given the apparent dependence of the tunnel resistance on the density of states of the electrodes, there is potential for the properties of these junctions to be tuned. This could occur by the application of electric fields or by the inclusion of dopants in the semiconducting electrodes. Having magnetic tunnel junctions with tuneable electrodes may lead to increased functionality.

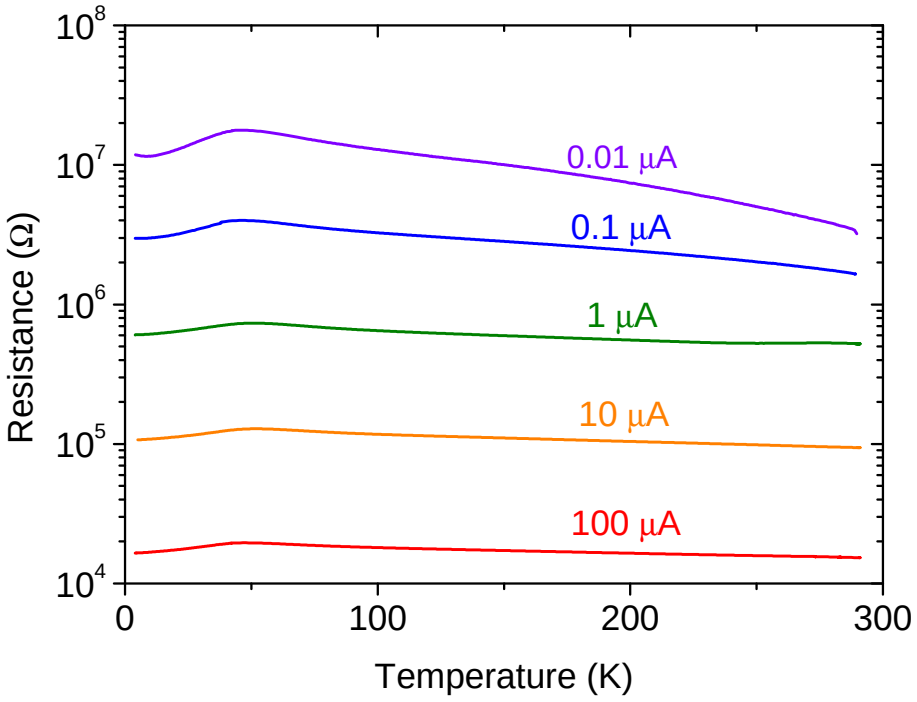

Figure 4.20 – Temperature dependent resistance of sample II measured using different currents.

4.5 Ga Rich Barriers

Tunnel junction samples were also prepared with slightly Ga rich GaN barriers grown at lower partial pressures of nitrogen. This causes the GaN to be nitrogen deficient, raising the Fermi level. These samples present an opportunity for examining the properties of rare-earth nitride tunnel junctions when the barrier is very low.

Current-voltage characteristics for one of these samples are shown in Figure 4.21. Here the I-V characteristics are linear with a very small low-bias resistance at 290 K and non-linear with much larger low-bias resistance at 5 K. Using the rectangular Simmons model to fit these samples reveals barrier heights between 0.1 and 0.3 eV at 5 K for samples of different GaN doping levels. Care should be taken in interpreting these fits as the WKB approximation used in the Simmons model derivation breaks down for low/narrow barriers. The barrier height can be examined from the I-V curves by taking the derivative and plotting dI/dV against V as has been done in the inset to Fig. 4.21. In this case there is a peak in the dI/dV curve corresponding to the barrier height. This barrier height of 0.12 eV agrees well with the rectangular Simmons fit of 0.12 eV. When the temperature dependence and images forces are included in the Simmons model the extracted barrier height of 0.2 eV agrees less well with the dI/dV measurement, perhaps due to the fact that the barrier is low. For the higher (GaN or AlN) barriers presented elsewhere in this thesis the difference in fitted thickness when image forces and the temperature dependence is included is much smaller, being of order 10 %. The Ga rich barrier sample in Fig. 4.21 showed a magnetoresistance similar to bulk GdN which decreased at low temperatures from ~ 35 % at 10 K to ~ 25 % at 5 K, perhaps signalling that the device is compromised by pinholes (see Section 4.6 for further discussion).

For some of these samples with a low barrier height, the resistance at high temperatures is so low that the diagonal contact resistance begins to dominate, meaning that the apparent resistance becomes negative at high temperatures as outlined in Section 3.5. Temperature dependent resistance of one such sample is included in Figure 4.22. For this device the I-V characteristics go from linear

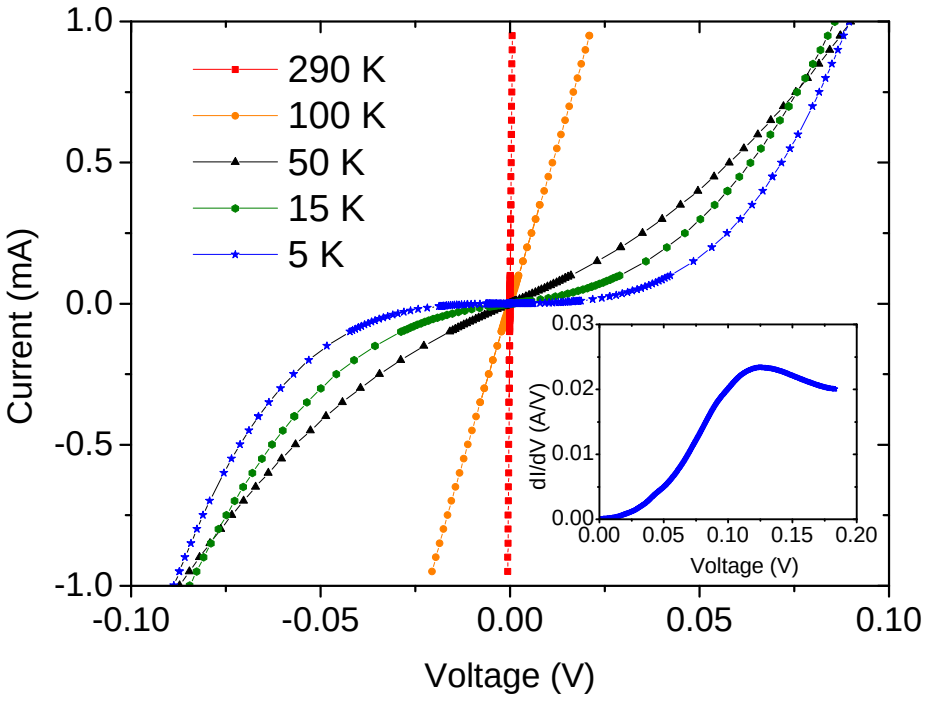

Figure 4.21 – Current-voltage characteristics of a GdN/GaN/GdN tunnel junction with a low barrier height at various temperatures. Inset: dI/dV measurement at 5 K.

with a negative resistance at high temperatures (where the contact dominates) to non-linear at 5 K with a fitted barrier height of 0.1 eV.

This crossover point for the resistance has been discussed in magnetoresistive tunnel junctions by van der Veerdonk et al. [104]. They note that in these junctions, a change in the apparent resistance due to the magnetoresistance of the junction can result in a large apparent magnetoresistance for the device as a whole. Imagine for instance that a device was fabricated such that the junction and lead resistances are equal. In this case, the apparent resistance would be zero until a magnetic field was applied. This applied field changes the junction resistance without affecting the contact resistance, and the apparent magnetoresistance would be

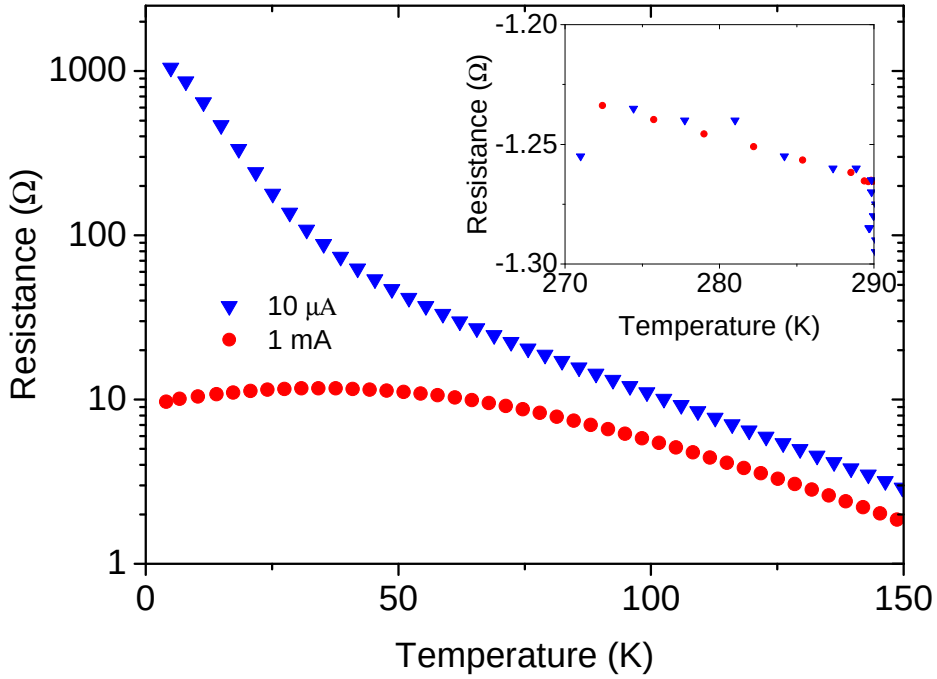

Figure 4.22 – Temperature dependent resistance for a sample with a low GaN barrier and a negative resistance at high temperature.

infinite. This apparently infinite on/off ratio does not necessarily lead to increased potential in applications, because although the relative change is large the signal voltage (and absolute change in resistance) is still very small.

This method of tailoring the barrier height may prove useful for future device applications, where the device resistance could be optimised for the desired application. As these devices were not observed to be switching in magnetoresistance measurements, it is not clear what effect such a low barrier height will have on the spin coherence of the tunnel current. At some point it is also expected that variable range hopping within the barrier, or even diffusive conduction through the barrier will begin to be the primary conduction mechanism. For these barriers it is difficult to rule out the possibility that there might be pinholes in the barrier creating parasitic resistance pathways in the linear IV regime, as will be discussed

in more detail in Section 4.6.

4.6 Pinholes in Tunnel Junctions

If a tunnel barrier is too thin, or discontinuous due to roughness, a short circuit known as a pinhole can form between the top and bottom electrodes. This is illustrated schematically in Figure 4.23. In such a device some, or all, of the current will flow through this low resistance pathway. Criteria have been developed to test for pinholes in systems containing metallic electrodes [105, 106], however these do not necessarily carry over to semiconducting electrodes.

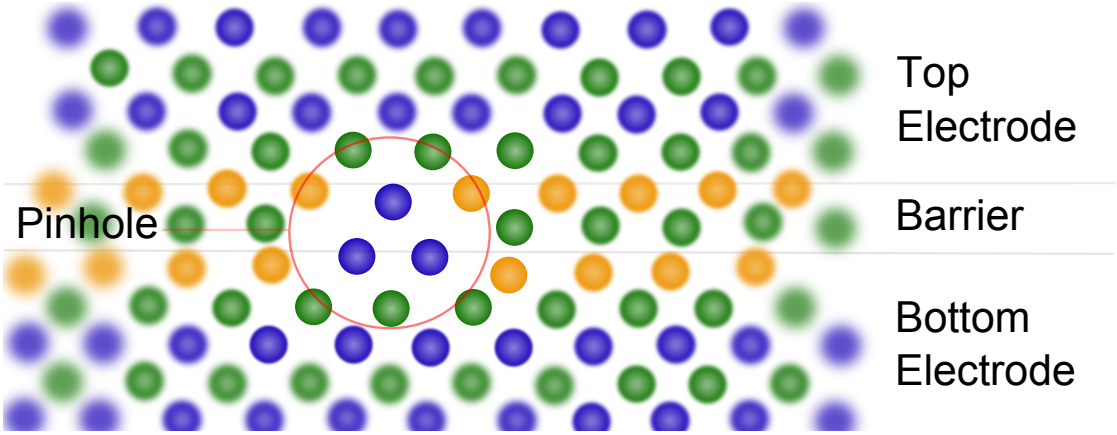

Figure 4.23 – Schematic diagram of a pinhole causing a tunnel junction to short-circuit. Here blue spheres represent rare-earth ions, green nitrogen ions, and orange group III ions.

The criteria for metallic pinholes are [106]:

1. Metal like R(T) regardless of bias.
2. Decreasing fitted barrier height and increasing fitted barrier width for decreasing temperature.
3. Increased junction noise at finite bias.
4. Increased junction instability at finite bias.

In the case of semiconducting electrodes, the pinholes would themselves be semiconducting rather than metallic. The TCR would also be opposite in sign and so the first two of these would need to be redefined as:

1. Semiconductor like R(T) regardless of bias.

2. Increasing fitted barrier height and decreasing fitted barrier width for decreasing temperature. This is because the pinholes in a metallic system become more conductive as the temperature is decreased which will "fool" the model into thinking the device is becoming more conductive due to properties of the barrier. In a semiconducting system the pinholes are expected to become more resistive as the temperature decreases. For truly semiconducting pinholes the resistance will diverge at low temperatures regardless of the bias. This would result in fitted barrier heights and widths which increase rapidly at low temperatures.

There are several observations in our tunnel junctions which are apparently inconsistent with the existence of pinholes. First note that the non-linear region is clearly dominated by tunnelling. This means that the low-bias region is the only place where the measurements could be effected by parasitic resistance pathways. The low bias R(T) data is similar in form to the data at high bias, and there are several other observations inconsistent with pinholes:

- A linear region at low bias is expected for a tunnelling system. The resistive GdN/I/GdN devices in this thesis have I-V curves even more resistive and non-linear at low bias than expected by the Simmons model. This is possibly due to the additional effect imposed by the density of states in the electrodes and/or the formation of Schottky barriers at the edge of the tunnel barrier. The presence of pinholes would impose an additional (unobserved) linear contribution to the I-V characteristics at low bias corresponding to the resistance of this parasitic pathway.

- The barrier height in samples with AlN barriers increases with decreasing barrier thickness while the resistance remains high [13]. As the barrier thick-

[13] See Figure 4.19.

ness is decreased it is expected that the barrier height will eventually begin to decrease due to the co-existence of pinholes. Pinholes in the barrier will reduce the device resistance, and when fit with the Simmons model this would manifest as an anomalously low fitted barrier height/width.

- The magnetoresistance in these tunnel junctions increases at the lowest temperatures, as shown in Figure 4.16. In bulk GdN films the magnetoresistance is largest near T_C and then decreases at low temperatures. This contrast in the temperature dependent magnetoresistance must be due to tunnelling.

- The current density flowing through any pinhole(s) would be immense if they were the dominant transport pathway. In our devices the non-linear I-V curves point to a conduction mechanism dominated by tunnelling at high bias. It is necessary to examine the low current measurements in order to ascertain whether there is a parasitic resistance pathway in parallel to the tunnel junction caused by pinholes. A back of the envelope calculation based on known parameters can be used to estimate the current density flowing through any pinholes. For a resistance of $\sim 10^7$ Ωcm from a 10 nm thick GdN pillar of $\rho = 10\,\Omega\,\mathrm{cm}$ the area must be 10^{-12} cm^2 (this is equivalent to one 10 nm wide pinhole). The 10 nA current then has a density of 10000 Acm^{-2} within the pinhole. Provided that the pinhole could withstand such a high current density this would cause Joule heating of the pinhole, meaning that the active area of the device would be hotter than its surroundings. Joule heating of the pinhole should manifest as an apparent shift in T_C of the measured device, as the active conduction channel would be warmer than the thermometer used during the measurement. This is not observed and the resistivity peak, due to the GdN T_C, occurs at 50 K regardless of bias level.

For the conductive junctions with low barriers there is a much stronger temperature dependence of R(T) at low bias [14] which, along with a magnetoresistance that decreases near 5 K, could point towards pinholes in these samples. Indeed, in

[14] See Figure 4.22.

these conductive samples the I-V curves are linear at high temperatures [15] which is consistent with the co-existence of pinholes. As the device is cooled the pinhole resistance pathway is expected to become more resistive while the tunnel junction resistance remains relatively constant. This means that the tunnel junction (non-linear) component dominates at low temperatures while the pinhole component dominates at the highest temperatures. Therefore for those samples it is possible that a parallel conduction pathway through pinholes exists, while the resistive tunnel junctions show very different behaviour and pinholes are unlikely.

[15] As shown in Figure 4.21.

4.7 Summary

In summary, magnetic tunnel junctions fabricated using electrodes made from the intrinsic ferromagnetic semiconductor GdN have been demonstrated. The current-voltage characteristics are well described by a tunnelling model which gives a 1.5 eV barrier height at 300 K for devices with insulating GaN barriers. This puts the GdN Fermi level close to the middle of the GaN band gap, which is consistent with recent calculations of Kagawa *et al.* [100] who find the GdN Fermi level lies close to mid-gap for GaN. This was found to carry over to AlN barriers, which have fitted barrier heights up to ∼3 eV, again pointing towards the GdN Fermi level lying close to the middle of the AlN gap. A trend of decreasing barrier height with increasing AlN barrier width was also observed, perhaps signalling the existence of Schottky barriers at the barrier interface. The resistances of tunnel junctions with GaN and AlN barriers agree with the Simmons model, although the electronic density of states in the GdN electrodes also has a marked effect on the temperature dependent resistance of the tunnel junction, demonstrating a novel approach to controlling the properties of MTJs.

Given that these are large, polycrystalline tunnel junctions with multiple crystallites of similar coercive fields it is unsurprising that the magnetoresistance data at low temperatures did not show any clear signs of sharp switching events. In order to pursue enhanced magnetoresistive switching, there are several potential avenues of investigation. This includes decreasing the number of magnetic domains in the electrodes, either by decreasing the device size or by improving the crystallinity of the layers (or both). Another route to enhanced switching is to use layers with contrasting magnetic properties. The latter technique is commonly used in magnetic tunnel junctions where one layer is "pinned" by exchange and the other electrode is left free to switch. Layers having a large coercivity contrast can also be used to this end and one such system will be studied in the next chapter.

Chapter 5

Tunnel Junctions Incorporating SmN

5.1 Introduction

Alongside recent progress in tunnel junction research has come new discoveries on the interaction between electron spin and orbital motion, including much progress in understanding the anomalous and spin Hall effects [107, 108], and the recent development of spin orbitronics [109]. It has become clear that increased control of magnetisation dynamics can be obtained by incorporating orbital effects in addition to the usual spin contribution to the magnetism. Nonetheless, to date this has not extended to the use of spin-orbit coupled materials in the electrodes of magnetic tunnel junctions. Unlike the *3-d* and *4-d* magnetism in transition metal ions, the rare earths do not feature full orbital quenching so that the net moment includes both spin and orbital contributions. The total moment is then larger, smaller or even oriented antiparallel to the spin moment. The contrasting magnetic properties that result suggest promise in as-yet-unimagined applications.

This chapter will report novel tunnelling characteristics in magnetic tunnel junctions with electrodes made from two contrasting members of the series, GdN and SmN. GdN has occupied the role as prototypical rare-earth nitride, with much more work done on it than has been afforded any of the rest of the series. Gd lies

at the centre of the lanthanide series, and the trivalent Gd ion in GdN has an exactly half-filled *4-f* shell, with zero orbital angular momentum ($L = 0$), fully aligned spins ($S = 7/2$), and a magnetic moment of 7 μ_B residing purely in the spin component [110]. It thus resembles the spin-only magnetism that is also characteristic of transition-metal compounds. However, the spherically symmetric ($L = 0$) orbital function results in a small crystal anisotropy, with coercive fields as low as 10^{-2} T having been reported [24]. In contrast Sm^{3+} features (L, S) of $(5, 5/2)$, and due to the presence of a strong spin-orbit interaction the Hund's rule ground state has opposing spin and orbital alignment. This leads to a small magnetic moment of only 0.8 μ_B in the free ion [110]. That is further reduced by the crystal field and exchange interaction in SmN to yield a ferromagnetic moment of only 0.035 μ_B per formula unit [46,61]; to our knowledge this is the smallest ferromagnetic magnetization in any stoichiometric compound. That small moment results from an almost complete cancellation of spin and orbital contributions. Significantly it is the orbital moment which dominates weakly in SmN. Its net magnetization is then directed in opposition to the *4-f* spin magnetic moment, which will be seen below to have important consequences in GdN/AlN/SmN devices. The coercive field of SmN is larger than 6 T at low temperatures [46], resulting from a stronger crystal anisotropy and much weaker Zeeman interaction than in GdN, again with important consequences. The strong spin polarisation of the *4-f* shell in both GdN and SmN results in a large exchange splitting of the conduction band, such that doped charge carriers are expected to be highly spin polarised [1, 24].

5.2 Sample Preparation

GdN/AlN/SmN tunnelling structures were formed by photolithography in a cross-contact geometry, as shown schematically in Figure 5.1(a). A narrow (100 µm) gold contact strip was deposited onto a sapphire substrate and patterned using photolithography and a metal lift-off process. A second photolithography step was performed to define a 200 µm photoresist channel perpendicular to the Au strip. Gd was then deposited into the strip at 0.02−0.05 nm/s by vapour deposition under

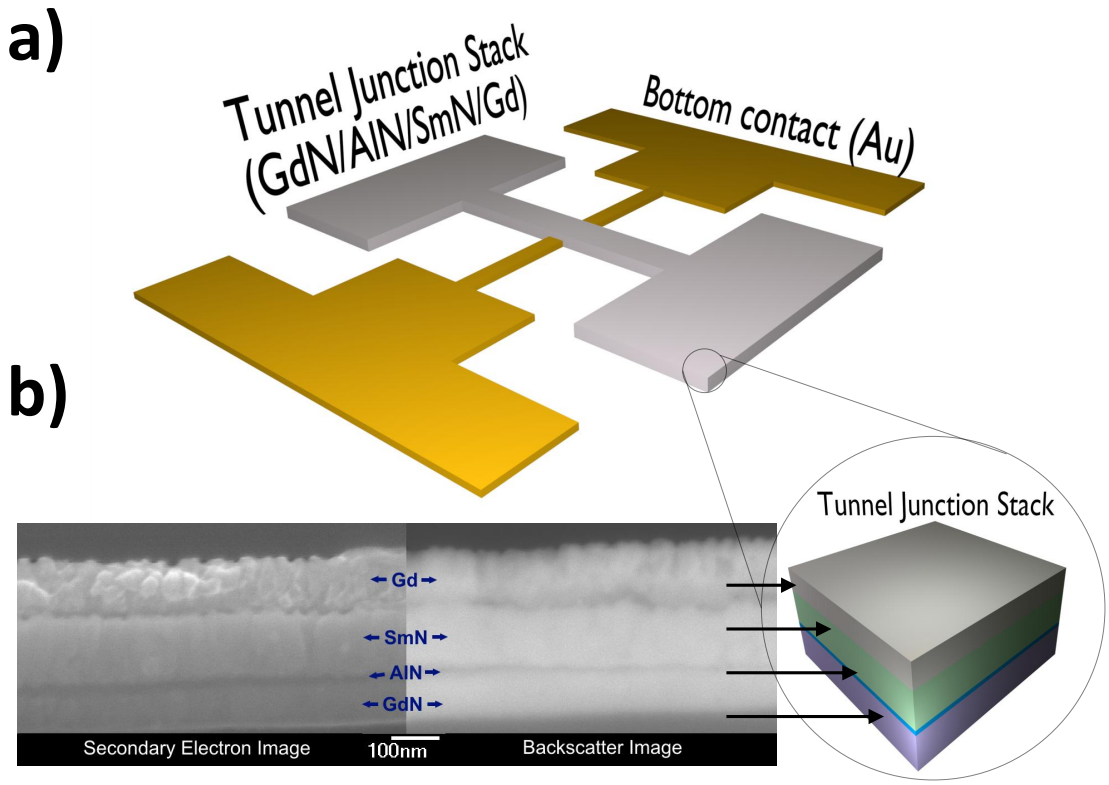

Figure 5.1 – (a) Schematic illustration of the entire magnetic tunnel junction geometry, where the "tunnel junction stack" is shown at lower right. The tunnel junction area is 100 µm×200 µm. (b) Cross-section SEM images of a GdN/AlN/SmN tunnel junction obtained by both backscatter and secondary electron imaging. The backscatter image highlights the AlN layer.

a nitrogen pressure of $1 - 10 \times 10^{-4}$ mbar, resulting in the formation of GdN. Al was deposited in the presence of activated nitrogen from a Kaufmann cell to grow the insulating AlN barriers followed by a SmN layer grown in the same manner as GdN. The structures were capped by Gd metal both to protect the structure from oxidation and to provide electrical contact to the top of the structure. After the growth of the tunnel junction and the Gd layer the photoresist was removed via a second lift-off process.

The typical SEM image of Fig. 5.1(b) shows that the insulating layer is thin-

ner than 5 nm, while all other layers are close to 100 nm thick. The device was deposited at ambient temperature, which results in GdN layers that are smooth and strongly (111) textured [30]. Ambient-temperature deposited SmN is much less strongly textured, and unsurprisingly it was not possible to prepare smooth structures showing clear tunnelling characteristics with SmN as the substrate for the AlN insulating barrier.

5.3 Results

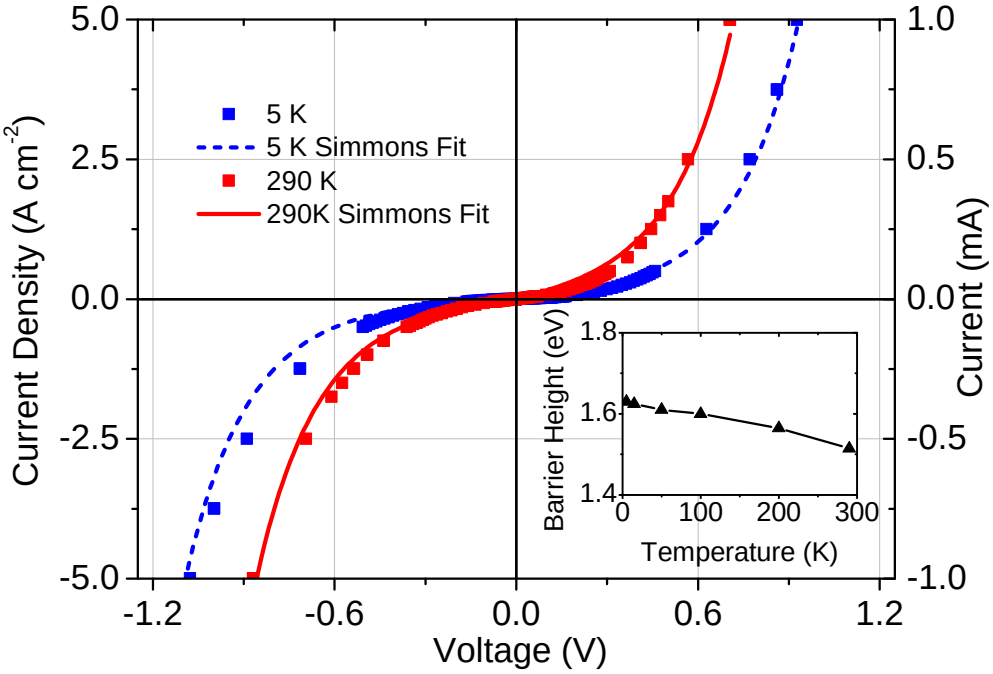

Figure 5.2 – Current-voltage characteristics for a SmN/AlN/GdN tunnel junction fitted using the Simmons tunnelling model. Inset: Modelled barrier height (average of forward and reverse current) plotted against temperature.

The current-voltage (IV) characteristics of a GdN/AlN/SmN tunnel junction shown in Figure 5.2 are well described by the Simmons square barrier model [92,95],

from which is extracted a barrier height of about 1.6 eV (see Fig. 5.2 inset) and a barrier width of 1.9 nm. This is consistent with the results of Chapter 4. In this instance it is found that the rare-earth nitride conduction bands lie slightly above the AlN mid-gap.

The strikingly unusual properties of the GdN/AlN/SmN tunnel junction are illustrated by the low temperature magnetoresistance data shown in Figure 5.3(a). The magnetoresistance is as large as 140% with the field in plane and nearly 200% with the field out of plane. It is important to note that the device resistance is largest at fields high enough to saturate the magnetisation of both layers, which is *opposite* to the behaviour of conventional tunnel junctions. As illustrated in Figure 5.4[1] the positive magnetoresistance is a direct result of the orbital dominant nature of the magnetism in SmN: at high fields it is the net, orbital dominant magnetic moment that aligns with the field, which then forces the spin magnetic moment to align opposite to the field. On the other hand the purely spin-based moment in GdN is aligned with the field, and thus high fields lead to opposite spin alignment across the tunnel barrier and in turn a high resistance. This novel behaviour is a clear demonstration that the device is operating in the tunnelling regime, with the very large magnetoresistance indicating strong spin polarisation in the rare-earth nitride electrodes. The magnetoresistance observed in GdN/I/GdN (I=GaN,AlN) control junctions shown in Figures 4.15 and 4.16 is negative, smaller, and shows no signs of the interesting features observed in the SmN system.

More unusual features are revealed in the magnetoresistance at lower fields. A pronounced dip occurs between 1 T and 4 T, with no evidence for hysteresis between upward and downward field sweeps. The lack of dependence on the field orientation of this feature implies it originates in changes in the magnetisation of the SmN electrode whose near vanishing moment leads to a very small shape anisotropy. Its appearance below 4 T is consistent with the magnitude of the coercive field expected for SmN [46, 61].

The region closer to zero field is expanded in Figs. 5.3(b)-(g), where large and reproducible changes are seen in the magnetoresistance that now depend on

[1] In Figure F.2 this is represented by an animation (see Appendix F).

the field orientation. With the field in the film plane the magnetoresistance shows strong maxima of over 140% either side of zero field. These are reminiscent of those that occur in conventional magnetic tunnel junctions when the spin orientation of the electrodes are in opposition [79], but crucially here the maxima occur on both the positive and negative side of zero field, independent of the direction of field sweep. The field-out-of-plane data show similar strong features, but at somewhat larger fields, and in this case the maxima are hysteretic. Most surprisingly the hysteresis is in the opposite sense to that conventionally expected, i.e., the maxima occur on decreasing field rather than increasing field, implying that one of the electrodes switches spin orientation before the field changes sign. All of the low field features are still present when the current is increased by an order of magnitude, although their magnitude is reduced substantially as expected in the tunnelling regime [Fig. 5.3(d)-(g)].

Figure 5.5 presents the temperature dependent resistance of the GdN/AlN/SmN tunnel junction. Under low current a clear feature is observed near the $\approx$50 K Curie temperature of the GdN electrodes, with an additional feature seen near the $\approx$30 K Curie temperature of SmN. These features are caused by exchange splitting of the energy bands as the rare-earth nitrides enter the ferromagnetic state [24, 30]. The resistance is several orders of magnitude larger than would be expected for SmN or GdN in the absence of a tunnel barrier [24], so clearly transport through the tunnel junction is dominated by the presence of the barrier layer. However, the presence of the exchange splitting features emphasise again that the density of states in the electrodes also has an important effect on the device characteristics. For larger applied currents, and hence voltages, the features are less noticeable because states further from the Fermi level are being probed. The separate resistance features associated with GdN and SmN show that these layers are magnetically decoupled.

The GdN/AlN/SmN magnetoresistance data are in marked contrast to the conventional behaviour of magnetic tunnel junctions, which are opposite in sign and do not show detailed structure as a function of field. Overall the data imply complicated switching of the spin orientations within the SmN and GdN electrodes,

with the lack of hysteresis in the majority of the magnetoresistance data showing that the switching is not simply a result of the bulk magnetisation reversals observed in isolated magnetic layers. A direct investigation of the magnetisation is clearly of interest but the vanishingly small SmN magnetic moment is entirely masked by the large GdN moment, so magnetisation measurements of these junctions are not useful. However, the GdN and SmN moments have been probed independently using x-ray magnetic circular dichroism both in coupled GdN/SmN bilayers and in heterostructures with an exchange-blocking insulating layer [17]. The results show quite clearly that uncoupled SmN and GdN layers the magnetisation switches just as in homogeneous films of the two materials. Furthermore an exchange-Zeeman conflict led to an easily understood spin-twisted pattern in SmN that was exchange-coupled to GdN, which influences the intermediate-field behaviour of the tunnelling structure in the present study. The twisted magnetisation phase rotates as a function of distance from the interface, similar to an exchange spring. The small magnetic moment of SmN, and the corresponding weak Zeeman interaction, yield a length scale for the rotation of several tens of nanometres in fields of order 1 T. It is likely that such a twisted phase forms in the SmN layer of the MTJ described here, where the interface pinning comes from the top Gd electrode that is in direct contact with the SmN. A twisted phase propagating through the SmN to the tunnel barrier with a length scale that decreases with increasing applied field then leads to the intermediate field oscillations observed in the magnetoresistance.

The features at low magnetic fields likely originate from complicated magnetisation dynamics. Given the large shape anisotropy of GdN, and the small shape anisotropy of SmN, the contrasting data measured with the field in and out of plane points to the GdN layer being responsible for these features. Observations in a similar ferromagnetic semiconductor system, (Ga,Mn)As, attribute the spontaneous magnetisation reversal to the large ratio between anisotropy and coercive fields. With the field out of plane, even a small in-plane component can result in the magnetisation switching between in-plane easy directions. [111] It is worth noting that the peaks close to zero field decrease with increasing temperature and

current. This is typical of magnetic tunnel junctions where the TMR decreases as the temperature increases due to magnetic disorder and thermally assisted tunnelling [112]. It is not clear what role, if any, spin-transfer torque might play in the magnetisation dynamics of these devices, and this is worthy of future investigation. The strong spin-orbit coupling in SmN may be beneficial to a device based on current-controlled switching.

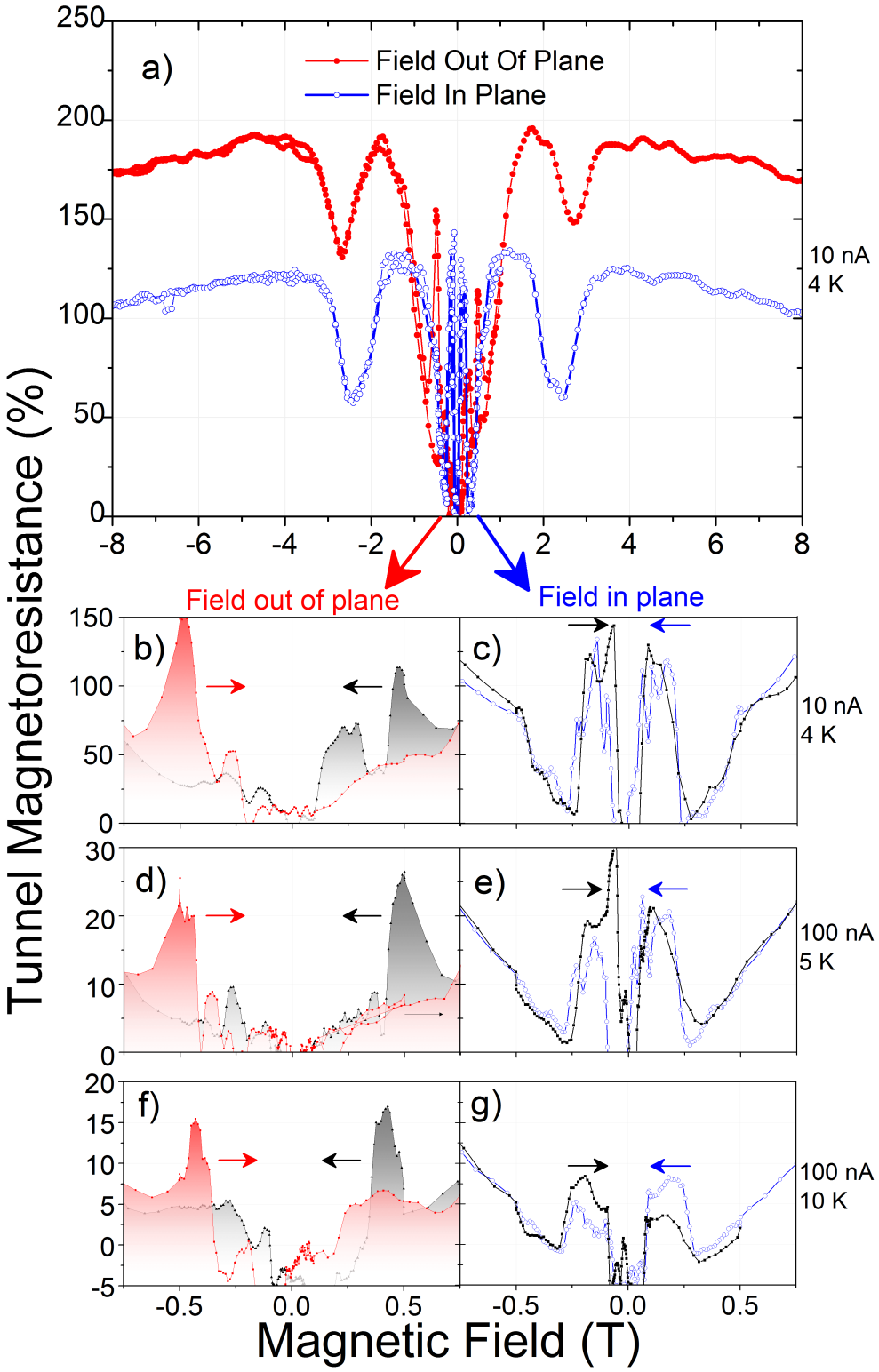

Figure 5.3 – (a) Magnetoresistance data from a GdN/AlN/SmN tunnel junction obtained from −8 T to 8 T at 4 K in both the in-plane and out-of-plane orientations with a measurement current of 10 nA. (b-g) Tunnel magnetoresistance data at low fields measured both in increasing and decreasing fields using different currents and temperatures.

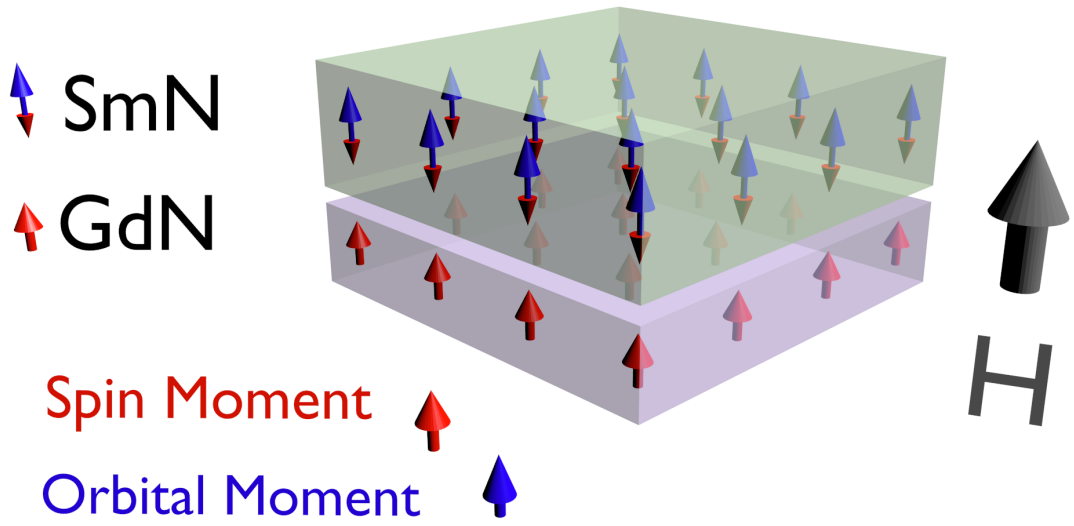

Figure 5.4 – Schematic diagram of the spin and orbital parts of the magnetic moments when the tunnel junction is in the high resistance state in a large applied field. For SmN the magnetic moment is dominated by the orbital contribution, so the spin moment aligns opposite to the field.

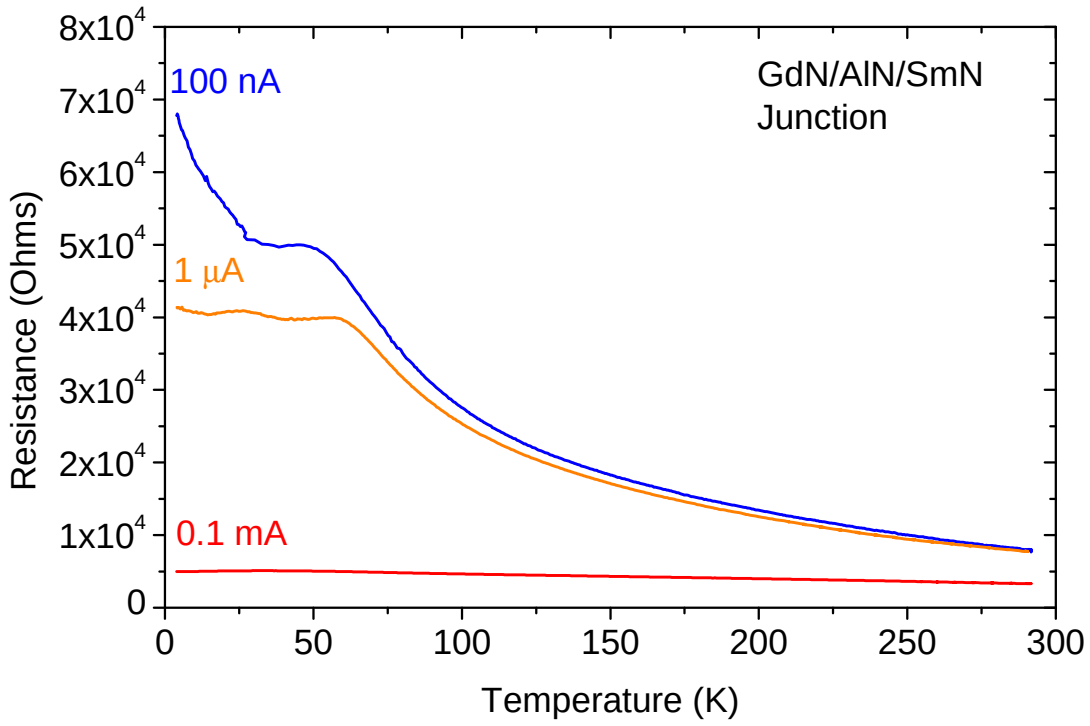

Figure 5.5 – Temperature dependent resistance of a GdN/AlN/SmN tunnel junction, measured using various applied currents.

5.4 Summary

In summary, the data presented here for a magnetic tunnel junction incorporating a near-zero-moment ferromagnet demonstrate the possibility of bringing new functionality to these devices by exploiting novel spin and orbital magnetic properties in the electrodes. An exceptionally large magnetoresistance for a polycrystalline tunnel junction is found, indicative of strong spin polarisation in the electrodes. The positive sign of the magnetoresistance is a direct result of the use of the orbital-dominant ferromagnet SmN as an electrode material. This zero-moment ferromagnet also leads to unusual field-dependent structure in the magnetoresistance data. The spintronics potential of moment-free ferromagnets has recently been highlighted also in a half-metallic Heusler system [64, 65], where the moment cancellation comes from two competing spin contributions rather than competing spin and orbital moments. Investigating the similarities and differences in devices based on the two types of zero moment systems promises to provide much insight into their physics.

5.5 Towards Epitaxial Devices

Epitaxial devices are expected to show improved switching and better interfacial quality, possibly resulting in even larger tunnel magnetoresistance values. Preliminary investigations into producing these was conducted in collaboration with CRHEA/CNRS. Epitaxial tunnel junction stacks were grown on silicon doped GaN, which provides both a conductive and epitaxially compatible layer onto which the rare-earth nitrides can be deposited. The as-grown stack was then processed into mesa structures in a top-down configuration, in contrast to the bottom-up configuration used in the cross-contact geometry. It was found that these could be wet etched using dilute hydrochloric acid for samples prepared using ammonia as the nitrogen precursor. In contrast, samples prepared using nitrogen gas were rapidly corroded, perhaps signalling that the ammonia passivated hydrogen sites. For future processing of films, a dry ion-milling process is preferable to mitigate these technical challenges and reduce exposure to aqueous solutions. Once patterned

into mesa structures, making reliable contact to these devices for low temperature measurements was problematic, and remains an ongoing topic of investigation.

Chapter 6

Mg Doped GdN

6.1 Introduction

Control of the electronic charge concentration is an important aspect of semiconductors and is crucial for many device applications. By introducing a small concentration of impurities into a semiconductor it is possible to dope the sample with electrons or holes. Given that the atomic density is much greater than the mobile charge density these impurity atoms need not change the global crystallographic properties of the material.

Because Gd is trivalent and Mg divalent, the possibility exists of using Mg as a p-type substitutional dopant in GdN. By changing the charge density, or even by p-type doping GdN, a greater understanding of the role of the charge carriers on the other properties such as the magnetism can be obtained. P-type doping would represent a large step toward the integration of rare-earth nitrides into spintronics devices through the formation of P-N junctions. Mg doping has been demonstrated in GaN which [113], like GdN, is easy to dope n-type by the formation of nitrogen vacancies but difficult to dope p-type. In this chapter results are presented from a study of magnesium-doped GdN films.

The films used in this study have been prepared in collaboration with CRHEA/CNRS and are epitaxial GdN grown on an AlN crystallographic template, capped with GaN to prevent oxidation. The GdN layers grown here differ slightly from

Sample	Mg Cell Temperature (°C)
A	0
B	180
C	220
D	200
E	253

Table 6.1 – Magnesium effusion cell temperatures for the samples A-E.

those prepared at VUW (see Section 3.1) in that ammonia is used as a nitrogen precursor instead of nitrogen gas. Gd metal is evaporated from an effusion cell onto a heated substrate (650 °C) under a flux of ammonia. A second effusion cell containing Mg is used to provide a small flux of Mg atoms for doping. All samples were grown on 100 nm AlN buffer layers on Si (111) and capped with GaN. It was observed that Mg evaporated during the growth coats the chamber, and care must be taken during subsequent depositions as Mg re-evaporation may occur when Mg coated surfaces are heated.

The samples A-E were grown with differing Mg effusion cell temperatures as described in Table 6.1.

6.2 Results

6.2.1 XRD

XRD patterns from the films are displayed in Figure 6.1, revealing a strong GdN (111) peak in every sample with no sign of any crystalline Mg phase [1]. These scans have been angle-corrected using the AlN (0002) peak at 36.1° as a reference [114]. There is no systematic variation in either the GdN (111) peak angle (lattice constant) or linewidth (crystalline quality) with Mg concentration. Peaks

[1] These measurements were performed by Franck Natali at CRHEA-CNRS.

close to 28 and 34 degrees are also visible, which are due to the Si substrate and GaN cap, respectively [115]. Rocking curve measurements of the GdN (111) peak, shown in Figure 6.2, to probe the crystalline quality further yield no obvious trend with Mg concentration (see inset to Fig. 6.2). This is an indication that the Mg is being integrated into the lattice as a substitutional impurity atom resulting in no significant strain or degradation in crystalline quality.

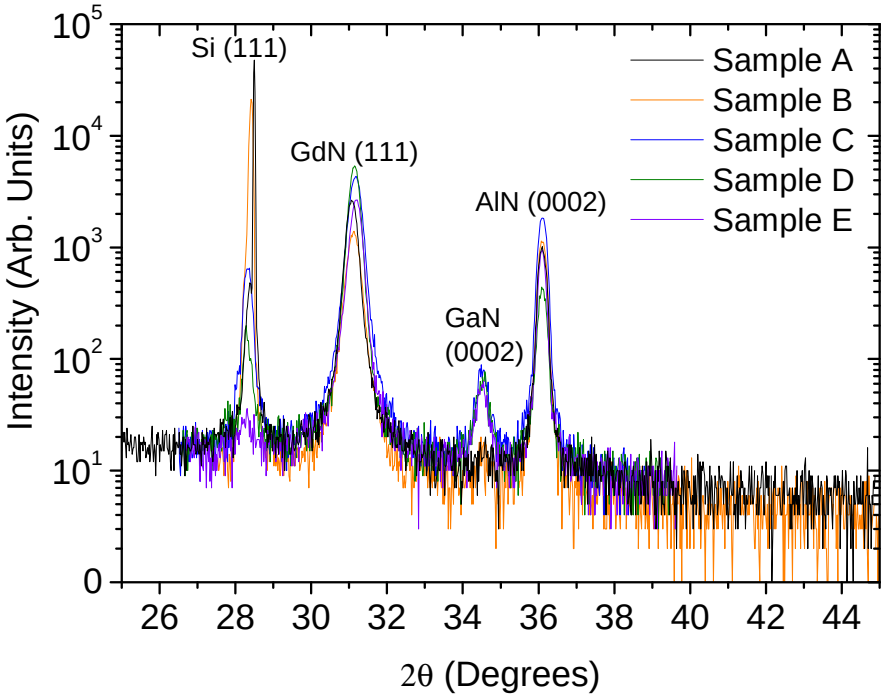

Figure 6.1 – $\theta - 2\theta$ XRD patterns from the Mg doped GdN samples A-E.

6.2.2 Electron Microscopy

Scanning electron microscopy was employed in order to visually examine the thickness and homogeneity of the layers. A typical image of one of the films is included in Figure 6.3, from which it is found that the Mg:GdN layers are smooth and ∼140 nm thick.

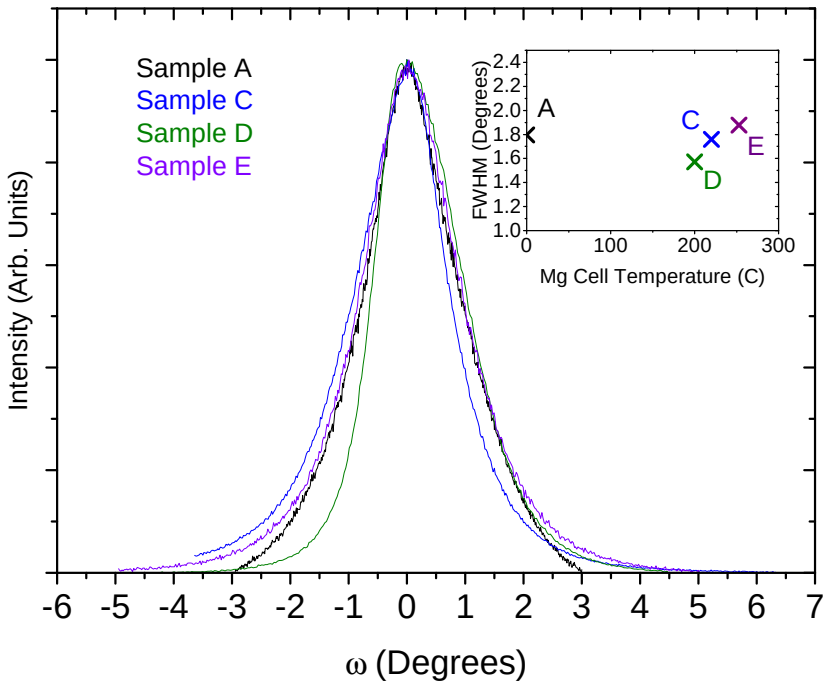

Figure 6.2 – Rocking curve XRD measurements of Mg:GdN samples.

Spatially resolved Energy-Dispersive X-ray Spectroscopy (EDS) measurements of a Mg doped sample suggest a uniform dispersion of Mg within the film. This is shown in Figure 6.4 where EDS images of the films are shown probing a variety of different x-ray energies. Starting from the top left and working right and then down:

1. The topology image shows the three layer (AlN/Mg:GdN/GaN) on a silicon substrate. This is obtained in the backscatter configuration.

2. A Gd L-edge image highlights the Gd atoms present within the GdN layer.

3. A Ga K-edge image reveals the Ga atoms present within the capping layer atop the film.

4. The Mg-K edge image shows that there are Mg layers present within the

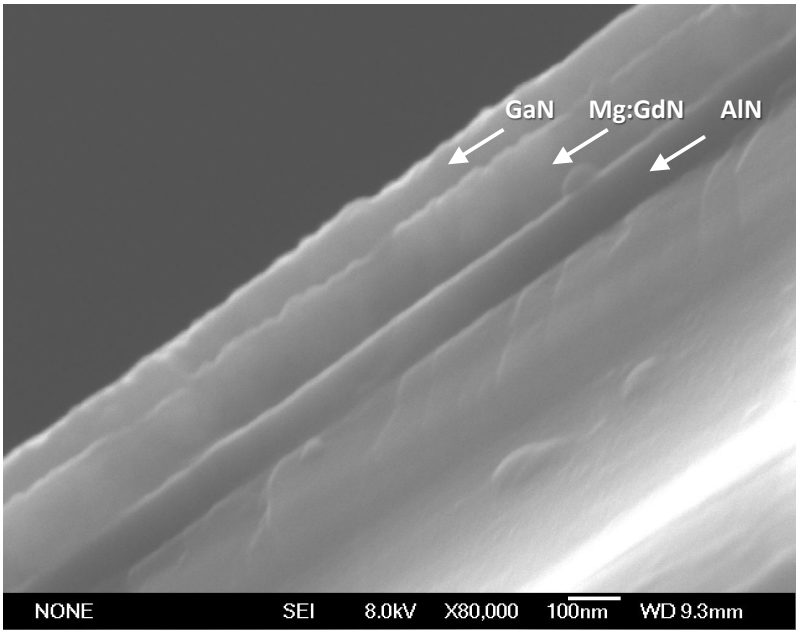

Figure 6.3 – Scanning electron microscope image of a Mg:GdN film obtained in the SEI configuration.

GdN layer, and that these Mg atoms are dispersed evenly. This lends further evidence to suggest that Mg atoms are uniformly incorporated into the GdN, as opposed to forming Mg clusters.

5. The nitrogen K-edge image shows the nitrogen present in the nitride layers.

6. A Si K-edge image clearly shows the silicon substrate.

The XRD and SEM structural characterisation results support the growth of epitaxial GdN layers incorporating uniformly dispersed Mg impurity atoms.

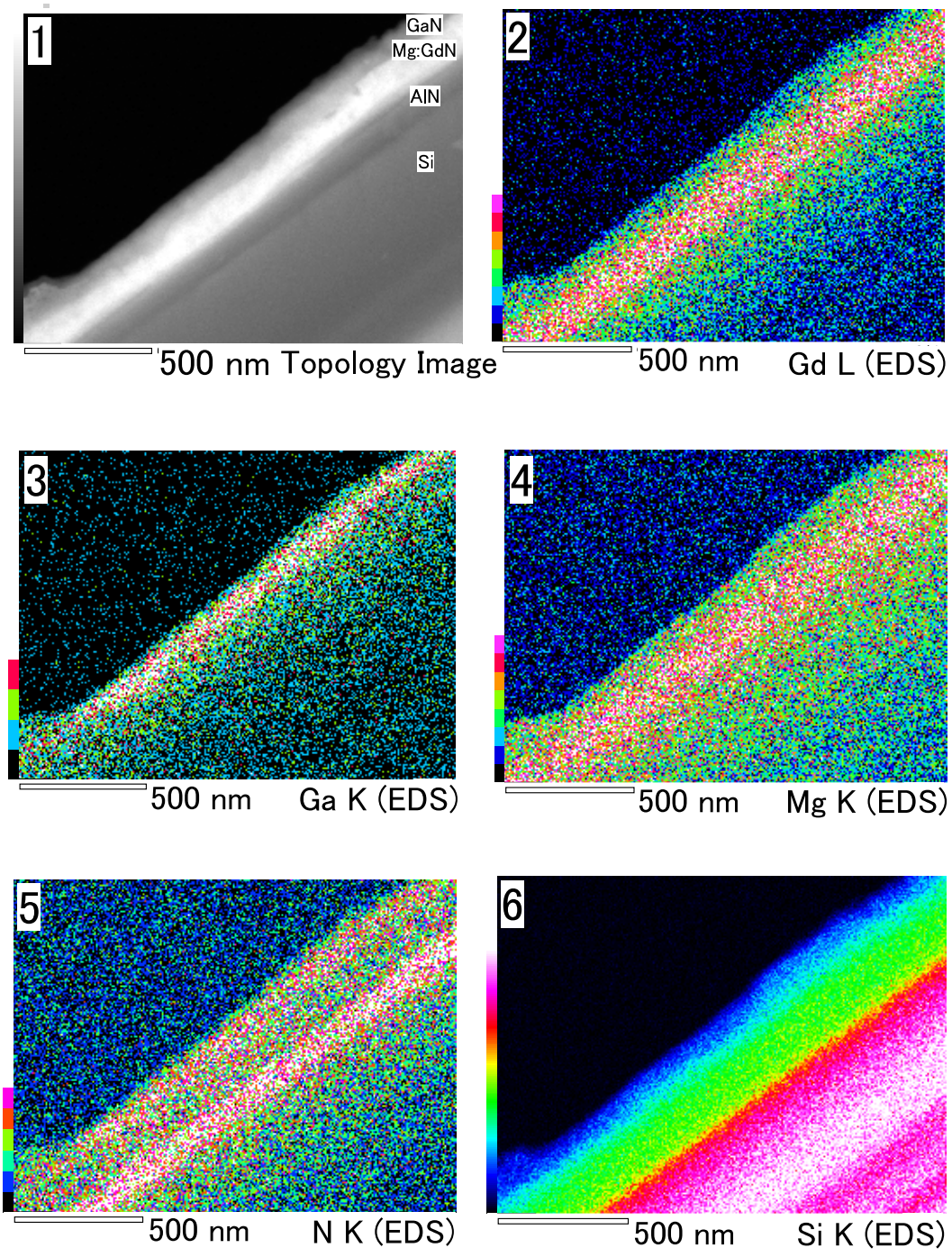

Figure 6.4 – Scanning electron microscope images of a Mg:GdN film obtained in the EDS configuration. The different images show the topology (subplot 1), and the spatially resolved x-ray edges from Gd, Ga, Mg, N and Si (subplots 2-6).

6.2.3 Temperature Dependent Resistivity

The temperature dependent resistivity of three Mg:GdN films was measured in the van der Pauw geometry as described in Section 3.3.1. The results of these measurements are displayed in Figure 6.5. There is a clear peak near 60 K in the resistivity of these samples, corresponding to the onset of ferromagnetism in the GdN. The resistivity increases from $\sim$2 mΩ cm for an undoped film to $\sim$100 Ω cm for the most heavily Mg doped of the samples. This increase in resistivity with magnesium doping is strong evidence to suggest that the Mg is acting to passivate free carriers introduced through nitrogen vacancies. Alongside the increase in resistivity, there is a change of sign of the TCR close to room temperature. The TCR between 150 and 300 K changes from positive to negative as the doping level is increased, consistent with depletion of carriers in the GdN conduction band. There also appears to be a slight shift in the peak to lower temperatures as the doping level is increased, which has been investigated further in Section 6.2.5 using magnetometry measurements.

6.2.4 Hall Effect Measurements

Room temperature Hall effect measurements were performed in the van der Pauw configuration on an expanded set of samples subsequent to this study [3]. The results of these measurements are shown in Figure 6.6 which plots the resistivity against the measured carrier concentration. There is a clear trend of decreasing carrier concentration and increasing resistivity. Which is consistent with the resistivity results above. The reduction in carrier concentration with increasing Mg doping suggests that the Mg atoms are acting as electron acceptors when substitutionally doped onto the Gd sites in GdN.

6.2.5 Magnetic Measurements

To further investigate the apparent change in T_C observed in temperature dependent resistivity measurements, magnetisation measurements as a function of temperature were performed. This used a SQUID magnetometer, the results from

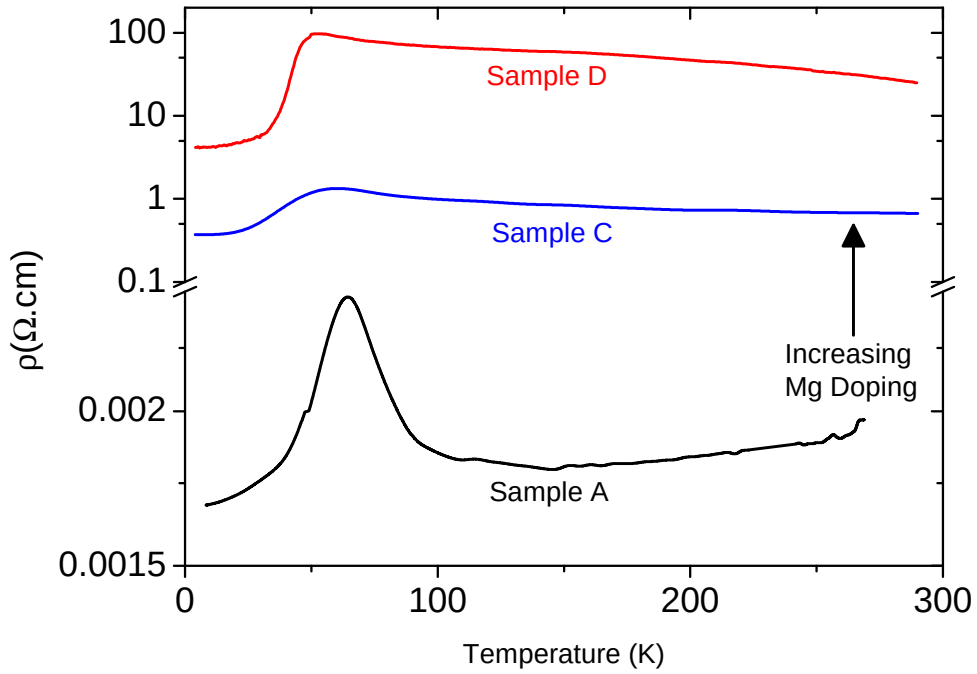

Figure 6.5 – Temperature dependent resistivity measurements of three Mg:GdN samples. From lowest to highest resistivity these are: undoped (Sample A), intermediately Mg doped (Sample C) and heavily Mg doped (sample D).

which are displayed in Figure 6.7 for three samples of different Mg doping concentrations. The magnetic moments in these samples have been normalised to the maximum (low temperature) value so that they can be more readily compared. It is apparent that in the case of the undoped sample there is an onset of magnetic ordering at ∼70 K corresponding to the Curie temperature. For this sample an inverse susceptibility plot in Figure 6.8 reveals a T_C of ∼70 K. As the magnesium doping level is increased there is a clear second transition observed at ∼45 K which becomes stronger as the doping level is increased. An inverse susceptibility plot is insufficient in this instance for quantitatively finding the T_C of multiple magnetic transitions. Lee *et al.* investigate this further for the Mg doped GdN samples shown here (along with other samples) using Arrott plots to find that the

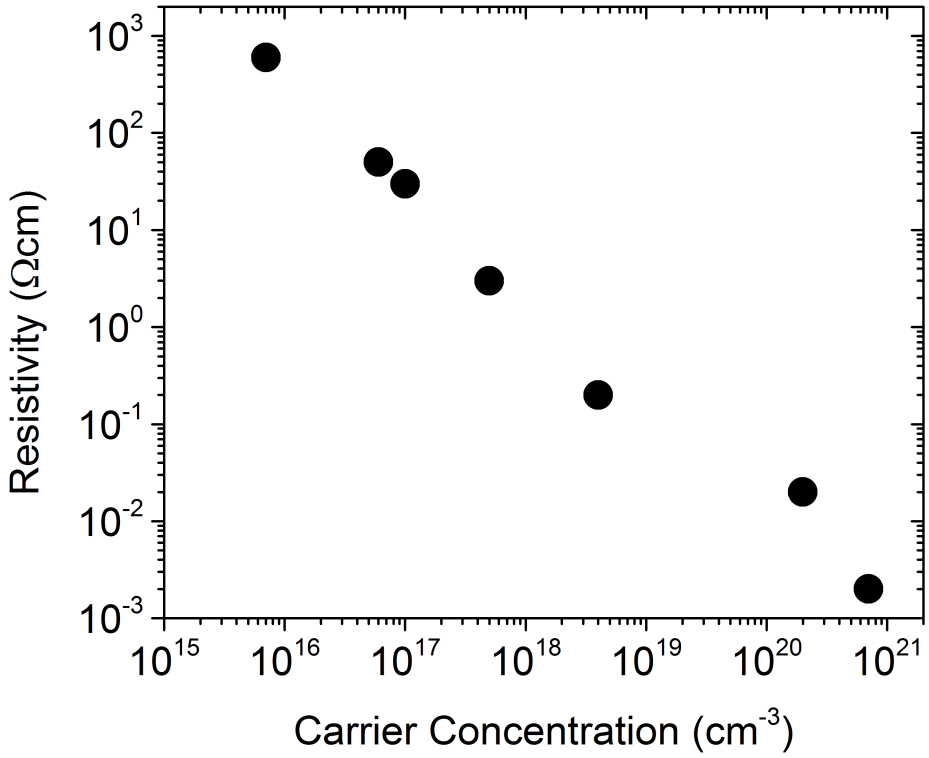

Figure 6.6 – Mg:GdN room temperature resistivity plotted against the carrier concentration measured via the Hall effect. Note that this figure contains an expanded set of samples, extending the results presented elsewhere in this chapter. Figure reproduced from Lee *et al.* [3].

transition lies close to 50 K [3].

The reduction of T_C from 70 K to 50 K as carriers are removed is consistent with a recent magnetic polaron model proposed by Natali *et al.* in GdN [60]. In this model the exchange between Gd^{3+} ions is enhanced by the presence of electrons donated from nitrogen vacancies which form an energy level close to the CB minimum[2]. This energy level becomes filled as the temperature is decreased

[2]Punya *et al.* calculate the binding energy of nitrogen vacancies. In their model each vacancy binds two electrons in a singlet state, with a third electron weakly bound to the other two in an

and carriers are frozen out of the conduction band, giving each of the vacancies a magnetic moment of 1 μ_B and providing a localised density of electrons which can mediate the magnetic exchange between Gd^{3+} ions. This idea of exchange mediated by weakly bound donor levels forms the basis of the magnetic polaron model [117]. The fact that in the present Mg:GdN samples the size of the transition between 50 and 70 K increases with carrier concentration supports this model, lending strong evidence to an impurity mediated exchange mechanism which increases T_C from 50 to 70 K in slightly nitrogen deficient GdN.

An inset to Figure 6.8 plots the coercive field of these three samples as a function of magnesium cell temperature. A slight decrease in the coercive field from $\sim$ 150 to $\sim$ 100 Oe with increasing Mg doping is observed. The coercive field of GdN depends partly on the crystalline quality [26]. Because no increase in the coercive field is observed upon incorporation of Mg, this is another confirmation that the crystalline quality is not impaired by Mg doping.

extended orbit [116]. The calculated binding energy of this weakly bound electron puts it close to the conduction band minima. These weakly bound electrons dope the GdN conduction band and enhance the exchange interactions between Gd atoms.

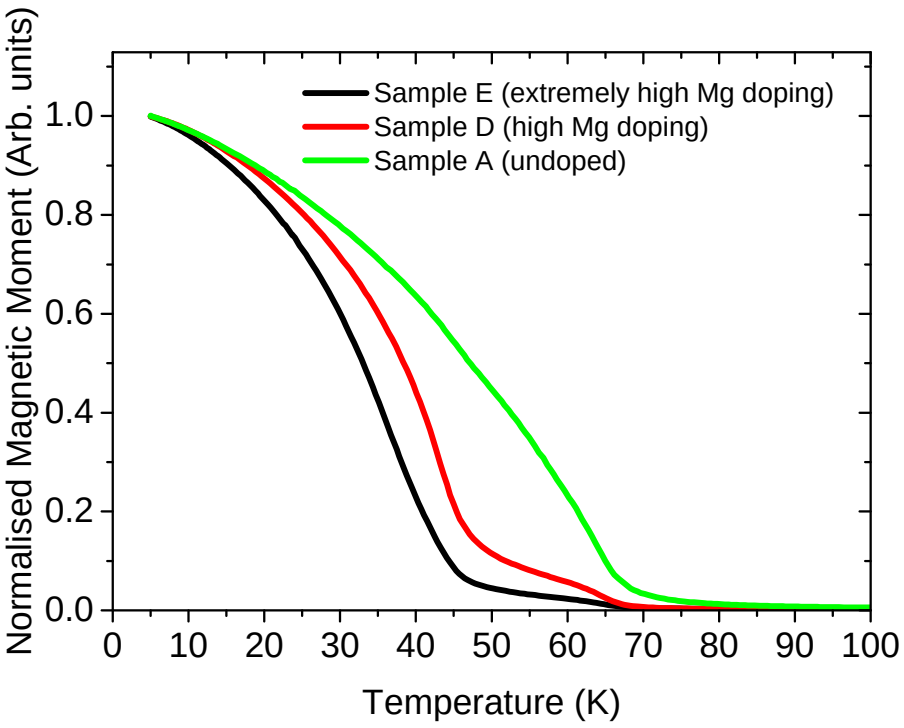

Figure 6.7 – Temperature dependent magnetisation measurements for Mg samples of different doping levels. These measurements were performed using the RSO measurement mode, field cooled at 250 Oe.

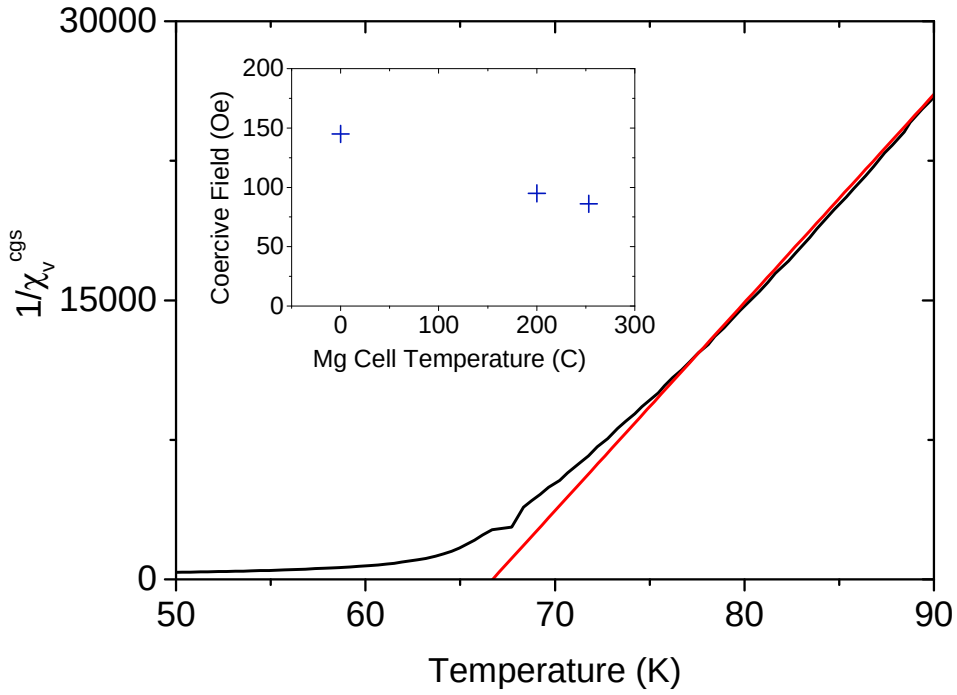

Figure 6.8 – Inverse susceptibility plot of the undoped sample. Here T_C is found to be 67±1 K. Inset: Coercive field of samples A, D, and E plotted against Mg cell temperature.

6.3 Summary

Overall, the results show that Mg doping of GdN results in a lower carrier concentration and correspondingly higher resistivity. The magnetic properties of the GdN are altered in a way consistent with the magnetic polaron model where the Curie temperature decreases from ∼70 K to ∼50 K as the carrier concentration is reduced. Given the low formation energy of nitrogen vacancies, the high temperatures used to prepare epitaxial samples result in films which are nitrogen deficient and carrier rich. If in future the growth conditions can be optimised to avoid this, or if films can be annealed post-growth to fill these vacancies, then there should be an even more pronounced effect resulting from Mg doping. In the present case, the Mg acceptors must first overcome the already high electron concentration. If these nitrogen vacancies can be filled alongside the Mg doping, it may be possible to dope GdN films p-type in future.

The results presented in this chapter were incorporated into a larger study using additional samples which confirm the results presented here [118]. A further study of this expanded sample set also revealed that there were two different contributions to the time-dependent photoconductivity decay in Mg:GdN films [119], an initial fast decay followed by a slow persistent photoconductivity. The results of this study suggest that Mg impurities in epitaxial GdN thin films act as acceptor-like centres, and incorporation of Mg results in a significant decrease of the density of nitrogen vacancies. Magnesium doping of GdN offers promise in future device applications. Although it has not yet been possible to p-type dope with Mg, p-type doping would open the door to devices such as spin-polarised diodes, transistors and other such devices built on p-n junctions.

Chapter 7

Conclusions

In this thesis, methods have been demonstrated allowing for the fabrication of novel rare-earth nitride devices in the vertical transport orientation. The rare-earth nitrides are sensitive to oxidation, and for this reason a bottom-up growth method was developed to avoid exposure to solvents. The rare-earth nitride layers were grown into a thin channel defined by photoresist, perpendicular to a thin bottom contact. This cross-contact geometry that has been developed allows for devices to be produced in the vertical transport orientation. Using this new device architecture there has been a focus on polycrystalline magnetic tunnel junctions incorporating GaN and AlN barriers. Upon inclusion of these barriers a highly resistive tunnel junction with strongly non-linear current-voltage characteristics is obtained. The I-V characteristics of devices with GdN electrodes have been examined using the tunnelling model of Simmons and from this barrier heights have been extracted of $\sim$1.5 and $\sim$3 eV for GaN and AlN, respectively. This permits an estimation of the band offsets, which puts the GdN conduction band slightly above the middle of the group-III nitride mid-gap, in line with recent theoretical calculations. These devices with GdN electrodes showed no signs of homogeneous switching, likely owing to the large size and correspondingly large number of magnetic domains with similar coercivities. To pursue switching, devices were fabricated replacing one of the electrodes with SmN, which has contrasting magnetic properties to GdN. In these GdN/AlN/SmN systems a large ($\sim$200%) positive magnetore-

sistance at high field was observed. This large positive magnetoresistance is due to the novel, orbital dominant magnetism within the SmN. At intermediate fields features were observed in the magnetoresistance consistent with the existence of a twisted magnetisation phase. At low fields homogeneous switching (hysteretic) events with TMR values of over ∼140% were observed. The size of the magnetoresistance is extremely large given the polycrystalline nature of the electrodes. This suggests a large spin polarisation within the rare earth nitride electrodes. These devices highlight the novel and contrasting magnetic properties of the rare-earth nitrides which may have much more to offer spintronic, and even spin-orbitronic devices in future.

One key benefit of semiconductors when applied to spintronics is that their properties can be tuned in various ways, such as engineering their carrier concentrations. One such method is through doping by the intentional inclusion of impurity atoms. By reducing the carrier concentration, Mg doping of GdN was observed to both increase the resistivity, and alter the nature of the ferromagnetic transition at T_C. This change in the magnetic properties near T_C is consistent with a recent model of magnetic polarons in GdN.

7.1 Suggested Future Work

With proof of concept REN magnetic tunnel junctions achieved, there are several obvious ways that both this new device architecture and other types of devices can be further explored.

The samarium and gadolinium nitride devices demonstrated in this thesis have exhibited interesting magnetoresistive properties. This could be investigated further and expanded on in a number of different ways including:

- The use of a non-magnetic top contact, this will establish whether there is a twisted magnetisation phase originating from the top Gd contact. The origin of the numerous features observed in GdN/AlN/SmN/Gd tunnel junctions could then be further isolated.

- Growing a series of tunnel junctions while varying the SmN layer thickness would also help in understanding the extent of the twisted magnetic phase.

- Superconducting contacts. There are several reasons that superconducting contacts might be interesting. Firstly, the contact resistance would go to zero, meaning that low resistance devices (without a barrier) could be investigated. For thin rare-earth nitride layers Josephson junctions could also be examined using many of the rare earth nitrides not already examined in other studies [12–14]. SmN is an interesting type of ferromagnetic superconductor when prepared correctly, and it may be fruitful to examine SmN when interfaced with different types of superconductors.

- Different devices sizes and geometries could be examined, requiring further development of the fabrication protocols. A top down fabrication method should be developed, particularly for epitaxial films. For top down fabrication, dry ion milling should be investigated in order to avoid the runaway etching problems experienced with samples prepared using N_2.

- The use of different members of the REN series begs further study. Like SmN, many of the rare-earth nitrides exhibit orbital dominant magnetism but without a negligible moment. It would be interesting to observe how these materials behave when incorporated into tunnelling structures.

- Different barrier materials should be investigated to assess both how the barrier material may result in spin filtering, and to examine the effects of changing the barrier height.

- The effect of spin-transfer torque on these devices should also be examined. Spin-transfer torque may be assisted by the large spin-orbit coupling and small magnetic moment offered by SmN. Investigating this will likely require a much smaller device area.

- Epitaxial devices may provide enhanced switching due to improved crystalline quality, and offer an interface which may result in a greater spin-polarisation of tunnelling electrons. Some progress towards this has been

made however the processing of these devices remains an open topic of investigation.

There are also other types of devices which should be investigated using the RENs including:

- Datta Das transistors could benefit by using SmN as an impedance-matched fringe-field free ferromagnetic semiconducting electrode. Many of the impedance matching problems experienced to date relate to the use of ferromagnetic metals, which may be avoided through use of a ferromagnetic semiconductor. The lack of fringe-fields offered by SmN will enhance the phase purity of the electrons as they migrate away from the edge of the electrode.

- Spin field effect transistors may be developed using Mg doped GdN as the channel. Field control of the carrier concentration in polycrystalline films has already been demonstrated in GdN [16]. In a film prepared with a lowered carrier concentration (using Mg), the field control could be enhanced in order to produce a device with a large on/off ratio. In this case the current being field modulated would be strongly spin polarised by virtue of the GdN.

- Spin oscillators exploiting the near-zero moment of SmN should be examined as the near zero moment may allow for the production of high frequency nano-oscillators.

These investigations will likely yield both interesting spintronic devices, and will provide a greater understanding of the properties of the rare-earth nitrides used in their construction.

Appendix A

Sequences for the Closed-Cycle Cryostat

The LabVIEW program used to perform measurements with the closed-cycle cryostat requires an input file known as a "sequence". This sequence defines the measurement routine which will be performed by the various pieces of equipment connected to the GPIB controller. There are several columns which set various parameters, and then there are rows which define the successive measurement iterations which are conducted as the preceding measurement is completed. The columns are as follows:

1. *row*. This column is used for indexing purposes.

2. *current* Measurement current used (in amps).

3. *task*. This tells the user what the system is doing, it does not in itself change any of the measurement settings.

4. *help*. This is what sets the type of measurement to be performed, be it a temperature scan or measurement at a fixed temperature.

5. *temp1*. This sets the final temperature used for a scan, for fixed temperature measurements this is the temperature which the cryostat will maintain for the duration of the measurement.

6. *temp2*. This is not used, in principal this can be used with the secondary thermocouple.

7. *step*. For temperature dependent measurements this is not required and is not used.

8. *ramp rate*. For temperature sweeps this sets the rate at which the cryostat is warmed/cooled. This must be kept below 3 K/min if thermal equilibrium is required otherwise a temperature gradient within the cryostat will build up and the sample temperature will not be accurately described by the thermocouple reading.

An example sequence for measuring temperature dependent resistivity is included below:

row	current	task	help	temp1	temp2	step	time	ramp rate
1	5.00E-05	Scan to 4.0K at 0.8K per minute	3	4	0	0	0	0.8
2	5.00E-05	Measure at minimum for 15.0 minutes	5	0	0	0	15	0
3	5.00E-05	Scan to 290.0K at 0.8K per minute	3	290	0	0	0	0.8
4	5.00E-05	Measure for 30.0 minutes	4	0	0	0	30	0
5	5.00E-05	Scan to 4.0K at 1.2K per minute	3	4	0	0	0	1.2
6	5.00E-05	Measure at minimum for 15.0 minutes	5	0	0	0	15	0
3	5.00E-05	Scan to 290.0K at 0.8K per minute	3	290	0	0	0	0.8
4	5.00E-05	Measure for 30.0 minutes	4	0	0	0	30	0
7	5.00E-05	Stop	7	0	0	0	0	0

The sequence for performing current-voltage measurements is somewhat more convoluted, as a new measurement is conducted for each desired current. Here the "..." represent parts of the sequence omitted for brevity. The sequence is set up to perform measurements at many different currents while holding the temperature constant, the sample is then heated or cooled to the next temperature and another set of current-voltage data obtained. Typically at the end of each sequence the sample is also repeatedly warmed and cooled with different applied currents. Each measurement can be performed for a different amount of time, in this example it is 0.1 minutes for the different currents, some of the samples exhibited a transient response which made it necessary to increase the measurement time in order to allow for transient effects to subside at each current.

row	current	task	help	temp1	temp2	step	time	ramp rate
1	1.00E-06	Scan to 290.0K at 0.8K per minute	3	290	0	0	0	0.8
2	5.00E-09	Measure for 0.1 minutes	4	290	0	0	0.1	0
3	1.00E-08	Measure for 0.1 minutes	4	290	0	0	0.1	0
4	1.50E-08	Measure for 0.1 minutes	4	290	0	0	0.1	0
5	2.00E-08	Measure for 0.1 minutes	4	290	0	0	0.1	0
6	2.50E-08	Measure for 0.1 minutes	4	290	0	0	0.1	0
7	3.00E-08	Measure for 0.1 minutes	4	290	0	0	0.1	0
8	...	...	...	...	...	...	...	...
99	1.00E-06	Scan to 100.0K at 0.8K per minute	3	100	0	0	0	0.8
100	5.00E-09	Measure for 0.1 minutes	4	100	0	0	0.1	0
101	1.00E-08	Measure for 0.1 minutes	4	100	0	0	0.1	0
102	1.50E-08	Measure for 0.1 minutes	4	100	0	0	0.1	0
103	2.00E-08	Measure for 0.1 minutes	4	100	0	0	0.1	0
104	...	...	...	...	...	...	...	...
105	3.00E-08	Measure for 0.1 minutes	4	100	0	0	0.1	0
106	3.50E-08	Measure for 0.1 minutes	4	100	0	0	0.1	0
107	4.00E-08	Measure for 0.1 minutes	4	100	0	0	0.1	0
108	...	...	...	...	...	...	...	...
295	1.00E-06	Scan to 5.0K at 0.8K per minute	3	5	0	0	0	0.8
296	5.00E-09	Measure for 0.1 minutes	4	5	0	0	0.1	0
297	1.00E-08	Measure for 0.1 minutes	4	5	0	0	0.1	0
298	1.50E-08	Measure for 0.1 minutes	4	5	0	0	0.1	0
299	2.00E-08	Measure for 0.1 minutes	4	5	0	0	0.1	0
300	2.50E-08	Measure for 0.1 minutes	4	5	0	0	0.1	0
301	3.00E-08	Measure for 0.1 minutes	4	5	0	0	0.1	0
302	...	...	...	...	...	...	...	...
392	9.50E-04	Measure for 0.1 minutes	4	5	0	0	0.1	0
393	1.00E-06	Scan to 290.0K at 0.8K per minute	3	290	0	0	0	0.8
394	1.00E-06	Measure for 30.0 minutes	4	290	0	0	30	0
395	1.00E-06	Scan to 4.0K at 1.2K per minute	3	4	0	0	0	1.2
396	1.00E-06	Measure at minimum for 15.0 minutes	5	4	0	0	15	0
397	1.00E-06	Scan to 290.0K at 0.8K per minute	3	290	0	0	0	0.8
398	1.00E-06	Measure for 30.0 minutes	4	290	0	0	30	0
399	1.00E-06	Stop	7	290	0	0	0	0

The resulting data is then output as a series of (several hundred) text files, these can easily be sorted by temperature and then concatenated in the terminal using the following command[1]. In Linux (using bash):

```
ls -rt *.txt | xargs -n 1 tail -n +2 >filename.out
```

[1]In Windows it is possible to do this using e.g. powershell, but it is simpler to use a bash emulator such as cygwin and use the above command. This strips the header off all the files and concatenates them into a single file, which can then be analysed.

The alternative way to perform these measurements was using a different LabVIEW program developed during this project. However, temperature control was not yet possible using this, which made it less suitable for measurements at multiple temperatures for which the sample needed to be measured over several days.

Appendix B

Operation of the Liquid Helium Bath Cryostat

Further to the closed-cycle cryostat mentioned elsewhere, there is also a bath cryostat located in the same laboratory. Rather than using helium gas supplied by a compressor in a closed cycle, the bath cryostat relies on the sample being submerged in a bath of liquid helium.

Samples are mounted onto a flat copper sample stage with cryogenic varnish which serves to anchor the sample both thermally and mechanically. Electrical connections are then made by means of silver paint or pressed indium. The sample space in this system is considerable smaller than in the closed-cycle cryostat so at this time there is no facility for a system of clips to make electrical contact such as is available in the closed-cycle cryostat. The sample space is sealed inside a stainless steel tube using an indium gasket which must be prepared each time. Care must be taken when tightening the seal such that the gasket is deformed evenly, to this end it is recommended that screws on alternating sides are tightened so as not to deform one side more than the other. The sample holder should then be leak tested before installation into the bath cryostat. The sample and thermometer can then be connected to the electrical equipment, consisting of a voltmeter and current source for each of the sample and thermometer. These are connected through a USB-GPIB converter to a laptop containing the LabVIEW program which runs

the measurement.

The bath cryostat itself is comprised of several chambers inside, as illustrated in Figure B.1. Before filling with helium it is necessary to pre-cool the cryostat with liquid nitrogen and ensure an adequate vacuum is achieved in the vacuum jacket. Once precooled the helium can be introduced slowly using a transfer tube. Once cooled to $\sim$4 K the sample can be cooled further by pumping on the helium, this is done by connecting the helium vacuum port to a large single stage rotary pump with a high throughput. By pumping on the helium vapour the liquid is cooled. When the temperature is below $\sim$2.1 K the helium becomes superfluid and has zero viscosity. At this point the temperature can be decreased to $\sim$1.5 K by continuing to pump on the helium, provided that there are no leaks for the superfluid helium to escape through.

Measurements in magnetic fields are also possible using this cryostat, which gives it an advantage over the closed-cycle system. A large electromagnet can be used to provide magnetic fields up to approximately 1 T, the magnet can also be rotated to perform both magnetoresistance and Hall effect measurements.

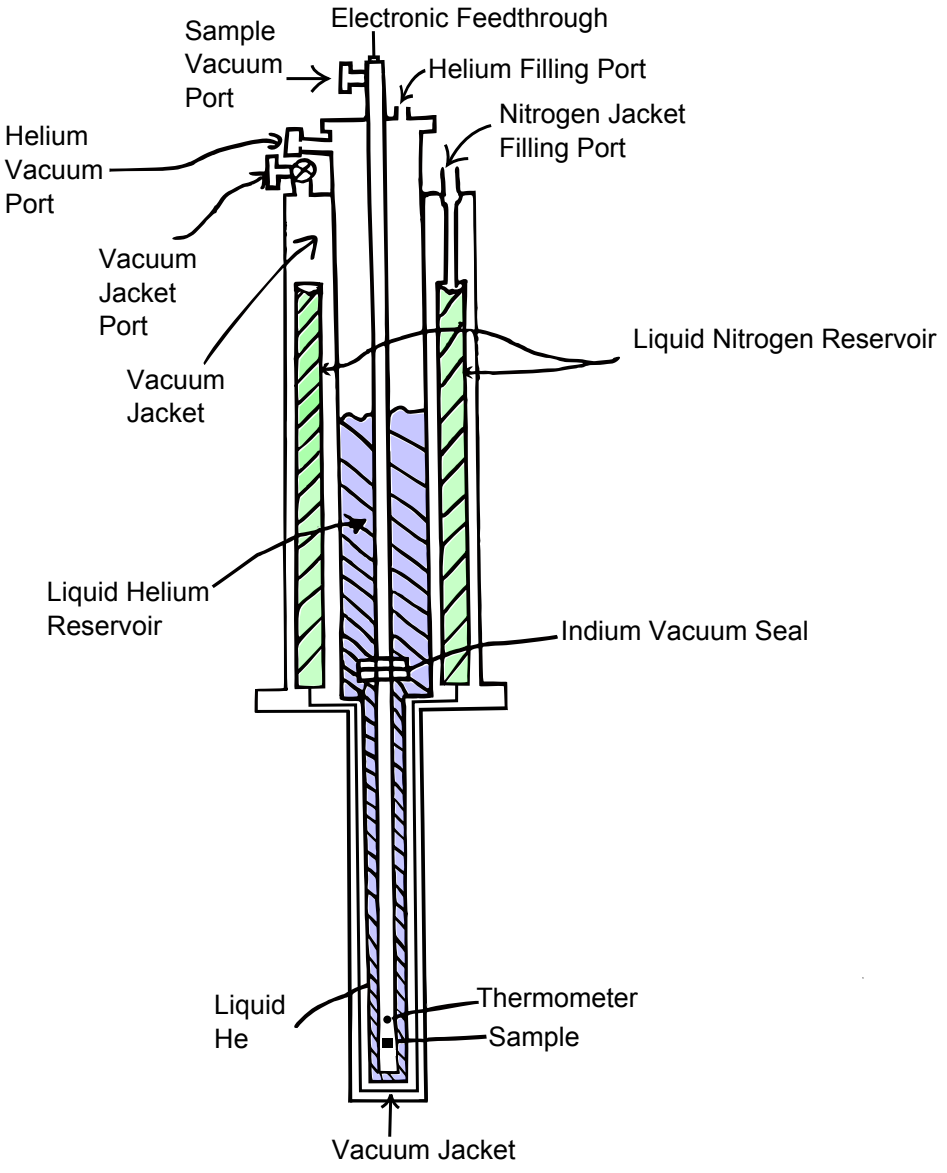

Figure B.1 – Schematic diagram of the liquid helium bath cryostat.

Appendix C

Scanning Electron Microscope

C.1 Introduction

The scanning electron microscope images samples using electrons. Electrons are emitted from a hot filament by way of thermionic emission. This is similar to the electron gun used for materials deposition, however in the case of the SEM the beam is less intense and is focussed in a much more careful way which allows high resolution images to be acquired. The electron beam is controlled and focussed using apertures and electromagnetic lenses. The user interface allows both the discharge voltage and probe current to be controlled, in the case of the probe current the aperture inside the electron gun is being varied. Much as in the case of conventional optics, this produces a shallower depth of field and reduces the exposure time. Varying the high voltage controls the electron energy, higher energies result in larger signal to noise ratios but also an increase both charging and in interaction volume which decreases the spatial resolution.

The interaction volume is the term given to the excited area beneath the sample surface which is excited by the incident electron beam. While the beam striking the surface may be sharply focussed, the interaction volume beneath the surface may be larger than the incident spot size. Higher beam energies result in a larger penetration depth, and in a larger interaction volume.

Much like the optics in a conventional microscope must be aligned, the elec-

tron microscope must be aligned prior to imaging of samples. This must also be done whenever the beam conditions are changed. Once the sample has been installed and moved to the analysis position, an alignment procedure is conducted to optimise image quality. A scanned image of the surface is then obtained using deflection coils which raster the beam across the sample surface.

C.2 Measurement Modes

The three different measurement modes used during this project are outlined below, along with a brief description of the SEM operation which is common to all three.

Secondary electron imaging captures secondary electrons emitted after the incident beam has interacted with the specimen. These electrons are much lower in energy than the surface electrons, because of this they can only escape the sample from within a few nm of the surface.

Backscatter imaging captures electrons which still retain their high energies from the accelerated beam, these electrons scatter elastically off atoms in the sample. The scattering cross section is a function of the atomic mass of the species, resulting in a contrast between high and low mass species. This makes the backscatter configuration useful for measuring multi-layered structures comprised of layers with different atomic mass. Due to the fact that the backscatter electrons are high in energy, they have a larger penetration depth (lower capture cross-section) within the sample, this means that electrons from deep in the sample may be observed. Because these electrons may have scattered from somewhere deep in the interaction volume, the resolution of the backscatter technique is lower than that of the secondary electron imaging measurement mode.

The third technique used in this project is EDS. This technique relies on the x-rays emitted when high energy electrons interact with atoms in the sample. The high energy electrons may cause a core electron to be ejected, an electron from a higher orbital may then relax to fill the core shell by means of x-ray emission. Because the x-rays emitted have energies that are fixed, and specific to the chem-

ical element present, this technique is useful to assay the chemical composition of the sample. EDS is limited in much the same way as backscatter imaging in that it requires high beam energies, and the x-rays emitted may originate from within the interaction volume. Some x-ray peaks also overlap, and the absorption cross section of x-rays having different energies will be different (x-rays from different depths will have different escape probabilities), this reduces the quantitative usefulness of the technique.

Appendix D

Analysing the Gd Contact Voltage

The sample voltage can be modelled more accurately than the rough calculations made in Section 3.5. In general it is possible to solve for an arbitrary film underneath the top contact, which may be comprised of multiple layers and may be non-linear. However, the 1D solution for a GdN/Gd bilayer will be shown here. This is a further development of the rough calculation shown in Section 3.5. The Gd resistivity is $\sim 100\ \mu\Omega\,\mathrm{cm}$ [77], much higher than that of the $2\ \mu\Omega\,\mathrm{cm}$ gold contact [120]. The majority of the contact resistance drop then originates in the Gd contact and the problem can be approximated to one dimension. In this case the top contact can be modelled in terms of infinitesimal strips[1], each with a resistance parallel to the film of

$$\frac{\rho_{Gd}dx}{wt_{top}},$$

where ρ_{Gd} is the Gd resistivity, w is the contact width and t_{top} the thickness of the top contact. The GdN layers is modelled as an array of infinitesimal resistors perpendicular to the film each having a resistance

$$\frac{\rho_{GdN}t_{GdN}}{wdx}.$$

[1]This is similar to the problem of an unbalanced resistance ladder, however in this case the source leads are arranged slightly differently and the resistors are continuous and infinitesimal.

The voltage drop across a distance dx of the top layer is then

$$dV_{top} = -I\frac{\rho_{Gd}dx}{wt_{top}}. \tag{D.1}$$

Similarly, the change in current due to current losses down through the GdN layer is

$$dI = -V_{GdN}\frac{wdx}{\rho_{GdN}t_{GdN}}. \tag{D.2}$$

Combining Equations D.1 and D.2 gives a second order differential equation

$$\frac{d^2V}{dx^2}\left(\frac{1}{\rho_{top}/t_{top}}\right) - \frac{V}{\rho_{GdN}t_{GdN}} = 0,$$

which has a solution

$$V = V_0 \exp\left(-x\sqrt{\frac{\rho_{Gd}/t_{Gd}}{\rho_{GdN}t_{GdN}}}\right). \tag{D.3}$$

This gives a voltage which decays exponentially from the leading edge of the top contact.

For qualitative comparison with the analytic solution, finite element modelling was performed using the electric currents module in COMSOL [121].

A 200×100 µm Au/GdN/Gd junction was studied, with each layer being 100 nm thick. A current density was injected into the broadside of the top (Gd) layer. The ground was set to be the right hand side of the bottom (Au) layer. The voltage profile along the current path between these two points was then modelled. Figure D.1 shows the voltage profile across the Gd layer for three different realistic GdN resistivities (0.1 Ω cm, 1 Ω cm, and 10 Ω cm). As the GdN resistivity is increased the solution approaches the 1D limit used in the analytic solution above. Examining the voltage in the Gd layer for the study with the most resistive GdN (10 Ω cm) it is possible to compare the finite element result with the analytic solution in Equation D.3. Figure D.2 reveals that the Gd voltage indeed follows an exponential decay. Fitting of this curve to extract the decay constant yielded a result consistent within 10% of the analytic solution[2].

[2]Here the 10% disagreement is most likely due to the fact that the bottom Au contact is not an equipotential. It is apparent in Figure D.1 that there is a variation in the voltage distribution across the Gd contact, even in the case of the most resistive 10 Ω cm GdN layer modelled.

For comparison, a sample was also modelled with a 10^6 Ω cm GaN barrier sandwiched between two 10 Ω cm GdN layers[3]. Figure D.3 shows the results of this model, for which the voltage drop occurs entirely across the GaN barrier.

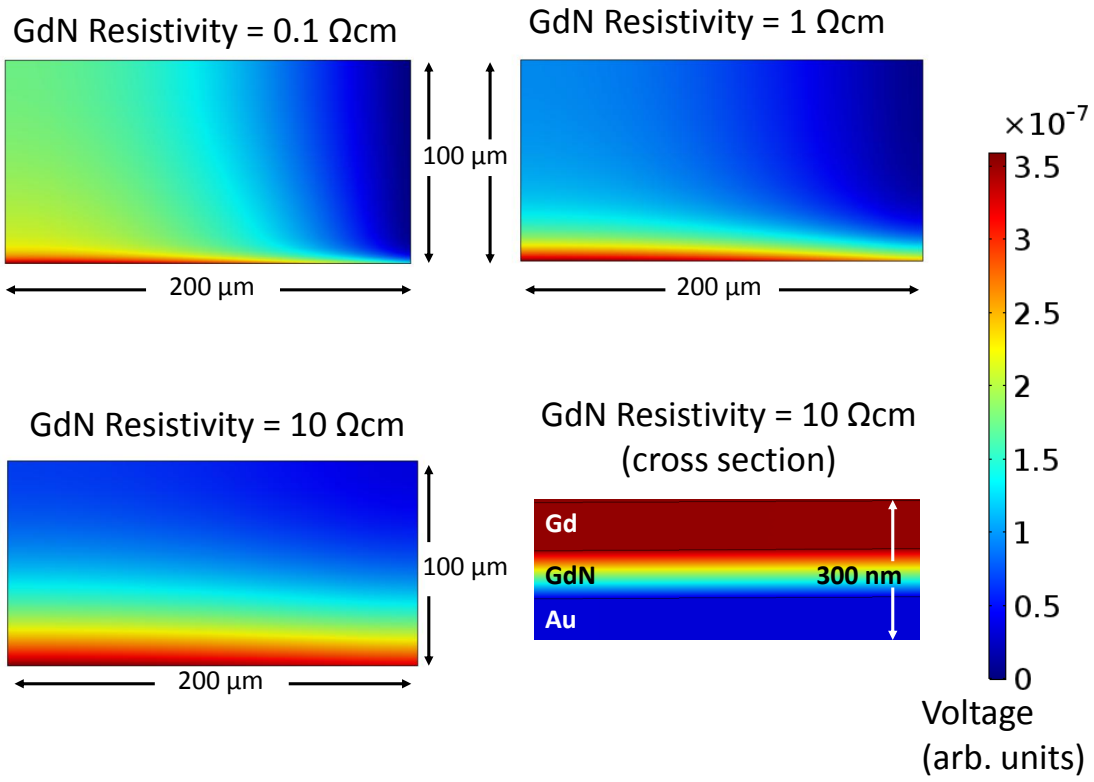

Figure D.1 – Modelled voltage profiles for several different junctions with realistic dimensions and GdN resistivities. Here the current is being injected into the lower edge of the top Gd layer, and flowing out through the right hand side of the Au film beneath. The voltage profile is displayed from both a top down, and side on perspective at the edge of current injection.

[3]This model does not take into account the non-linearity observed in tunnel junctions.

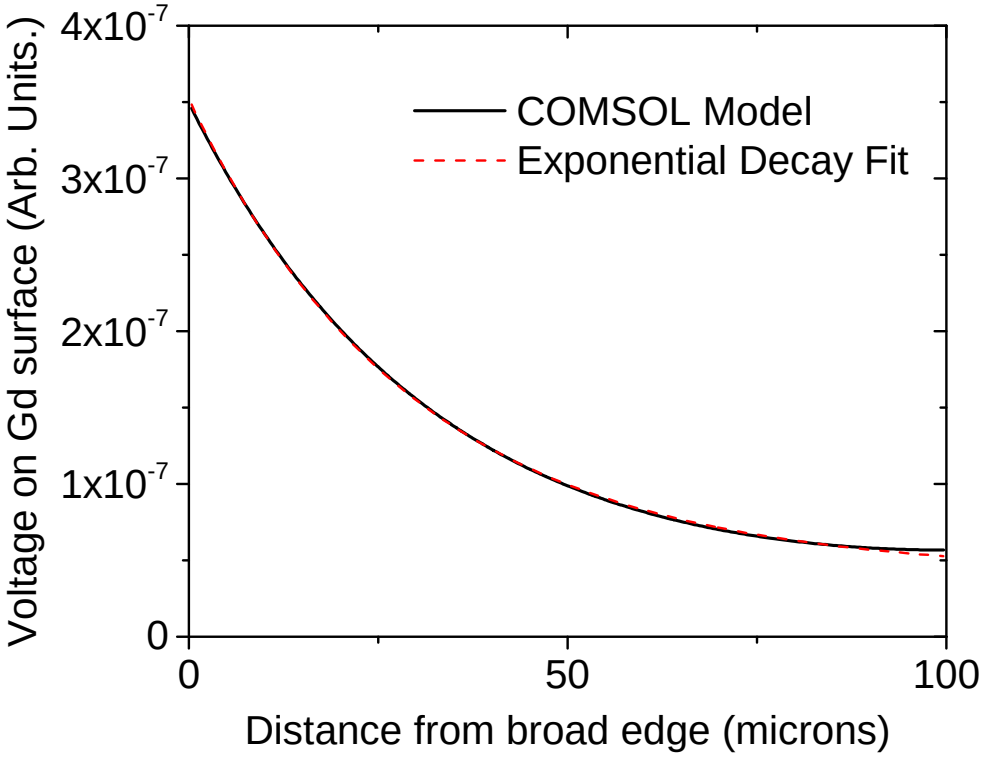

Figure D.2 – Voltage in the Gd layer as a function of distance from the broad edge.

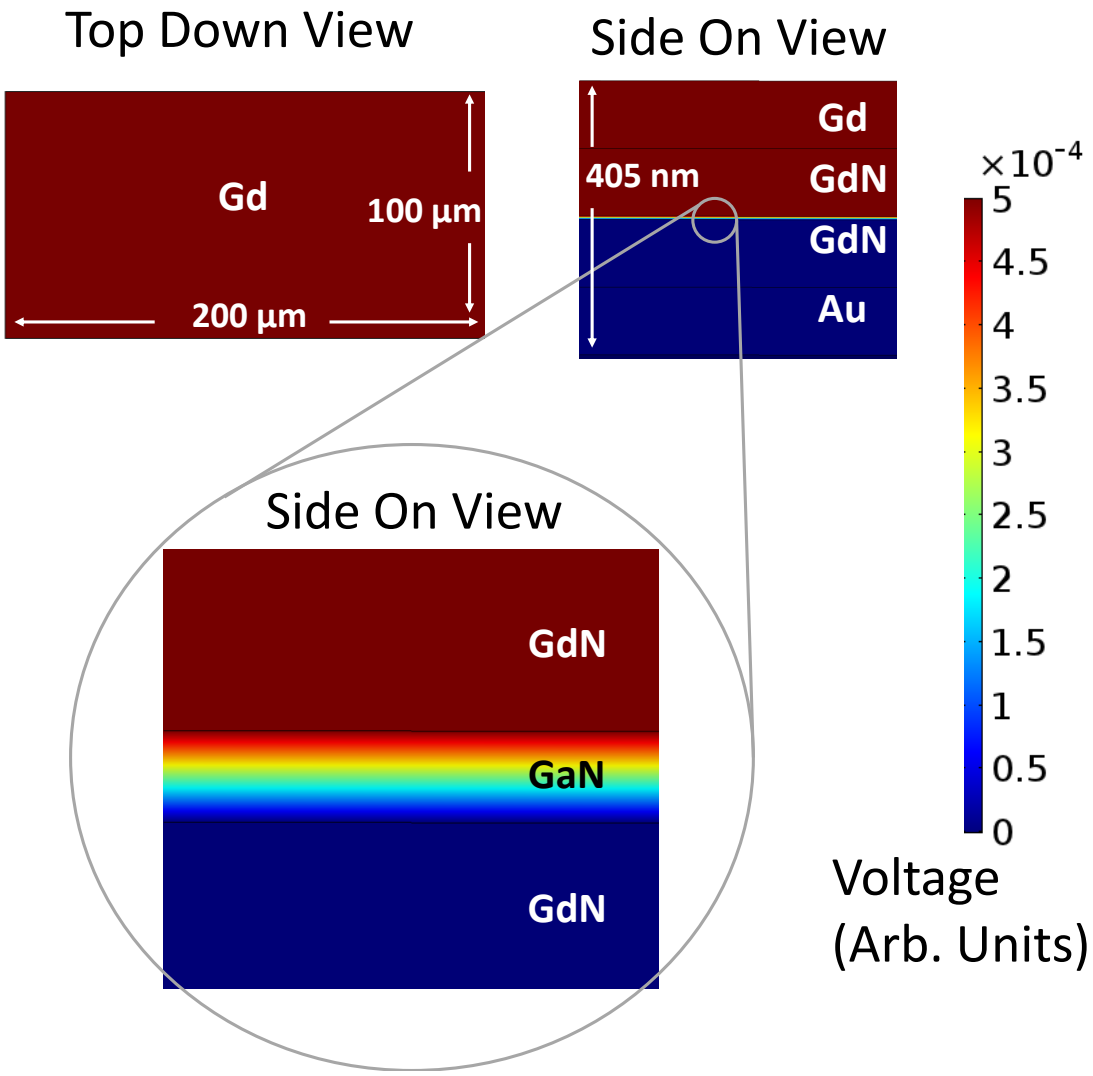

Figure D.3 – Modelled voltage profile for a Au/GdN/GaN/GdN/Gd junction, which is displayed from both a top down and side on perspective. Here the voltage drop occurs entirely across the GaN layer.

Appendix E

Simmons Model Derivation

Variables used in this appendix

$\hbar$, h	Planck constant.
t	Time.
m,m_e	Electron rest mass = 9.11×10^{-31} kg.
v	Velocity.
e	Electronic charge = 1.60×10^{-19} C.
s	Barrier thickness.
s_1,s_2	Barrier edges at the Fermi level.
Δs	$s_2 - s_1$.
$f(E)$	Fermi-Dirac function.
J	Current density.
V	Voltage.
$V(x)$	Potential. This is the barrier height referenced to $E = 0$.
E_F	Fermi level.
φ	Height of the barrier at the Fermi level.
ψ	Work function of electrode.
$\bar{\varphi}$	Average barrier height.
β	Dimensionless correction factor (usually set to 1).
λ	$= e^2 \ln 2/8\pi\epsilon s$.
ϵ	Barrier permittivity.
K	Dielectric constant.
k_B	Boltzmann Constant = 1.38×10^{-23} $m^2kgs^{-2}K^{-1}$ (SI).

Parameters used in the Simmons model relating to the barrier are depicted schematically in Figure E.1 for an arbitrarily shaped barrier.

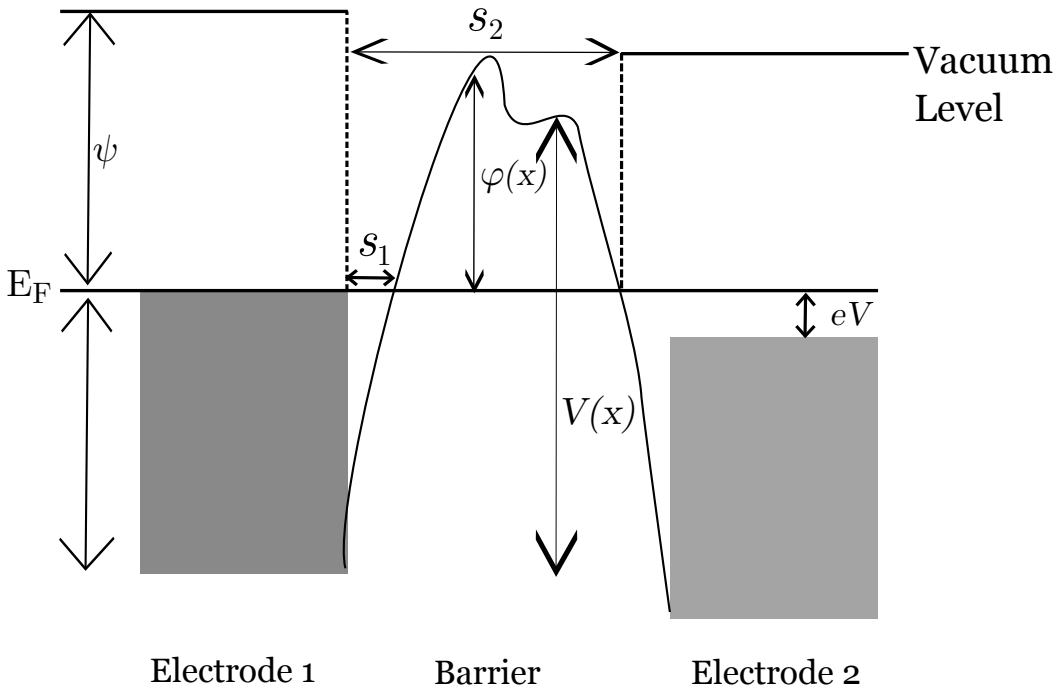

Figure E.1 – Schematic diagram of an arbitrary potential barrier separating two electrodes, with parameters labelled. Shaded rectangles represent filled states in the electrodes.

E.1 Wentzel-Kramers-Brillouin approximation

In order to derive the Simmons model, the transmission coefficient for electrons tunnelling through the barrier must first be considered. The Simmons model is based on calculating both the possibility of electrons tunnelling (through the Fermi-Dirac function) but also the probability (which requires something akin to a transmission coefficient). The approximation for this used by Simmons is known

as the Wentzel-Kramers-Brillouin (WKB) approximation.

The final result here will be an expression for the tunnelling probability between two electrodes separated by an insulating barrier, this is then used in the Simmons model. Simmons uses the expression derived by Bohm [122], while here the working of both Griffiths and Murayama will be followed [123, 124]. These, and other derivations of the WKB model are employed by many others and can be found in many textbooks on quantum theory.

Starting with a wavefunction

$$\psi(x,t) = \exp\left(iS(x,t)/\hbar\right). \tag{E.1}$$

It will be shown below that our function $S(x,t)$ satisfies the so-called Hamilton-Jacobi equation by starting from the Schrödinger equation and making a classical approximation, meaning that S satisfies the equation of motion in the classical limit.

Starting with the Schrödinger equation in one dimension (only considering tunnelling in one-dimension, as in the Simmons model):

$$i\hbar\frac{\partial}{\partial t}\psi(x,t) = \left[\frac{-\hbar^2\vec{\nabla}^2}{2m} + V(x)\right]\psi(x,t), \tag{E.2}$$

$$\frac{\partial\psi}{\partial t} = \frac{\partial S}{\partial t}\frac{i}{\hbar}\exp(iS(x,t)/\hbar),$$

then the first term in E.2 becomes

$$\frac{\partial\psi}{\partial t} = -\frac{\partial S}{\partial t}\psi.$$

Then, for the second term

$$\vec{\nabla}^2\psi = \frac{\partial^2\psi}{\partial x^2} = \frac{i}{\hbar}\frac{\partial^2 S}{\partial x^2}\psi(x,t) + \left(\frac{\partial S}{\partial x}\right)^2\left(\frac{i}{\hbar}\right)\psi(x,t),$$

so

$$\frac{-\hbar^2}{2m}\vec{\nabla}^2\psi = \left(\frac{-i\hbar}{2m}\vec{\nabla}^2 S + \frac{(\vec{\nabla}S)^2}{2m}\right)\psi,$$

which means that, after cancelling the ψ terms (which assumes they are non-zero), Eq. E.2 becomes

$$-\frac{\partial S}{\partial t} = \frac{(\vec{\nabla}S)^2}{2m} - \frac{i\hbar}{2m}\vec{\nabla}^2 S + V(x). \tag{E.3}$$

This is the point at which the so-called classical limit $\hbar \to 0$ is taken. In this case Equation E.3 becomes

$$-\frac{\partial S}{\partial t} = \frac{(\vec{\nabla}S)^2}{2m} + V(x). \tag{E.4}$$

This is the classical Hamilton-Jacobi equation, a first order non-linear partial differential equation which is used in classical mechanics for identifying conserved quantities. This shows that the function $S(x,t)$ satisfies classical mechanics, but what does that mean? We have started from quantum mechanics (the Schrödinger equation) and ended up at classical mechanics (the Hamilton-Jacobi equation) by way of approximating $\hbar$. What we would like is a tractable semiclassical approximation for quantum mechanics. This is the idea behind the WKB approximation; we keep terms up to a certain order in order in $\hbar$ to find approximate solutions to the Schrödinger equation. So instead of sending $\hbar$ to zero, we look for solutions for small $\hbar$.

It is possible to perform a series expansion in $\hbar$ of $S(x,t)$ to get

$$S(x,t) = S_0 + \hbar S_1 + \hbar^2 S_2 + \cdots \tag{E.5}$$

This is called the semi-classical expansion[1]. Equation E.5 can be inserted term by term into Equation E.3.

The first series solution (zeroth order) is just the Hamilton-Jacobi Equation (Eq. E.4) above with $S = S_0$. The first order solution can then be evaluated by keeping terms up to $\hbar$. Doing this term-by term it can be seen that, for first term in Equation E.3

$$-\frac{\partial S}{\partial t} = -\frac{\partial}{\partial t}(S_0 + \hbar S_1) = -\frac{\partial \hbar S_1}{\partial t} + \frac{(\vec{\nabla}S_0)^2}{2m} + V(x)^2. \tag{E.6}$$

[1]In general each of these terms S_n may themselves be functions $S_n(x,t)$.

[2]Here the zeroth order solution to E.4 with $S = S_0$ has been employed.

Similarly, for the second term in Equation E.3

$$\frac{(\vec{\nabla}S)^2}{2m} = \frac{((\vec{\nabla}(S_0 + \hbar S_1)))^2}{2m} = \frac{(\vec{\nabla}S_0)^2 + (\vec{\nabla}\hbar S_1)^2 + 2\vec{\nabla}S_0\vec{\nabla}\hbar S_1}{2m}, \tag{E.7}$$

and again for the third term

$$\frac{-i\hbar\vec{\nabla}^2 S}{2m} = \frac{-i\hbar\vec{\nabla}^2(S_0 + \hbar S_1)}{2m}, \tag{E.8}$$

which can be repeated for higher order terms as desired.

Grouping Equations E.6,E.7,E.8 and cancelling terms the "first order" Schrödinger equation becomes[3]:

$$\frac{-\partial S_1}{\partial t} = \frac{1}{2m}(-i\vec{\nabla}^2 S_0 + 2\vec{\nabla}S_0\vec{\nabla}S_1). \tag{E.9}$$

The WKB approximation in its general form terms up to $O(\hbar)$. When applied to the time-independent Schrödinger equation, the spatial and time dependent components of the wave function can be separated, with a time dependence given by $\exp(-iEt/\hbar)$, that is

$$\psi(x,t) = \exp\left(iS(x,t)/\hbar\right) = \exp\left(iS(x)/\hbar\right)\exp\left(-iEt/\hbar\right),$$

which is to say $S(x,t) = S(x) - Et$. For the zeroth order term, S_0, this is just $S_0(x,t) = S_0(x) - Et$[4]. This means that

$$\frac{\partial S_n}{\partial t} = 0 : n > 0.$$

This time dependence can be used along with Eq. E.4 to find a differential equation. First observe that,

$$-\frac{\partial S_0(x,t)}{\partial t} = -\frac{\partial(S_0(x) - Et)}{\partial t} = E = \frac{1}{2m}\left(\frac{\partial S_0(x)}{\partial t}\right)^2 + V(x),$$

[3]Terms of order $\hbar^2$ and higher have been omitted at this point.

[4]As no $\hbar$ appears in this Et term, the expansion for higher S_n terms does not contain the time dependent part. That is

$$S(x,t) = S_0 + \hbar S_1 + \hbar^2 S_2 + \cdots - Et$$

.

which can be rearranged and integrated to

$$S_0(x) = \pm \int \sqrt{2m(E - V(x'))}dx'. \tag{E.10}$$

Because the first order term is time independent, Eq. E.9 becomes,

$$i\vec{\nabla}^2 S_0 = 2\vec{\nabla} S_0 \vec{\nabla} S_1,$$

and together with Equation E.10 this differential equation can be rearranged to get

$$S_1(x) = i \int \frac{\nabla^2 S_0(x)}{\vec{\nabla} S_0} dx = \frac{i \ln\left[\sqrt{2m(E - V(x))}\right]}{2} + C. \tag{E.11}$$

Now, all the ingredients to obtain the wave function with $S(x,t)$ to first order are prepared and Equations E.11 and E.1 can be combined to get,

$$\begin{aligned}\psi(x,t) &= \exp\left(iS(x,t)/\hbar\right) = \exp\left(iS_0(x)/\hbar + iS_1(x)\right)\exp\left(-Et/\hbar\right) \\ &= \frac{C}{(2m(E - V(x))^{1/4}} \exp\left(\pm\frac{i}{\hbar}\int \sqrt{2m(E - V(x))}dx\right)\exp\left(-Et/\hbar\right).\end{aligned}$$

The next step is to consider the case of tunnelling, forgoing the time dependence and considering the case when $E < V$. Then $\sqrt{2m(E - V(x))}$ is imaginary and

$$\psi(x) = \frac{C}{(2m(E - V(x))^{1/4}} \exp\left(\pm\frac{i}{\hbar}\int \sqrt{2m(E - V(x))}dx\right). \tag{E.12}$$

Now examine the case of an electron scattering from a rectangular barrier. The wavefunctions on the left of the barrier for the incident and reflected waves are given using the usual exponential form

$$\psi(x) = A\exp\left(ikx\right) + B\exp\left(-ikx\right),$$

with $k = \sqrt{2mE}/\hbar$. On the right hand side of the barrier, there is no incident wave but only a transmitted wave and

$$\psi(x) = F\exp\left(ikx\right).$$

The tunnelling probability, given by the transmission coefficient is then given as

$$T = \frac{|F|^2}{|A|^2}.$$

To find the wavefunctions inside the barrier Equation E.12 is used and

$$\psi(x) = \frac{C}{(2m(E-V(x))^{1/4}} \exp\left(+\frac{i}{\hbar}\int \sqrt{2m(E-V(x))}dx\right) + \frac{D}{(2m(E-V(x))^{1/4}} \exp\left(-\frac{i}{\hbar}\int \sqrt{2m(E-V(x))}dx\right).$$

Caveat: the next step makes an approximation which reduces the accuracy of the model for low or narrow barriers. Ultimately this means that the Simmons model should only be applied when the barrier is sufficiently wide and thick. Making the approximation that the barrier is thick and high enough that the exponentially increasing term is negligible (meaning that there is only a decaying exponential inside the barrier) then $C \to 0$. Matching coefficients at the boundaries gives the transmission coefficient in terms of the decrease of the exponential across the barrier

$$T = D(E_x) = \exp\left(\frac{-4\pi(2m)^{1/2}}{h}\int_{s_1}^{s_2}(E_F + \varphi(x) - E_x)^{1/2}dx\right). \tag{E.13}$$

This is the transmission probability $D(E_x)$ used in the Simmons model[5].

E.2 Simmons' Temperature Independent Model for Tunnelling

This section follows the derivation of Simmons [92] with additional working and comments. There are many earlier studies examining electron tunnelling through barriers, such as the models of Holm and Stratton [89, 125]. The Simmons model is useful as it parameterises the barrier in terms of "real" quantities while the

[5]This $D(E_x)$ is the tunnelling probability in the notation used by Simmons, and should not be confused with the density of states.

Stratton (and other) model has variables which depend on voltage in their integrals. More modern models also account for three dimensional tunnelling, along with tunnelling of multiple spin channels [88,126]. While these more sophisticated treatments may be more accurate, and more useful for accounting for tunnelling due to different bands, the Simmons model represents a good first step for extracting barrier parameters and characterising the differences between similar devices. The problem, along with a definition of the variables used, is illustrated schematically in Figure E.1 for an arbitrarily shaped barrier. In the case of a rectangular barrier $\Delta s \to s_2 = s$ as $s_1 \to 0$.

The number of electrons tunnelling from electrode 1 to electrode 2 is given by:

$$N_1 = \int_0^{v_m} v_x n(v_x) D(E_x) dv_x = \frac{1}{m} \int_0^{E_m} n(v_x) D(E_x) dE_x, \tag{E.14}$$

where v_m, E_m are the maximum velocity and energy of electrons in electrode 1, respectively. $n(v_x)dv_x$ is the number of electrons per unit volume having a velocity in the x direction between v_x and $v_x + dv_x$[6].

If we assume that the electrons have an isotropic velocity distribution inside the electrodes then

$$n(v)dv_x dv_y dv_z = \frac{2m^4}{h^3} f(E) dv_x dv_y dv_z,$$

with $f(E)$ the Fermi-Dirac distribution function. Using this we get:

$$n(v_x) = \frac{2m^4}{h^3} \int\int_{-\infty}^{+\infty} f(E) dv_y dv_z = \frac{4\pi m^3}{h^3} \int_0^{\infty} f(E) dE_r, \tag{E.15}$$

where a change into polar coordinates has been made using $v_r^2 = v_y^2 + v_z^2$, $E_r = \frac{m v_r^2}{2}$ and $dE_r = m v_r dv_r$ [7]. Substituting E.15 into E.14:

$$N_1 = \frac{4\pi m^2}{h^3} \int_0^{E_m} D(E_x) dE_x \int_0^{\infty} f(E) dE_r.$$

[6]Here the free electron mass is used. This is one of several tacit assumptions, along with the isotropic velocity distribution, within the model which treats the system as metallic.

[7]After changing coordinates the integrals become:

$$\int\int_{-\infty}^{+\infty} dv_y dv_z = \int_0^{2\pi} \int_0^{+\infty} v_r d\theta dv_r = 2\pi \int_0^{\infty} v_r dv_r = 2\pi \int_0^{\infty} dE_r/m \tag{E.16}$$

.

Similarly, for electrons tunnelling from electrode 2 into electrode 1 and implicitly assuming the tunnelling probability is the same in both directions:

$$N_2 = \frac{4\pi m^2}{h^3} \int_0^{E_m} D(E_x) dE_x \int_0^{\infty} f(E + eV) dE_r.$$

The net flow $N = N_1 - N_2$ is then

$$N = \int_0^{E_m} D(E_x) dE_x \left(\frac{4\pi m^2}{h^3} \int_0^{\infty} \left[f(E) - f(e + eV) \right] dE_r \right).$$

Now define[8]:

$$\zeta_1 = \frac{4\pi m^2 e}{h^3} \int_0^{\infty} f(E) dE_r,$$

and

$$\zeta_2 = \frac{4\pi m^2 e}{h^3} \int_0^{\infty} f(E + eV) dE_r.$$

Then, by setting $\zeta = \zeta_1 - \zeta_2$, J can be written as

$$J = \int_0^{\infty} D(E_x) \zeta dE_x, \tag{E.17}$$

for a generalised barrier, with voltage $V(x) = E_F + \varphi(x)$ and $D(E_x)$ given by Equation E.13.

To integrate Equation E.13 Simmons first examines the integral in a more general form over an interval $\Delta s = s_2 - s_1$.

First, define[9]

$$\bar{f} = \frac{1}{\Delta s} \int f(x) dx. \tag{E.18}$$

Then, we wish to examine an integral of the form[10]

$$\int_{s_1}^{s_2} f^{1/2}(x) dx = \bar{f}^{1/2} \int_{s1}^{s2} \left[1 + \frac{(f(x) - (\bar{f}))^{1/2}}{\bar{f}} \right]^{1/2}.$$

[8]Here we multiply N, the number of electrons per unit area per unit time, by e to get the current density.

[9]Note that although $\bar{f}$ is the mean value of f it does not itself explicitly depend on x.

[10]Here the term in brackets has been obtained by adding and subtracting a $\bar{f}$ term, and taking $\bar{f}^{1/2}$ out of the integral.

The square root term can be expanded using the Taylor series expression for $\sqrt{(1+g(x))}$. Here Simmons only keeps terms to second order[11] to get

$$\int_{s_1}^{s_2} f^{1/2}(x)dx \simeq \bar{f}^{1/2}\Delta s\left[1-\frac{1}{8f^2\Delta s}\int_{s_1}^{s_2}(f(x)-\bar{f})^2dx\right]=\beta\bar{f}^{1/2}\Delta s. \quad \text{(E.19)}$$

where $\bar{f}$ is the mean value of $f(x)$ over the interval and β is a correction factor (approximately 1)[12].

Using Equation E.19, Equation E.13 can be integrated to get

$$D(E_x)\simeq\exp(-A(E_F+\bar{\varphi}-E_x)^{1/2}). \quad \text{(E.20)}$$

Here $\bar{\varphi}$ is the mean barrier height defined as

$$\bar{\varphi}=\frac{1}{\Delta s}\int_{s_1}^{s_2}\varphi(x)dx$$

and $A=4\pi\beta\Delta s(2m)^{1/2}/h$. Now, assuming that because this is a temperature independent model $T\to 0$ and $f(E)=1$ up to E_F, thus

$$\int_0^\infty f(E)dE\to\int_0^\infty\lim_{T\to0}\frac{1}{e^{(E_x-E_F)/kT}+1}=\int_0^\infty\Theta(E_F-E_x)dEx=E_F-E_x \quad \text{(E.21)}$$

where Θ is the Heaviside step function. This amounts to saying that the Fermi function is 1 up to E_F and zero thereafter[13] and so

$$\zeta_1=\frac{4\pi m^2e}{h^3}(E_F-E_x)\quad;\quad\zeta_2=\frac{4\pi m^2e}{h^3}(E_F-E_x-eV)$$

$$\zeta=\left\{\begin{array}{cc}\frac{4\pi me}{h^3}eV & 0<E_x<E_F-eV\\ \frac{4\pi me}{h^3}(E_F-E_x) & E_F-eV<E_x<E_F\\ 0 & E_x>E_F\end{array}\right\} \quad \text{(E.22)}$$

[11] The first order term is zero due to the definition of $\bar{f}$ in Equation E.18 and as $\int_{s_1}^{s_2}\bar{f}dx=\bar{f}\Delta s$.

[12]
$$\beta=\left[1-\frac{1}{8f^2\Delta s}\int_{s_1}^{s_2}(f(x)-\bar{f})^2dx\right].$$
This is a correction factor and is generally approximated to 1 by neglecting the second term in brackets.

[13] The Heaviside function is zero when the argument becomes negative, hence the chance of sign of the argument in Equation E.21.

Equations E.22 and E.20 can be inserted partwise into Equation E.17 to yield

$$J = \frac{4\pi me}{h^3}\Big\{eV\int_0^{E_F-eV}\exp\left[-A(E_F+\bar{\varphi}-E_x)^{1/2}\right]dE_x + \int_{E_F-eV}^{E_F}(E_F-E_x)\exp\left[-A(E_F+\bar{\varphi}-E_x)^{1/2}\right]dE_x\Big\}.$$

To integrate this, Simmons then adds and subtracts the term

$$\int_{E_F-eV}^{E_F}(\bar{\varphi})\exp\left[-A(E_F+\bar{\varphi}-E_x)^{1/2}\right]dE_x \tag{E.23}$$

to obtain:

$$J = \frac{4\pi me}{h^3}\Big\{eV\int_0^{E_F-eV}\exp\left[-A(E_F+\bar{\varphi}-E_x)^{1/2}\right]dE_x + \int_{E_F-eV}^{E_F}(E_F+\bar{\varphi}-E_x)\exp\left[-A(E_F+\bar{\varphi}-E_x)^{1/2}\right]dE_x - \bar{\varphi}\int_{E_F-eV}^{E_F}\exp\left[-A(E_F+\bar{\varphi}-E_x)^{1/2}\right]dE_x\Big\}. \tag{E.24}$$

Equation E.24 can now be integrated piecewise, the first term of which is:

$$\frac{4\pi me}{h^3}eV\int_0^{E_F-eV}\exp\left[-A(E_F+\bar{\varphi}-E_x)^{1/2}\right]dE_x$$

$$= \frac{4\pi me}{h^3}(eV)\left[\frac{2(1+A(E_F+\bar{\varphi})^{1/2})\exp\left[-A(E_F+\bar{\varphi}-E_x)^{1/2}\right]}{A^2}\right]_0^{E_F-eV}$$

$$= \frac{8\pi mV}{h^3}\left(\frac{e}{A}\right)^2\Big\{\left[A(\bar{\varphi}+eV)^{1/2}+1\right]\exp\left[-A(\bar{\varphi}+eV)^{1/2}\right] - \left[A(\bar{\varphi}+E_F)^{1/2}+1\right]\exp\left[-A(\bar{\varphi}+E_F)^{1/2}\right]\Big\}. \tag{E.25}$$

Now, $eV << E_F$ so that the second term is negligible[14]. And Equation E.25 reduces to

$$\left(\frac{8\pi me^2V}{h^3A}\right)\left((\bar{\varphi}+eV)^{1/2}+1/A\right)\exp\left(-A(\bar{\varphi}+eV)^{1/2}\right). \tag{E.26}$$

[14]This approximation can be justified by observing that the filled states extend many eV below E_F [24], while the energies probed with an applied voltage are up to 1-2 V.

The third integral from Eq. E.24 has the same integrand with different bounds, and can be integrated and approximated the same way to get

$$\frac{4\pi me}{h^3}(\bar{\varphi})\left[\frac{2(1+A(E_F+\bar{\varphi})^{1/2})\exp\left[-A(E_F+\bar{\varphi}-E_x)^{1/2}\right]}{A^2}\right]_0^{E_F-eV}$$
$$=\left(\frac{8\pi me}{h^3A^2}\right)\bar{\varphi}\{[A\bar{\varphi}^{1/2}+1]\exp\left(-A\bar{\varphi}^{1/2}\right)-[A(\bar{\varphi}+eV)^{1/2}+1]\exp\left[-A(\bar{\varphi}+eV)^{1/2}\right]\}. \tag{E.27}$$

The second integral now requires a little bit more work, here Simmons invokes a substitution and uses a standard integral. Setting $z^2 = E_F + \bar{\varphi} - Ex$, then dx becomes $-2zdz$ and the third integral in Eq. E.24 is[15]

$$-\frac{8\pi me}{h^3}\int_{E_x=E_F-eV}^{E_F} z^{-1}z^3\exp\left(-Az\right)dz=\frac{8\pi me}{h^3}\exp\left(-Az\right)\left(\frac{z^3}{A}+\frac{3z^2}{A^2}+\frac{6z}{A^3}+\frac{6}{A^4}\right)\Bigg|_{E_x=E_F-eV}^{E_F}, \tag{E.28}$$

where the third and fourth terms in the sum are negligible. Equation E.28 is then

$$\frac{8\pi me}{h^3}\exp\left(-Az\right)\left(\frac{z^3}{A}+\frac{3z^2}{A^2}\right)\Bigg|_{E_x=E_F-eV}^{E_F}$$
$$=\frac{8\pi me}{h^3}\exp\left(-A(E_F+\bar{\varphi}-E_x)^{1/2}\right)\left(\frac{(E_F+\bar{\varphi}-E_x)^{3/2}}{A}+\frac{3(E_F+\bar{\varphi}-E_x)}{A^2}\right)\Bigg|_{E_x=E_F-eV}^{E_F}$$
$$=\frac{8\pi me}{h^3}\left[\exp\left(-A\bar{\varphi}^{1/2}\right)\left(\frac{\bar{\varphi}^{3/2}}{A}+\frac{3\bar{\varphi}}{A^2}\right)-\exp\left(-A(\bar{\varphi}+eV)^{1/2}\right)\left(\frac{(\bar{\varphi}+eV)^{3/2}}{A}+\frac{3(\bar{\varphi}+eV)}{A^2}\right)\right]. \tag{E.29}$$

Now it is time to group Equations E.26,E.27,E.29 together, while messy at first many of these terms cancel

$$J \quad = \quad \frac{8\pi me}{h^3A}\left[\left(\exp\left(-A\bar{\varphi}^{1/2}\right)\frac{2\bar{\varphi}}{A}\right)+\exp\left(-A(\bar{\varphi}+eV)^{1/2}\right)\left(\frac{-2\bar{\varphi}}{A}\right)\right],$$

and then rearranging the coefficient by expanding A gives the generalised Simmons equation

$$J=\frac{2}{2\pi h}(\beta\Delta s)^{-2}\{\bar{\varphi}\exp\left(-A\bar{\varphi}^{1/2}\right)-(\bar{\varphi}+eV)\exp\left(-A(\bar{\varphi}+eV)^{1/2}\right)\},$$

[15]Note that the bounds of integration have not been reparametrised in terms of z. This is because the integral will be reparametrised in terms of x before evaluating the definite integral.

which can be expressed in the following form:

$$J = J_0\{\bar{\varphi}\exp\left(-A\bar{\varphi}^{1/2}\right) - (\bar{\varphi}+eV)\exp\left(-A(\bar{\varphi}+eV)^{1/2}\right)\}, \tag{E.30}$$

where

$$J_0 = \frac{e}{2\pi h(\beta\Delta s)^2}.$$

Equation E.30 can also be expressed in terms of numerical values with the constants inserted

$$J(V) = \left[\frac{6.2\times10^{10}}{(\beta\Delta s)^2}\right]\times \{\bar{\varphi}\exp\left(-1.025\beta\Delta s\bar{\varphi}^{\frac{1}{2}}\right) - (\bar{\varphi}+V)\exp\left(-1.025\beta\Delta s(\bar{\varphi}+V)^{\frac{1}{2}}\right)\}.$$

This is the generalised model presented by Simmons in his 1963 paper, he goes on to consider the effect of the image forces and to examine the limits of this model for different voltage regimes and barriers. The result of considering the effect of the image potential manifests as a small correction to the model of the form

$$\bar{\varphi} = \varphi_0 - \frac{eV}{2s}(s_1+s_2) - \left[\frac{1.15\lambda s}{s_2-s_1}\ln\frac{s_2(s-s_1)}{s_1(s-s_2)}\right] = \varphi_I.$$

Using this for a rectangular (symmetric) barrier with the images forces excluded Simmons arrives at the following equation for the current density for voltages less than the barrier height

$$J = (6.2\times10^{10}/s^2)\Big[(\varphi_0 - V/2)\exp\left[-1.025s(\varphi_0-V/2)^{1/2}\right] - (\varphi_0+V/2)\exp\left[-1.025s(\varphi_0+V/2)^{1/2}\right]\Big]. \tag{E.31}$$

Including the image forces yields[16]

[16] In this case

$$\varphi_I = \varphi_0 - \frac{V}{2s}(s_1+s_2) - \left[\frac{5.75}{K(s_2-s_1)}\ln\frac{s_2(s-s_1)}{s_1(s-s_2)}\right],$$

where $s_1 = 6/K\varphi_0$ and $s_2 = s[1-46/(3\varphi_0 Ks+20-2VKs)]+6/K\varphi_0$ for voltages less than the barrier height.

$$J = (6.2 \times 10^{10}/\Delta s^2)\Big[(\varphi_I)\exp\left[-1.025(\varphi_I)^{1/2}\Delta s\right] - (\varphi_I + V)\exp\left[-1.025\Delta s(\varphi_I + V)^{1/2}\right]\Big]. \quad \text{(E.32)}$$

E.3 Temperature Dependent Model

This is built on the Stratton model [125], but is more useful for parametrising experimental data as it is expressed in terms of useful parameters [95].

The starting point for this model is the same as for the temperature independent case, and the temperature dependence is introduced through the Fermi functions.

$$J = \frac{4\pi me}{h^3}\int_0^{E_m} D(E_x)dE_x \int_0^{\infty}[f(E) - f(E + eV)]dE_r, \quad \text{(E.33)}$$

with, as before (here Simmons writes $<\varphi(E_x)>_{av} = E_F + \bar{\varphi} - E_x$)

$$D(E_x) = \exp\left[-A <\varphi(E_x)>_{av}^{1/2}\right],$$

to extend this to non-zero temperatures it is first necessary to evaluate the two antiderivatives involving Fermi functions.

$$\int f(E) = \int \frac{1}{\exp\left(\frac{E-E_F}{k_BT}\right)+1} = \int \frac{\exp\left(\frac{E_F-E}{k_BT}\right)}{1+\exp\left(\frac{E_F-E}{k_BT}\right)} = k_BT\ln\left(\exp\left(\frac{E_F-E}{k_BT}\right)+1\right)+C,$$

similarly

$$\int f(E) = \int \frac{1}{\exp\left(\frac{E+eV-E_F}{k_BT}\right)+1} = k_BT\ln\left(\exp\left(\frac{E_F-E-eV}{k_BT}\right)+1\right)+C,$$

the integrals in Equation E.33 extend from 0 to ∞, here Stratton (and by extension Simmons) invoke an energy conservation argument to change the upper limit to

E_x. Equation E.33 then becomes

$$J = \frac{4\pi mek_BT}{h^3}\int_0^{E_m} \ln\left[\frac{1+\exp\left(\frac{E_F-E_x}{k_BT}\right)}{1+\exp\left(\frac{E_F-E_x-eV}{k_BT}\right)}\right] \times \exp\left(-A < \varphi(E_x) >_{av}^{1/2}\right) dE_x. \tag{E.34}$$

The next step involves expanding $D(E_x)$ as a Taylor series so that the integration can be performed,

$$D(E_x) = \exp\left[-A(E_F + \bar{\varphi} - E_x)^{1/2}\right] = \exp\left[-A\bar{\varphi}^{1/2}[1 + \frac{E_F - E_x}{\bar{\varphi}}]^{1/2}\right]. \tag{E.35}$$

Invoking the power series expansion $(1+x)^{1/2} = 1 + \frac{x}{2} - \frac{x^2}{8} + \ldots$ to first order with $x = \frac{E_F - E_x}{\bar{\varphi}}$ Equation E.35 becomes,

$$D(E_x) = \exp\left[-A\bar{\varphi}^{1/2}[1 + \frac{E_F - E_x}{2\bar{\varphi}^{1/2}}]\right] = \exp\left[\bar{\varphi}^{1/2}\right]\exp\left[-A\frac{E_F - E_x}{2\bar{\varphi}^{1/2}}\right]. \tag{E.36}$$

To truncate this expansion at first order it is assumed that $\frac{E_F - E_x}{\bar{\varphi}} << 1$, which is to say that only the energy levels closest to the Fermi level are being examined. Equations E.34 and E.36 can then be combined to obtain,

$$J(V,T) = \frac{4\pi mek_BT}{h^3}\exp\left[\bar{\varphi}^{1/2}\right]\int_0^{E_m} \ln\left[\frac{1+\exp\left(\frac{E_F-E_x}{k_BT}\right)}{1+\exp\left(\frac{E_F-E_x-eV}{k_BT}\right)}\right] \times \exp\left[-A\frac{E_F - E_x}{2\bar{\varphi}^{1/2}}\right] dE_x.$$

The solution to this integral was published by Murphy and Good in the context of thermionic emission [127][17]. They simplify the problem by extending the upper limit of the integral to infinity, the result is then,

$$J(V,T) = \frac{4\pi me}{h^3B^2}\frac{\pi Bk_BT}{\sin\left(\pi Bk_BT\right)} exp(-A\bar{\varphi}^{1/2})[1 - \exp\left(-BeV\right)], \tag{E.37}$$

where $B = A/2\bar{\varphi}^{1/2}$. Here Simmons has reparameterised in terms of physical constants (where Stratton, and Murphy and Good did not). Which approximates to

[17] Eq. (55) in [127]

the generalised temperature independent model in the limit $T \to 0$. By comparing the temperature independent model to Equation E.37 the temperature independent part of the model can be removed and the resulting equation is,

$$J(V,T) = J(V,0) \times \pi B k_B T / \sin(\pi B k_B T),$$

which when expanding the sin as a power series gives

$$J(V,T) = J(V,0) \times [1 + \frac{(\pi B k_B T)^2}{6} + ...].$$

This can be expressed, with the constants substituted[18], as

$$= J(V,0) \times [1 + 3 \times 10^{-9} (\Delta s T)^2 / \bar{\varphi} + ...]. \quad \text{(E.38)}$$

The second order term in the power series dominates for most real barriers[19].

Combining Equations E.32 and E.38 allows us to model J-V characteristics as a function of temperature with the image forces included, note that this was done with the computer algebra software Maple. [128] The resulting equation which was used for fitting and modelling purposes is included as Figure E.2.

[18]Here the constants in SI units have been used, with Δs converted to Å from metres and $\bar{\varphi}$ to eV from joules.

[19]The fourth-order term is $6.3 \times 10^{-18} (\Delta s T)^4 / \bar{\varphi}^2$ so will be negligible compared with the second order term as long as $(\Delta s T)^2 << 4.8 \times 10^8 \bar{\varphi}$. This approximation will only break down for very low barriers, very wide barriers, or very high temperatures.

$$
\begin{aligned}
J = 6.2 \times 10^{10} \Bigg(& \left(-\frac{1}{2} \left(-2ps + 6\,\frac{V}{Kp} + V \left(s \left(1 - \frac{46}{3pKs + 20 - 2VKs} \right) + 6\,\frac{1}{Kp} \right) \right) s^{-1} - 5.75 \ln \left(\frac{1}{6} \left(s \left(1 - 46\,(3pKs + 20 - 2 \right. \right. \right. \right. \\
& \left. \left. \left. \left. VKs)^{-1} \right) + 6\,\frac{1}{Kp} \right) \left(s - 6\,\frac{1}{Kp} \right) Kp \left(s - s \left(1 - 46\,(3pKs + 20 - 2VKs)^{-1} \right) - 6\,\frac{1}{Kp} \right)^{-1} \right) K^{-1} s^{-1} \left(1 - 46\,(3pKs + 20 - 2VKs)^{-1} \right)^{-1} \right) \\
& \mathrm{e}^{-1.025\,s\left(1 - \frac{46}{3pKs + 20 - 2VKs}\right) \sqrt{-\frac{1}{2}\left(-2ps + 6\frac{V}{Kp} + V\left(s\left(1 - \frac{46}{3pKs + 20 - 2VKs}\right) + 6\frac{1}{Kp}\right)\right) s^{-1} - 5.75 \ln\left(\frac{1}{6}\left(s\left(1 - \frac{46}{3pKs + 20 - 2VKs}\right) + 6\frac{1}{Kp}\right)\left(s - 6\frac{1}{Kp}\right) Kp\left(s - s\left(1 - \frac{46}{3pKs + 20 - 2VKs}\right) + 6\frac{1}{Kp}\right) Kp\left(s - s\left(1 - \frac{46}{3pKs + 20 - 2VKs}\right) - 6\frac{1}{Kp}\right)^{-1}\right) K^{-1} s^{-1} \left(1 - \frac{46}{3pKs + 20 - 2VKs}\right)^{-1}}} \\
& - \left(-\frac{1}{2} \left(-2ps + 6\,\frac{V}{Kp} + V \left(s \left(1 - \frac{46}{3pKs + 20 - 2VKs} \right) + 6\,\frac{1}{Kp} \right) \right) s^{-1} - 5.75 \ln \right. \\
& \left(\frac{1}{6} \left(s \left(1 - \frac{46}{3pKs + 20 - 2VKs} \right) + 6\,\frac{1}{Kp} \right) \left(s - 6\,\frac{1}{Kp} \right) Kp \left(s - s \left(1 - \frac{46}{3pKs + 20 - 2VKs} \right) - 6\,\frac{1}{Kp} \right)^{-1} \right) K^{-1} s^{-1} \left(1 - \frac{46}{3pKs + 20 - 2VKs} \right)^{-1} + V \Bigg) \Bigg) \\
& \mathrm{e}^{-1.025\,s\left(1 - \frac{46}{3pKs + 20 - 2VKs}\right) \sqrt{-\frac{1}{2}\left(-2ps + 6\frac{V}{Kp} + V\left(s\left(1 - \frac{46}{3pKs + 20 - 2VKs}\right) + 6\frac{1}{Kp}\right)\right) s^{-1} - 5.75 \ln\left(\frac{1}{6}\left(s\left(1 - \frac{46}{3pKs + 20 - 2VKs}\right) + 6\frac{1}{Kp}\right)\left(s - 6\frac{1}{Kp}\right) Kp\left(s - s\left(1 - \frac{46}{3pKs + 20 - 2VKs}\right) + 6\frac{1}{Kp}\right) Kp\left(s - s\left(1 - \frac{46}{3pKs + 20 - 2VKs}\right) - 6\frac{1}{Kp}\right)^{-1}\right) K^{-1} s^{-1} \left(1 - \frac{46}{3pKs + 20 - 2VKs}\right)^{-1} + V}} \\
& \left(\left(1 + \frac{3}{10^9}\, sT^2 \left(-\frac{1}{2} \left(-2\,ps + 6\,\frac{V}{Kp} + V \left(s \left(1 - \frac{46}{3pKs + 20 - 2VKs} \right) + 6\,\frac{1}{Kp} \right) \right) s^{-1} - 5.75 \ln \left(\frac{1}{6} \left(s \left(1 - \frac{46}{3pKs + 20 - 2VKs} \right) + 6\,\frac{1}{Kp} \right) \left(s \right. \right. \right. \right. \\
& \left. \left. \left. \left. - 6\,\frac{1}{Kp} \right) Kp \left(s - s \left(1 - 46\,(3pKs + 20 - 2VKs)^{-1} \right) - 6\,\frac{1}{Kp} \right)^{-1} \right) K^{-1} s^{-1} \left(1 - \frac{46}{3pKs + 20 - 2VKs} \right)^{-1} - \frac{1}{2}\,V \right)^{-1} \right) s^{-2} \left(1 - \frac{46}{3pKs + 20 - 2VKs} \right)^{-2}
\end{aligned}
\tag{1}
$$

Figure E.2 – The temperature dependent Simmons model for tunnelling through a rectangular barrier, with the image forces included. Note here the change of notation for barrier height as p instead of φ.

Appendix F

Animated Figures

This appendix contains animated figures which are accessible in the electronic version when a compatible PDF reader is used. The latest versions of Adobe Acrobat should be used to view these animations. Older versions of Acrobat may also work, however the Flash Player plug-in may also need to be installed. Other pdf readers may not play these animations correctly.

In Figure F.1 a layer of photoresist is first spin coated on and developed to reveal a hole into which the bottom contact is grown. The photoresist is then lifted-off and another photoresist layer used to define the second layer. The second layer is comprised of the tunnel junction stack along with the top contact. After deposition of the second layer, the second photoresist layer is lifted-off and the cross-contact geometry tunnel junction is revealed.

Figure F.2 begins with the net moments aligned with a small applied field the, device is in a high resistance state due to the anti-alignment of the spin moments. The magnetic field is then decreased through zero and the GdN moments begin to flip for small applied fields forcing the device into a low resistance state. The SmN flips at larger fields making the device resistive again. Note that this only describes the contrasting behaviour between high and low fields. For intermediate fields there are complicating factors such as twisted magnetic phases, which are discussed in Section 5.3.

This figure includes an animation
which is available in the digital version
of this thesis.

Figure F.1 – Available online, click to play: Schematic animation of lithography and growth steps involved in fabrication of a magnetic tunnel junction.

This figure includes an animation
which is available in the digital version
of this thesis.

Figure F.2 – Available online: Schematic animation of the realignment of layers in a GdN/I/SmN tunnel junction as the magnetic field is reversed and increased.

Bibliography

[1] P. Larson, W. R. L. Lambrecht, A. Chantis, and M. van Schilfgaarde, "Electronic structure of rare-earth nitrides using the LSDA + U approach: Importance of allowing $4f$ orbitals to break the cubic crystal symmetry," *Phys. Rev. B*, vol. 75, p. 045114, Jan 2007.

[2] P. Larson and W. R. L. Lambrecht, "Electronic structure of Gd pnictides calculated within the LSDA+ U approach," *Phys. Rev. B*, vol. 74, no. 8, p. 085108, 2006.

[3] C. M. Lee, "Electrical and Magnetic Investigations of Magnesium-doped Epitaxial Gadolinium Nitride Thin Films," Master's thesis, 2015.

[4] Software Spectra Inc., Portland, USA, *TFCalc 3.5*, Nov. 1993.

[5] M. M. Waldrop, "The chips are down for Moore's law," *Nature News*, vol. 530, no. 7589, p. 144, 2016.

[6] I. Žutić, J. Fabian, and S. D. Sarma, "Spintronics: Fundamentals and applications," *Rev. Mod. Phys.*, vol. 76, no. 2, p. 323, 2004.

[7] R. Wood, "Future hard disk drive systems," *J. Magn. Magn. Mater.*, vol. 321, no. 6, pp. 555–561, 2009.

[8] S. Wolf, D. Awschalom, R. Buhrman, J. Daughton, S. Von Molnar, M. Roukes, A. Y. Chtchelkanova, and D. Treger, "Spintronics: a spin-based electronics vision for the future," *Science*, vol. 294, no. 5546, pp. 1488–1495, 2001.

[9] H. Ohno, A. Shen, F. Matsukura, A. Oiwa, A. Endo, S. Katsumoto, and Y. Iye, "(Ga,Mn)As: A new diluted magnetic semiconductor based on GaAs," *Appl. Phys. Lett.*, vol. 69, no. 3, pp. 363–365, 1996.

[10] G. B. Haxel, J. B. Hendrick, and G. J. Orris, "Rare Earth Elements - Critical Resources for High Technology — USGS Fact Sheet 087-02," Nov 2002.

[11] D. Munoz, "As hybrid cars gobble rare metals, shortage looms," tech. rep., Reuters, 2009.

[12] K. Senapati, M. G. Blamire, and Z. H. Barber, "Spin-filter Josephson junctions," *Nat. Mater.*, vol. 10, no. 11, pp. 849–852, 2011.

[13] P. K. Muduli, A. Pal, and M. G. Blamire, "Crossover from diffusive to tunneling regime in NbN/DyN/NbN ferromagnetic semiconductor tunnel junctions," *Phys. Rev. B*, vol. 89, p. 094414, Mar 2014.

[14] A. Pal, K. Senapati, Z. H. Barber, and M. G. Blamire, "Electric-Field-Dependent Spin Polarization in GdN Spin Filter Tunnel Junctions," *Adv. Mater.*, vol. 25, no. 39, pp. 5581–5585, 2013.

[15] S. Krishnamoorthy, T. F. Kent, J. Yang, P. S. Park, R. C. Myers, and S. Rajan, "GdN Nanoisland-Based GaN Tunnel Junctions," *Nano Lett.*, vol. 13, no. 6, pp. 2570–2575, 2013.

[16] H. Warring, B. J. Ruck, H. J. Trodahl, and F. Natali, "Electric field and photo-excited control of the carrier concentration in GdN," *Appl. Phys. Lett.*, vol. 102, no. 13, p. 132409, 2013.

[17] J. F. McNulty, E.-M. Anton, B. J. Ruck, F. Natali, H. Warring, F. Wilhelm, A. Rogalev, M. M. Soares, N. B. Brookes, and H. J. Trodahl, "Twisted phase of the orbital-dominant ferromagnet SmN in a GdN/SmN heterostructure," *Phys. Rev. B*, vol. 91, p. 174426, May 2015.

[18] D. A. Spedding F, *The Rare Earths*. John Wiley & Sons, Inc., 1961.

[19] W. Klemm and G. Winkelmann, "Zur Kenntnis der Nitride der Seltenen Erdmetalle," *Z. Anorg. Allg. Chem*, vol. 288, no. 1-2, pp. 87–90, 1956.

[20] R. A. Young and W. T. Ziegler, "Crystal Structure of Lanthanum Nitride," *J. Am. Chem. Soc.*, vol. 74, no. 21, pp. 5251–5253, 1952.

[21] F. Endter, "Die Kristallstruktur des Gadoliniumnitrids," *Z. Anorg. Chem.*, vol. 257, no. 1-3, pp. 127–130, 1948.

[22] R. Didchenko and F. Gortsema, "Some electric and magnetic properties of rare earth monosulfides and nitrides," *J. Phys. Chem. Solids*, vol. 24, no. 7, pp. 863 – 870, 1963.

[23] R. D. Shannon, "Revised effective ionic radii and systematic studies of interatomic distances in halides and chalcogenides," *Acta Crystallogr. Sect. A*, vol. 32, no. 5, pp. 751–767, 1976.

[24] F. Natali, B. J. Ruck, N. O. V. Plank, H. J. Trodahl, S. Granville, C. Meyer, and W. R. L. Lambrecht, "Rare-earth mononitrides," *Prog. Mater Sci.*, vol. 58, no. 8, pp. 1316 – 1360, 2013.

[25] F. Natali, N. O. V. Plank, J. Galipaud, B. J. Ruck, H. J. Trodahl, F. Semond, S. Sorieul, and L. Hirsch, "Epitaxial growth of GdN on silicon substrate using an AlN buffer layer," *J. Cryst. Growth*, vol. 312, no. 24, pp. 3583 – 3587, 2010.

[26] B. M. Ludbrook, I. L. Farrell, M. Kuebel, B. J. Ruck, A. R. H. Preston, H. J. Trodahl, L. Ranno, R. J. Reeves, and S. M. Durbin, "Growth and properties of epitaxial GdN," *J. Appl. Phys.*, vol. 106, no. 6, p. 063910, 2009.

[27] H. Yoshitomi, S. Kitayama, T. Kita, O. Wada, M. Fujisawa, H. Ohta, and T. Sakurai, "Optical and magnetic properties in epitaxial GdN thin films," *Phys. Rev. B*, vol. 83, p. 155202, Apr 2011.

[28] R. Dargis, R. Smith, F. E. Arkun, and A. Clark, "Epitaxial rare earth oxide and nitride buffers for GaN growth on Si," *Phys. Status Solidi (c)*, vol. 11, no. 3-4, pp. 569–572, 2014.

[29] I. L. Farrell, R. J. Reeves, A. R. H. Preston, B. M. Ludbrook, J. E. Downes, B. J. Ruck, and S. M. Durbin, "Tunable electrical and optical properties of hafnium nitride thin films," *Appl. Phys. Lett.*, vol. 96, no. 7, p. 071914, 2010.

[30] S. Granville, B. J. Ruck, F. Budde, A. Koo, D. J. Pringle, F. Kuchler, A. R. H. Preston, D. H. Housden, N. Lund, A. Bittar, G. V. M. Williams, and H. J. Trodahl, "Semiconducting ground state of GdN thin films," *Phys. Rev. B*, vol. 73, p. 235335, Jun 2006.

[31] M. Azeem, B. J. Ruck, B. Do Le, H. Warring, H. J. Trodahl, N. M. Strickland, A. Koo, V. Goian, and S. Kamba, "Optical response of DyN," *J. Appl. Phys.*, vol. 113, no. 20, p. 203509, 2013.

[32] D. Le Binh, B. J. Ruck, F. Natali, H. Warring, H. J. Trodahl, E.-M. Anton, C. Meyer, L. Ranno, F. Wilhelm, and A. Rogalev, "Europium Nitride: A Novel Diluted Magnetic Semiconductor," *Phys. Rev. Lett.*, vol. 111, p. 167206, Oct 2013.

[33] C. Meyer, B. J. Ruck, A. R. H. Preston, S. Granville, G. V. M. Williams, and H. J. Trodahl, "Magnetic properties of ErN films ," *J. Magn. Magn. Mater.*, vol. 322, no. 14, pp. 1973 – 1978, 2010.

[34] D. L. Cortie, J. D. Brown, S. Brück, T. Saerbeck, J. P. Evans, H. Fritzsche, X. L. Wang, J. E. Downes, and F. Klose, "Intrinsic reduction of the ordered $4f$ magnetic moments in semiconducting rare-earth nitride thin films: DyN, ErN, and HoN," *Phys. Rev. B*, vol. 89, p. 064424, Feb 2014.

[35] C.-G. Duan, R. F. Sabirianov, W. N. Mei, P. A. Dowben, S. S. Jaswal, and E. Y. Tsymbal, "Electronic, magnetic and transport properties of rare-earth monopnictides," *J. Phys. Condens. Matter*, vol. 19, no. 31, p. 315220, 2007.

[36] A. Hasegawa and A. Yanase, "Energy band structures of Gd-pnictides," *J. Phys. Soc. Jpn.*, vol. 42, no. 2, pp. 492–498, 1977.

[37] A. Hasegawa, "Electronic structure of La monopnictides," *J. Phys. C. (Solid State Phys.)*, vol. 13, no. 33, p. 6147, 1980.

[38] A. G. Petukhov, W. R. L. Lambrecht, and B. Segall, "Electronic structure of rare-earth pnictides," *Phys. Rev. B*, vol. 53, pp. 4324–4339, Feb 1996.

[39] C. M. Aerts, P. Strange, M. Horne, W. M. Temmerman, Z. Szotek, and A. Svane, "Half-metallic to insulating behavior of rare-earth nitrides," *Phys. Rev. B*, vol. 69, p. 045115, Jan 2004.

[40] W. M. Temmerman, Z. Szotek, and H. Winter, "Band-structure method for 4 f electrons in elemental Pr metal," *Phys. Rev. B*, vol. 47, pp. 1184–1189, Jan 1993.

[41] L. Hedin, "New Method for Calculating the One-Particle Green's Function with Application to the Electron-Gas Problem," *Phys. Rev.*, vol. 139, pp. A796–A823, Aug 1965.

[42] A. N. Chantis, M. van Schilfgaarde, and T. Kotani, "Quasiparticle self-consistent GW method applied to localized $4f$ electron systems," *Phys. Rev. B*, vol. 76, p. 165126, Oct 2007.

[43] N. O. V. Plank, F. Natali, J. Galipaud, J. H. Richter, M. Simpson, H. J. Trodahl, and B. J. Ruck, "Enhanced Curie temperature in N-deficient GdN," *Appl. Phys. Lett.*, vol. 98, no. 11, 2011.

[44] F. Natali, S. Vézian, S. Granville, B. Damilano, H. J. Trodahl, E.-M. Anton, H. Warring, F. Semond, Y. Cordier, S. V. Chong, and B. J. Ruck, "Molecular beam epitaxy of ferromagnetic epitaxial GdN thin films," *J. Cryst. Growth*, vol. 404, pp. 146 – 151, 2014.

[45] F. Natali, B. Ludbrook, J. Galipaud, N. Plank, S. Granville, A. Preston, B. L. Do, J. Richter, I. Farrell, R. Reeves, S. Durbin, J. Trodahl, and B. Ruck,

"Epitaxial growth and properties of GdN, EuN and SmN thin films," *Phys. Status Solidi (c)*, vol. 9, no. 3-4, pp. 605–608, 2012.

[46] C. Meyer, B. J. Ruck, J. Zhong, S. Granville, A. R. H. Preston, G. V. M. Williams, and H. J. Trodahl, "Near-zero-moment ferromagnetism in the semiconductor SmN," *Phys. Rev. B*, vol. 78, p. 174406, Nov 2008.

[47] H. J. Trodahl, A. R. H. Preston, J. Zhong, B. J. Ruck, N. M. Strickland, C. Mitra, and W. R. L. Lambrecht, "Ferromagnetic redshift of the optical gap in GdN," *Phys. Rev. B*, vol. 76, no. 8, p. 085211, 2007.

[48] A. R. H. Preston, S. Granville, D. H. Housden, B. Ludbrook, B. J. Ruck, H. J. Trodahl, A. Bittar, G. V. M. Williams, J. E. Downes, A. DeMasi, Y. Zhang, K. E. Smith, and W. R. L. Lambrecht, "Comparison between experiment and calculated band structures for DyN and SmN," *Phys. Rev. B*, vol. 76, no. 24, p. 245120, 2007.

[49] E.-M. Anton, S. Granville, A. Engel, S. V. Chong, M. Governale, U. Zülicke, A. G. Moghaddam, H. J. Trodahl, F. Natali, S. Vézian, and B. J. Ruck, "Superconductivity in the ferromagnetic semiconductor SmN," *arXiv preprint arXiv:1505.03621*, 2015.

[50] J. H. Richter, B. J. Ruck, M. Simpson, F. Natali, N. O. V. Plank, M. Azeem, H. J. Trodahl, A. R. H. Preston, B. Chen, J. McNulty, K. E. Smith, A. Tadich, B. Cowie, A. Svane, M. van Schilfgaarde, and W. R. L. Lambrecht, "Electronic structure of EuN: Growth, spectroscopy, and theory," *Phys. Rev. B*, vol. 84, p. 235120, Dec 2011.

[51] H. Warring, B. J. Ruck, J. F. McNulty, E.-M. Anton, S. Granville, A. Koo, B. Cowie, and H. J. Trodahl, "YbN: An intrinsic semiconductor with antiferromagnetic exchange," *Phys. Rev. B*, vol. 90, p. 245206, Dec 2014.

[52] L. Degiorgi, W. Bacsa, and P. Wachter, "Electronic structure of YbN," *Phys. Rev. B*, vol. 42, no. 1, p. 530, 1990.

[53] D. B. Ghosh, M. De, and S. De, "Electronic, magnetic, and optical properties of Gd monopnictides: An LDA+ U study," *Phys. Rev. B*, vol. 72, no. 4, p. 045140, 2005.

[54] C. Mitra and W. R. Lambrecht, "Magnetic exchange interactions in the gadolinium pnictides from first principles," *Phys. Rev. B*, vol. 78, no. 13, p. 134421, 2008.

[55] C.-G. Duan, R. F. Sabiryanov, W.-N. Mei, P. A. Dowben, S. Jaswal, and E. Y. Tsymbal, "Magnetic ordering in Gd monopnictides: Indirect exchange versus superexchange interaction," *Appl. Phys. Lett.*, vol. 88, no. 18, p. 182505, 2006.

[56] A. Sharma and W. Nolting, "Additional carrier-mediated ferromagnetism in GdN," *Phys. Rev. B*, vol. 81, no. 12, p. 125303, 2010.

[57] J. F. McNulty, B. J. Ruck, and H. J. Trodahl, "On the ferromagnetic ground state of SmN," *Phys. Rev. B*, vol. 93, p. 054413, Feb 2016.

[58] E.-M. Anton, J. F. McNulty, B. J. Ruck, M. Suzuki, M. Mizumaki, V. N. Antonov, J. W. Quilty, N. Strickland, and H. J. Trodahl, "NdN: An intrinsic ferromagnetic semiconductor," *Phys. Rev. B*, vol. 93, no. 6, p. 064431, 2016.

[59] N. W. Ashcroft and N. D. Mermin, *Solid State Physics*. New York: Holt, Rinehart and Winston, 1976.

[60] F. Natali, B. J. Ruck, H. J. Trodahl, D. L. Binh, S. Vézian, B. Damilano, Y. Cordier, F. Semond, and C. Meyer, "Role of magnetic polarons in ferromagnetic GdN," *Phys. Rev. B*, vol. 87, p. 035202, Jan 2013.

[61] E.-M. Anton, B. J. Ruck, C. Meyer, F. Natali, H. Warring, F. Wilhelm, A. Rogalev, V. N. Antonov, and H. J. Trodahl, "Spin/orbit moment imbalance in the near-zero moment ferromagnetic semiconductor SmN," *Phys. Rev. B*, vol. 87, no. 13, p. 134414, 2013.

[62] H. Ohno, "A window on the future of spintronics," *Nat. Mater.*, vol. 9, no. 12, pp. 952–954, 2010.

[63] S. Datta and B. Das, "Electronic analog of the electro-optic modulator," *Appl. Phys. Lett.*, vol. 56, no. 7, pp. 665–667, 1990.

[64] H. Kurt, K. Rode, P. Stamenov, M. Venkatesan, Y.-C. Lau, E. Fonda, and J. M. D. Coey, "Cubic Mn_2Ga Thin Films: Crossing the Spin Gap with Ruthenium," *Phys. Rev. Lett.*, vol. 112, p. 027201, 2014.

[65] N. Thiyagarajah, Y.-C. Lau, D. Betto, K. Borisov, J. M. D. Coey, P. Stamenov, and K. Rode, "Giant spontaneous Hall effect in zero-moment Mn_2Ru_xGa," *Appl. Phys. Lett.*, vol. 106, no. 12, p. 122402, 2015.

[66] M. Scarpulla, C. Gallinat, S. Mack, J. Speck, and A. Gossard, "GdN (1 1 1) heteroepitaxy on GaN (0 0 0 1) by N_2 plasma and NH_3 molecular beam epitaxy," *J. Cryst. Growth*, vol. 311, no. 5, pp. 1239 – 1244, 2009.

[67] J. W. Gerlach, J. Mennig, and B. Rauschenbach, "Epitaxial gadolinium nitride thin films," *Appl. Phys. Lett.*, vol. 90, no. 6, 2007.

[68] MicroChemicals GmbH, "Exposure of Photoresists." `http://www.microchemicals.com/technical_information/exposure_photoresist.pdf`, Nov 2013. Accessed Online March 2016.

[69] C. W. Gwyn, R. Stulen, D. Sweeney, and D. Attwood, "Extreme ultraviolet lithography," *J. Vac. Sci. Technol. B*, vol. 16, no. 6, pp. 3142–3149, 1998.

[70] C. Vieu, F. Carcenac, A. Pepin, Y. Chen, M. Mejias, A. Lebib, L. Manin-Ferlazzo, L. Couraud, and H. Launois, "Electron beam lithography: resolution limits and applications," *Appl. Surf. Sci.*, vol. 164, no. 1, pp. 111–117, 2000.

[71] L. J. van der Pauw, "A method of measuring specific resistivity and hall effect of lamellae of arbitrary shape," *Philips Res. Rep.*, vol. 13, p. 19, Feb 1958.

[72] P. A. Joy, P. S. A. Kumar, and S. K. Date, "The relationship between field-cooled and zero-field-cooled susceptibilities of some ordered magnetic systems," *J. Phys. Condens. Matter*, vol. 10, no. 48, p. 11049, 1998.

[73] P. Scherrer, "Bestimmung der Größe und der inneren Struktur von Kolloidteilchen mittels Röntgenstrahlen," *Nachrichten von der Gesellschaft der Wissenschaften zu Gttingen, Mathematisch-Physikalische Klasse*, vol. 1918, pp. 98–100, 1918.

[74] W. L. Bragg, "The diffraction of short electromagnetic waves by a crystal," in *Proceedings of the Cambridge Philosophical Society*, vol. 17, p. 4, 1913.

[75] F. Ullstad, J. R. Chan, H. Warring, N. Plank, B. Ruck, J. Trodahl, and F. Natali, "Ohmic contacts of Au and Ag metals to n-type GdN thin films," *AIMS Materials Science*, vol. 2, no. 20150204, pp. 79–85, 2015.

[76] J. M. Pomeroy and H. Grube, "negative resistance errors in four-point measurements of tunnel junctions and other crossed-wire devices," *J. Appl. Phys.*, vol. 105, no. 9, 2009.

[77] H. Zeng, Y. Wu, J. Zhang, C. Kuang, M. Yue, and S. Zhou, "Grain size-dependent electrical resistivity of bulk nanocrystalline Gd metals," *Prog. Nat. Sci.: Mater. Int.*, vol. 23, no. 1, pp. 18 – 22, 2013.

[78] M. Julliere, "Tunneling between ferromagnetic films," *Phys. Lett. A*, vol. 54, no. 3, pp. 225 – 226, 1975.

[79] H. Swagten, "Chapter One Spin-Dependent Tunneling in Magnetic Junctions," vol. 17 of *Handbook of Magnetic Materials*, pp. 1 – 121, Elsevier, 2007.

[80] W. E. Pickett and J. S. Moodera, "Half metallic magnets," *Phys. Today*, vol. 54, no. 5, pp. 39–45, 2001.

[81] J. S. Parker, S. M. Watts, P. G. Ivanov, and P. Xiong, "Spin Polarization of CrO_2 at and across an Artificial Barrier," *Phys. Rev. Lett.*, vol. 88, p. 196601, Apr 2002.

[82] M. Bowen, M. Bibes, A. Barthélémy, J.-P. Contour, A. Anane, Y. Lemaître, and A. Fert, "Nearly total spin polarization in $La_{2/3}Sr_{1/3}MnO_3$ from tunneling experiments," *Appl. Phys. Lett.*, vol. 82, no. 2, pp. 233–235, 2003.

[83] M. Tanaka and Y. Higo, "Large Tunneling Magnetoresistance in GaMnAs /AlAs /GaMnAs Ferromagnetic Semiconductor Tunnel Junctions," *Phys. Rev. Lett.*, vol. 87, p. 026602, Jun 2001.

[84] H. Saito, S. Yuasa, and K. Ando, "Origin of the Tunnel Anisotropic Magnetoresistance in $Ga_{1-x}Mn_xAs$/ZnSe/$Ga_{1-x}Mn_xAs$ Magnetic Tunnel Junctions of II-VI/III-V Heterostructures," *Phys. Rev. Lett.*, vol. 95, p. 086604, Aug 2005.

[85] M. Gajek, M. Bibes, S. Fusil, K. Bouzehouane, J. Fontcuberta, A. Barthelemy, and A. Fert, "Tunnel junctions with multiferroic barriers," *Nat Mater*, vol. 6, no. 4, pp. 296–302, 2007.

[86] H. Sukegawa, Z. Wen, K. Kondou, S. Kasai, S. Mitani, and K. Inomata, "Spin-transfer switching in full-Heusler Co_2FeAl-based magnetic tunnel junctions," *Appl. Phys. Lett.*, vol. 100, no. 18, p. 182403, 2012.

[87] I. N. Sivkov, O. O. Brovko, and V. S. Stepanyuk, "Spin-polarized transport properties of GdN nanocontacts," *Phys. Rev. B*, vol. 89, p. 195419, May 2014.

[88] V. Perel, S. Tarasenko, I. Yassievich, S. Ganichev, V. Belkov, and W. Prettl, "Spin-dependent tunneling through a symmetric semiconductor barrier," *Phys. Rev. B*, vol. 67, no. 20, p. 201304, 2003.

[89] R. Holm, "The Electric Tunnel Effect across Thin Insulator Films in Contacts," *J. Appl. Phys.*, vol. 22, no. 5, pp. 569–574, 1951.

[90] A. Sommerfeld and H. Bethe, "Handbuch der Physik von Geiger und Scheel," *Julius Springer-Verlag, Berlin*, p. 450, 1933.

[91] J. Frenkel, "On the electrical resistance of contacts between solid conductors," *Phys. Rev.*, vol. 36, pp. 1604–1618, Dec 1930.

[92] J. G. Simmons, "Generalized Formula for the Electric Tunnel Effect between Similar Electrodes Separated by a Thin Insulating Film," *J. Appl. Phys.*, vol. 34, no. 6, pp. 1793–1803, 1963.

[93] W. H. Butler, X.-G. Zhang, T. C. Schulthess, and J. M. MacLaren, "Spin-dependent tunneling conductance of Fe|MgO|Fe sandwiches," *Phys. Rev. B*, vol. 63, p. 054416, Jan 2001.

[94] J. Bardeen, "Tunnelling from a Many-Particle Point of View," *Phys. Rev. Lett.*, vol. 6, pp. 57–59, Jan 1961.

[95] J. G. Simmons, "Generalized Thermal J-V Characteristic for the Electric Tunnel Effect," *J. Appl. Phys.*, vol. 35, no. 9, pp. 2655–2658, 1964.

[96] V. Bougrov, *Properties of Advanced Semiconductor Materials GaN, AlN, InN, BN, SiC, SiGe*, pp. 1–30. New York: John Wiley & Sons, Inc., 2001.

[97] Y. Goldberg, *Properties of Advanced Semiconductor Materials GaN, AlN, InN, BN, SiC, SiGe*, pp. 31–47. New York: John Wiley & Sons, Inc., 2001.

[98] S. Strite and H. Morkoç, "GaN, AlN, and InN: A review," *J. Vac. Sci. Technol. B*, vol. 10, no. 4, pp. 1237–1266, 1992.

[99] W. M. Yim, E. J. Stofko, P. J. Zanzucchi, J. I. Pankove, M. Ettenberg, and S. L. Gilbert, "Epitaxially grown AlN and its optical band gap," *J. Appl. Phys.*, vol. 44, no. 1, pp. 292–296, 1973.

[100] T. Kagawa and H. Raebiger, "Schottky Barrier Formation and Strain at the (011) GdN/GaN Interface from First Principles," *Phys. Rev. Applied*, vol. 2, p. 054009, Nov 2014.

[101] A. Schmehl, V. Vaithyanathan, A. Herrnberger, S. Thiel, C. Richter, M. Liberati, T. Heeg, M. Röckerath, L. F. Kourkoutis, S. Mühlbauer, *et al.*, "Epitaxial integration of the highly spin-polarized ferromagnetic semiconductor EuO with silicon and GaN," *Nat Mater*, vol. 6, no. 11, pp. 882–887, 2007.

[102] F. Bernardini and V. Fiorentini, "Macroscopic polarization and band offsets at nitride heterojunctions," *Phys. Rev. B*, vol. 57, pp. R9427–R9430, Apr 1998.

[103] G. Qixin and Y. Akira, "Temperature Dependence of Band Gap Change in InN and AlN," *Jpn. J. Appl. Phys.*, vol. 33, no. 5R, p. 2453, 1994.

[104] R. J. M. van de Veerdonk, J. Nowak, R. Meservey, J. S. Moodera, and W. J. M. de Jonge, "Current distribution effects in magnetoresistive tunnel junctions," *Appl. Phys. Lett.*, vol. 71, no. 19, pp. 2839–2841, 1997.

[105] J. M. Rowell, E. Burstein, and S. Lundquist, "Tunneling Phenomena in Solids," *Plenum Press, New York*, 1969.

[106] J. J. Åkerman, R. Escudero, C. Leighton, S. Kim, D. Rabson, R. W. Dave, J. Slaughter, and I. K. Schuller, "Criteria for ferromagnetic-insulator-ferromagnetic tunneling," *J. Magn. Magn. Mater.*, vol. 240, no. 13, pp. 86 – 91, 2002. 4th International Symposium on Metallic Multilayers.

[107] N. Nagaosa, J. Sinova, S. Onoda, A. H. MacDonald, and N. P. Ong, "Anomalous Hall effect," *Rev. Mod. Phys.*, vol. 82, pp. 1539–1592, 2010.

[108] J. Sinova, S. O. Valenzuela, J. Wunderlich, C. H. Back, and T. Jungwirth, "Spin Hall effects," *Rev. Mod. Phys.*, vol. 87, pp. 1213–1260, Oct 2015.

[109] A. Manchon, "Spin-orbitronics: A new moment for Berry," *Nature Phys.*, vol. 10, p. 340, 2014.

[110] J. Van Vleck, *The theory of electric and magnetic susceptibilities*. International series of monographs on physics, Oxford University Press, 1952.

[111] F. Matsukura, M. Sawicki, T. Dietl, D. Chiba, and H. Ohno, "Magnetotransport properties of metallic (Ga,Mn)As films with compressive and tensile strain," *Physica E: Low-dimensional Systems and Nanostructures*, vol. 21, no. 24, pp. 1032 – 1036, 2004. Proceedings of the Eleventh International Conference on Modulated Semiconductor Structures.

[112] L. Yuan, S.-H. Liou, and D. Wang, "Temperature dependence of magnetoresistance in magnetic tunnel junctions with different free layer structures," *Phys. Rev. B*, vol. 73, no. 13, p. 134403, 2006.

[113] H. Amano, M. Kito, K. Hiramatsu, and I. Akasaki, "P-type conduction in Mg-doped GaN treated with low-energy electron beam irradiation (LEEBI)," *Jpn. J. Appl. Phys.*, vol. 28, no. 12A, p. L2112, 1989.

[114] T. Shiosaki, T. Yamamoto, T. Oda, K. Harada, and A. Kawabata, "Low temperature growth of piezoelectric AlN film for surface and bulk wave transducers by RF reactive planar magnetron sputtering," in *1980 Ultrasonics Symposium*, pp. 451–454, IEEE, 1980.

[115] T. Lei, M. Fanciulli, R. Molnar, T. Moustakas, R. Graham, and J. Scanlon, "Epitaxial growth of zinc blende and wurtzitic gallium nitride thin films on (001) silicon," *Appl. Phys. Lett.*, vol. 59, no. 8, pp. 944–946, 1991.

[116] A. Punya, T. Cheiwchanchamnangij, A. Thiess, and W. R. Lambrecht, "First-principles Study of Nitrogen Vacancies in GdN," in *MRS Proceedings*, vol. 1290, pp. mrsf10–1290, Cambridge Univ Press, 2011.

[117] J. Coey, M. Venkatesan, and C. Fitzgerald, "Donor impurity band exchange in dilute ferromagnetic oxides," *Nat. Mater.*, vol. 4, no. 2, pp. 173–179, 2005.

[118] C.-M. Lee, H. Warring, S. Vézian, B. Damilano, S. Granville, M. Al Khalfioui, Y. Cordier, H. J. Trodahl, B. J. Ruck, and F. Natali, "Highly resistive epitaxial Mg-doped GdN thin films," *Appl. Phys. Lett.*, vol. 106, no. 2, 2015.

[119] C.-M. Lee, H. Warring, S. Vézian, H. J. Trodahl, B. J. Ruck, and F. Natali, "Photoconductivity investigation of recombination in Mg-doped epitaxial GdN thin Films," *Appl. Phys. Lett.*, Submitted 2016.

[120] R. A. Matula, "Electrical resistivity of copper, gold, palladium, and silver," *J. Phys. Chem. Ref. Data*, vol. 8, no. 4, pp. 1147–1298, 1979.

[121] Comsol, *COMSOL Multiphysics: Version 5.2*. Comsol, 2015.

[122] D. Bohm, *Quantum theory*. Prentice-Hall, 1951.

[123] D. J. Griffiths, *Introduction to quantum mechanics*. Pearson Prentice Hall, 2005.

[124] H. Murayama, "221A Lecture Notes WKB Method." `http://hitoshi.berkeley.edu/221a/wkb.pdf`, Jan 2014. Accessed Online Feb 2016.

[125] R. Stratton, "Volt-current characteristics for tunneling through insulating films," *J. Phys. Chem. Solids*, vol. 23, no. 9, pp. 1177 – 1190, 1962.

[126] W. H. Butler, "Tunneling magnetoresistance from a symmetry filtering effect," *Sci. Tech. Adv. Mater.*, 2016.

[127] E. L. Murphy and R. H. Good, "Thermionic Emission, Field Emission, and the Transition Region," *Phys. Rev.*, vol. 102, pp. 1464–1473, Jun 1956.

[128] Maplesoft, "Maple (12)," 2008.